Fabrication of Novel Microfluidic Devices for Investigating Ultrafast Structural Dynamics

Dissertation zur Erlangung des Doktorgrades
an der Fakultät für Mathematik, Informatik und Naturwissenschaften
Fachbereich Physik
der Universität Hamburg

vorgelegt von
Vasireddi Ramakrishna
aus
Andhra Pradesh
India

Hamburg
2019

Gutachter/innen der Dissertation:	Prof. Dr. Martin Trebbin
	Prof. Dr. Nils Huse
Gutachter der Disputation:	Prof. Dr. Martin Trebbin
	Prof. Dr. Nils Huse
	Prof. Dr. Gerhard Grubel
	Prof. Dr. Daniela Pfannkuche
	Dr. Thomas Keller
Vorsitzende der Prüfungskommission:	Prof. Dr. Daniela Pfannkuche
Datum der Disputation:	29.03.2019
Vorsitzender Fach-Promotionsausschusses PHYSIK:	Prof. Dr. Michael Potthoff
Leiter des Fachbereichs PHYSIK:	Prof. Dr. Wolfgang Hansen
Dekan der Fakultät MIN:	Prof. Dr. Heinrich Graener

Abstract

The recent developments of several X-ray synchrotrons and (ultrabright) XFEL light sources with increasingly narrow and brilliant beams have allowed facilities to reduce both sample volume and data acquisition time. Moreover, this has created new opportunities for investigating versatile sample conditions while simultaneously increasing demands in terms of sample preparation. The microfluidic flat liquid jet based sample preparation techniques are emerging as promising alternatives for manipulating small sample volumes and which can be integrated more easily into the experimental X-ray setups. The main goal of the thesis is to study and develop an innovative microfluidic flat liquid jet device technology that is suitable for microfocus X-ray scattering techniques. Furthermore, simultaneously providing a platform to control the experimental conditions for investigating particle alignments, spinning fibers and spectroscopic studies in the future.

The first part of the thesis deals with the development, fabrication and testing of high aspect ratio microfluidic flat liquid jet devices. The development of a method to fabricate three-dimensional and three-layered microstructures from photoresists SU-8 2050 was established with an increased nozzle height of 100 µm. Achieving exact control of the nozzle geometry at such high aspect ratios requires solving several issues such as edge beading, wafer bowing and UV-exposure artefacts. These issues have been overcome by successfully optimizing protocols and process parameters to produce high aspect ratio structures with suitable feature sizes. The optimized devices are based use the gas dynamic virtual nozzle (GDVN) principle, where the co-axially flowing gas focusses the liquids. The highly stable thin liquid sheets reported here enabled us to reduce the sample consumption up to tenfold in comparison to the traditional flat liquid jet injectors without gas -focusing. Our devices are produced by well-established soft-lithography techniques, which allow for exact control over the design and reproducibility of the nozzle geometry. The microfluidic flat liquid jet device generates a series of alternating, orthogonal stable liquid sheets with thicknesses approximately a few microns. Sheet width and length are dependent on the high aspect ratio nozzle geometry and flow parameters such as gas pressure and liquid flow rates. This work enriches multiple arenas such as soft X-ray spectroscopy because of optical the flatness and spatial stability of these jets. And hence offers exciting well-grounded versatile opportunities for ultrafast molecular science, ultrafast chemical dynamics, X-ray beam

diagnostics and industrial applications. Furthermore, the optimized fabrication methodology and nozzle geometry parameters provide useful design directions for whipping and fiber jets.

The second part of the thesis is a wide-angle X-ray scattering (WAXS) study of the influence of shear flow on the alignment of anisotropic nanoparticles in a liquid sheet. Spindle-shaped hematite nanoparticles showed alignment across and along the sheet jet with a preferred orientation along the flow axis in the center of the sheet and along the jet.

Furthermore, the optimized GDVN geometry is also suitable for micro- and nano-fiber spinning from polymer solutions by offering very high jetting stability, relinquishing the need for external fiber pulling mechanisms. These nozzle geometries allow fiber production of nanocomposite fibers and nanofibers with various tunable morphologies such as round, flat and grooved. Compared to other fiber spinning methods, this technique is inexpensive, user-friendly and permits precise fiber diameter control (~250 nm to ~15 μm), high production rate (m/s-range) and direct fiber deposition without clogging. The fabricated hematite/CNT nanocomposite endless fibers have exciting applications in the future. These fibers have thermal and electrical conductivity, magnetic properties, enhanced mechanical stability and stimuli-responsive features.

Zusammenfassung

Dank der jüngsten Entwicklung an mehreren Synchrotron- und XFEL- Röntgenlichtquellen stehen der Wissenschaft zunehmend kleinere und brillantere Strahlen zur Verfügung, was den Einsatz geringer Probenvolumina ermöglicht und die Datenerfassungszeit reduziert. Dieses eröffnet neue Möglichkeiten zur Untersuchung der Art und Anzahl der zu untersuchenden Probenzustände, erhöht aber auch gleichzeitig die Anforderungen an die Probenvorbereitung und -umgebung. Die mikrofluidische Probenumgebung basierend auf Liquid Jets hat sich als vielversprechende Methode zur Handhabung von Proben geringer Volumina und spezieller Funktionalitäten herausgebildet, die sich leicht in die experimentellen Setups an den Strahlrohren integrieren lässt. Das Hauptziel der vorliegenden Arbeit ist daher die Entwicklung einer neuartigen und innovativen, mikrofluidischen Flat-Liquid-Jet-Apparatur, welche für Mikrofokus-Röntgenstreuung geeignet ist und die Erforschung von Teilchenorientierung, Faserspinnen sowie zukünftig auch Spektroskopie mit einstellbaren Betriebsparametern ermöglicht.

Der erste Teil dieser Dissertation widmet sich der Entwicklung, der Herstellung sowie der experimentellen Charakterisierung von Flat-Liquid-Jet-Apparaten mit hohem Querschnittsverhältnis. Es wird ein Verfahren zur Herstellung dreidimensionaler und dreischichtiger Mikrostrukturen aus dem Photolack SU-8 2050 mit einer erhöhten Düsenhöhe von 100 µm entwickelt. Die exakte Kontrolle über die Düsengeometrie unter Beibehaltung einer minimalen Merkmalsgröße führt zu verschiedenen Problemen, wie etwa dem sog. Edge Beading (der Ansammlung von Photolack an den Waferrändern), der Wafer-Wölbung oder einer verminderten Auflösung. Durch Optimierung der Versuchsprotokolle und durch Wahl geeigneter Prozessparameter konnten diese Probleme erfolgreich überwunden und Strukturen mit einem hohem Seitenverhältnis hergestellt werden. Die so optimierten Designs basieren auf dem Prinzip der gas-dynamischen virtuellen Düse (Engl.: gas-dynamic virtual nozzle, GDVN), bei dem die Flüssigkeit durch ein koaxial strömendes Gas fokussiert wird. Eine damit erzeugte stabile, dünne Flüssigkeitsschicht ermöglicht es, den Probenverbrauch im Vergleich zu herkömmlichen Liquid-Jet-Injektoren ohne Gasstrom auf ein Zehntel zu reduzieren. Die Apparate werden im etablierten softlithographischen Verfahren hergestellt, was eine exakte Kontrolle des Designs und eine hohe Reproduzierbarkeit der Düsengeometrie ermöglicht. Die vorgestellten Apparate erzeugen reproduzierbar eine Abfolge von orthogonal zu einander stehenden Flüssigkeitsscheiben von

wenigen Mikrometern Dicke. Es werden Schichtdicken und –längen in Abhängigkeit von Geometrieparametern, wie Seitenverhältnis der Düsengeometrie, und von Prozessparametern, wie Gasdruck und Massenstrom, vorgestellt. Durch die Bereitstellung von optisch planen und räumlich stabilen Jets bereichert die vorliegende Arbeit mehrere Forschungsgebiete, wie beispielsweise die weiche Röntgenspektroskopie. Zudem eröffnen die Ergebnisse dieser Arbeit vielerlei Möglichkeiten im Bereich der ultraschnellen Molekularforschung, zur Untersuchung ultraschneller chemischer Reaktionen, für die Röntgenstrahl-Diagnostik und für industrielle Anwendungen. Dank der vorgestellten optimierten Fertigungsmethode dient diese Arbeit darüber hinaus als Anleitung zur Herstellung von Düsengeometrien für sogenannte oszillierende, oder „whipping“ Jets sowie für das Faserspinnen.

Der zweite Teil der Arbeit ist eine WAXS-Studie zum Einfluss der Scherung auf die Ausrichtung anisotroper Nanopartikel in einem dünnen Flüssigkeitsstrahl. Spindelförmige Hämatit-Nanopartikel zeigen eine Ausrichtung orthogonal und entlang der flachen Flüssigkeitsstrahlen mit einer bevorzugten Ausrichtung in der Mitte der Dünnschicht entlang der Flussrichtung.

Nach Optimierung der Düsengeometrie war es möglich einheitliche, funktionelle Mikro- und Nanofasern aus Polymerlösungen zu spinnen. Hierbei wurde eine sehr hohe Jet-Stabilität beobachtet, was externe Faserziehmechanismen obsolet macht. Diese neue Düsengeometrie ermöglicht die Herstellung von Fasern mit einstellbarer Morphologie (rund, flach, gerillt), von Nanokompositfasern sowie von Nanofasern. Im Vergleich zu anderen Faserspinnverfahren ist diese Technik kostengünstiger und benutzerfreundlicher und ermöglicht eine genauere Steuerung des Faserdurchmessers (~ 250 nm bis ~15 μm), eine höhere Produktionsrate (m/s-Bereich) und eine direkte Faserablagerung ohne Verstopfung. Die hergestellten Hämatit/CNT-Nanokomposit-Endlosfasern sind ein zukunftweisendes Beispiel für die spannenden Anwendungen, die dieses Verfahren ermöglichen wird, wie die Herstellung von Fasern mit thermischer und elektrischer Leitfähigkeit, mit magnetischen Eigenschaften, mit verbesserter mechanischer Stabilität oder mit stimuli-responsiven Eigenschaften.

“Understanding of fundamental science is not so difficult if you do real experiments.”

-Unknown

Contents

List of figures

List of tables

Acronyms

GDVN	Gas Dynamic Virtual Nozzle
CFD	Computational Fluid Dynamics
XFEL	X-ray Free-Electron Laser
SAXS	Small Angle X-ray Scattering
WAXS	Wide Angle X-ray Scattering
SFX	Serial Femtosecond Crystallography
MEMS	Micro Electro Mechanical System
MOEMS	Micro Opto Electro Mechanical System
μTAS	Micro Total Analysis Systems
LOC	Laboratory on-a-Chip
DNA	Deoxyribonucleic Acid
CAD	Computer-Aided Design
We	Weber number
WGJ	Wire-Guided Flow Jet
PDE	Partial Differential Equation
FEM	Finite Element Method
SFA	Surface Force Apparatus
μ-PIV	Micro-Particle Image Velocimetry
PDMS	Polydimethylsiloxane
Re	Reynolds Number
Pe	Peclet number
SEM	Scanning Electron Microscopy
KH	Kelvin- Helmholtz
T_c	Taylor number
VOF	Volume of Fluid
LES	Large Eddy Simulation
UDF	User Defined Functions
THV	Fluorinated Terpolymer of Tetrafluoroethylene, Hexafluoropropylene and Vinylidene Fluoride Monomers
OD	Outer Diameter

FIB	Focused Ion Beam
CVD	Chemical Vapor Deposition
CNT	Carbon Nanotube
ddH_2O	Double Filtered Water with 18 MΩ resistivity
IPA	Isopropanol
Tg	Glass Transition Temperature
SCCM	Standard Cubic Centimeters per Minute

1. Introduction

1.1 Motivation

Visualizing the structural dynamics of matter with atomic resolution and at short time scales (femto- to attoseconds) is of great interest in many areas of physics, materials science, biology and chemistry [1-4]. For understanding these fast dynamical processes (ultrafast phenomena), one requires the combination of advanced analysis techniques such as the X-ray scattering or spectroscopy. The realization of such experiments often relies on suitable sample environments, which can benefit these experiments in the following ways. (i) For X-ray scattering use, the fast and thin liquid jets are typically used for time-resolved studies of chemical reactions, dynamics of proteins and nanorheology of liquid samples [5] (ii) while the stable liquid sheets are ideally suited for X-ray spectroscopic use as they satisfy several requirements, the first of which is optical flatness. The second requirement is that the sheet thickness should be thin for spectroscopic studies (< 500 nm) [6]. (iii) Furthermore, these flow types, such as liquid sheets, droplets and spray, are ideal for minimizing sample consumption at lower flow rates. Lithographic based fabrication allows the production of liquid jet devices for the generation of micrometer and submicron diameter droplets [7] and liquid sheets [8] using a gas dynamic virtual nozzle (GDVN) geometry [9]. However, many essential aspects of GDVN functionality have yet to be thoroughly understood and refined, while the fabrication of GDVN devices still lacks approaches for mass production.

Soft lithography is a promising microfabrication technique for the production of GDVN devices. The key element of soft lithography is an elastomeric block, mostly poly-dimethylsiloxane (PDMS) containing the desired pattern and hence utilized as a stamp, mold, mask, or device itself. As a result, this technique offers exact control over the design and high-reproducibility of the nozzle geometry. Another critical advantage of this technique is its cost-efficiency for nozzle fabrication, enabling rapid prototyping and easy device availability for other users at beamlines [7, 10]. Concerning the sample environments, the highly diverse and interdisciplinary scientific field of gas-focused microfluidic flat liquid jets is used to perform fundamental investigations such as studying motions of molecules, particle alignment and fiber spinning. From an analysis point of view, X-ray scattering techniques, high speed video microscopy, high-resolution field-

emission scanning electron microscopic methods and numerical analysis such as computational fluid dynamics (CFD) offer a variety of tools to yield fundamental fluid dynamical insights of liquids and stimulating ideas for optimizing nozzle designs for soft matter samples [11-14]. The upcoming of current developments of X-rays free-electron laser facilities (XFEL) and third-generation synchrotron technologies paves the way for exciting possibilities such as time-resolved experiments. XFELs can produce extremely short X-ray pulses with 10^{12} photons per pulse. Moreover, XFEL pulses can be focused down to 0.1 µm without any significant reduction of X-ray photons carried to the sample. The combination of fast X-ray sources, high-speed video microscopy, computational fluid dynamics and GDVN based microfluidic flat liquid jets is an upcoming robust experimental methodology suitable for ultrafast molecular science, single-particle imaging, anisotropic nanoparticle alignment and the *in-situ* study of structural dynamics [15-18].

1.2 X-Ray scattering/spectroscopy

The application of X-ray scattering for the study of matter has a long tradition, ranging back to Wilhelm Roentgen, who discovered X-rays in 1895 [19]. X-rays is an electromagnetic radiation with short wavelengths of about 0.01 to 10 nm. The interaction of X-rays with matter allows the study of matter down to the atomic scale [20, 21]. Due to the advanced X-ray focusing designs, novel X-ray optics and beam control of third-generation light sources, the brilliance of X-ray beams has been greatly improved [22]. A relevant synchrotron radiation property becomes its spectral brightness or flux per unit source area and unit solid angle. Nowadays, the beam can be focused down to tiny spots down to the few nm-range, which is highly relevant for scanning and imaging X-ray experiments [23-26].

The development towards smaller beam sizes for scattering experiments primarily motivates the probability of probing the structure at smaller spatial areas. Smaller beam (allows for smaller sample volumes) probes with better signal-to-noise statistics [27-31]. Such point-focus equipment has replaced older slit-focus equipment together with advances in high-precision mirrors for brightness preservation and these advances now enable better-focused X-rays [32-34].

For the characterization of nanometer-scaled objects, X-ray scattering is a commonly used technique. Moreover, this is further distinguished into small- and wide-angle X-ray scattering (SAXS and WAXS) depending on the observed scattering angles. As an example, the microfluidic WAXS experiment, at microfocus beamline ID13 (ESRF, Grenoble), the X-ray beam size was adjusted to spot sizes around 3 μm by 3 μm to maintain the best combination of spatial resolution and high photon flux [35] as shown in Fig.1.

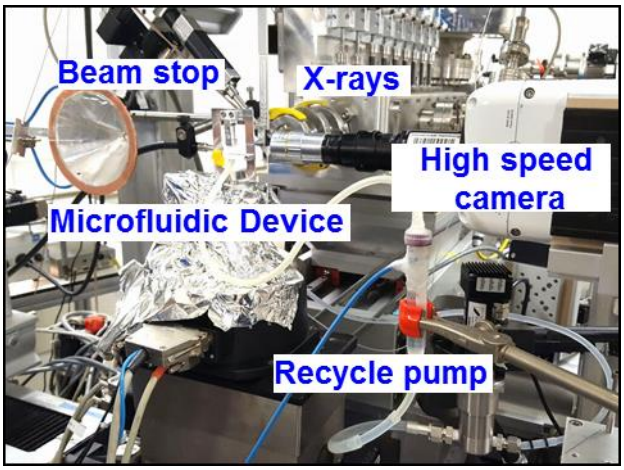

Fig.1: Photo of the experimental setups at the ID13 beamline at the ESRF synchrotron (Grenoble, France). The micro-focused X-rays pass through the stable flat liquid sheet jet that is monitored by a camera. The sheet flow is observed by a high-speed camera and controlled via a recirculation system to limit the sample consumption.

An example that demonstrates the benefits of micro-focused X-ray beams is the analysis of colloidal liquids under high shear forces and significant deformation rates, which form microstructures under those conditions such as layered particles or flocculated systems [36]. It is of high interest to investigate such behavior in solution experiments because the nanoscopic structure influences macroscopic sample properties, such as viscosity and density [37-39]. Furthermore, one can understand the structure and dynamics of complex fluids under the impact of flow-induced shear concerning various sample ratios [40-42]. Another example is the tomographic SAXS experiment at P03 (PETRA III, DESY) [43] that benefited from the spatial resolution of micro-focused X-ray beam. These measurement techniques can reveal the in-flow particle alignment, i.e. the orientation of anisotropic micelles, in tapered microchannel by rotating and scanning the sample with the X-ray beam to map out the spatial distribution of nanoparticle

orientations inflow. Fig.1 shows the in-house experimental setups for in-flow experiments which involve micro-focused X-rays combined with a suitable microfluidic device system.

The recent development of XFELs has overcome the limitations of X-ray damage and their implementation in the emerging field of serial femtosecond crystallography (SFX) [44, 45]. The characteristics of XFEL radiation and associated sample environments have triggered the development of new data collection methods such as SFX. SFX is also an essential step towards the ultimate goal of performing atomic resolution single-particle imaging and record molecular movies [46-48]. However, this can lead to new problems concerning radiation damage. The continuous sample stream replenishment in the X-ray focus regime [49] is a possible way to avoid the issues related to X-ray radiation damage. This methodology needs sample environments that allow continuing flow of sample and reproducibility. In the experiments with these new types of X-ray sources, the high speed and micrometer-sized liquid jets have become one of the most frequently used sample delivery systems for several reasons. Most importantly, a jet is a fast and steady stream injection system that refreshes the sample continuously so that X-ray always hits fresh sample [50-52].

Further applications for microfluidic sample environments at synchrotrons and XFELs could be their use to produce stable thin liquid sheets for experiments X-ray spectroscopy such as transmission spectroscopy or angle-resolved XPS from well-defined (liquid) surfaces. Such stable and flat liquid sheets also offer further potential for special applications such as X-ray beam diagnostics. For such experiments, however, it is necessary to probe samples with limited thicknesses, i.e., from submicrometer to a few nanometer range, dictated by the cross-sections of the investigated molecular compounds in the (soft) X-ray spectral range [53-57]. From a fluid dynamic point of view, being able to predict the behavior of flat liquid jets and to tailor the injector design to the experimental needs will be highly beneficial for XFEL and synchrotron users. Therefore, the microfluidic flat liquid jet system with different flow types (sheets, droplets and whipping), offers excellent potential as a sample environment for XFELs and other synchrotron experiments due to the accessible design control and rapid fabrication routines. Additionally, these systems allow for the implementation of unique features, such as high aspect ratio microchannels, rapid micromixers, multiple-focusing zones and complete nozzle arrays for fast sample change during an experiment [58].

1.3 Fundamentals of microfluidics

Microfluidics is both the technology of manufacturing miniaturized devices containing microchannels through which fluids flow and the science which studies the behavior and control of fluids in microchannels [59-61]. This technology deals with phenomena at scales from ten to a few hundred micrometers. At such small scales, the forces that govern the behavior of many systems can be different from what we are used to at the macroscopic scale. During the past decades, microfluidics has quickly become an essential tool in several fields such as medicine, analytics, chemistry, physics, biology and engineering. Microfluidics deals with small volumes of fluids from 10^{-9} to 10^{-18} L using channel dimensions towards micrometers [62]. These microfluidic systems have several advantages, such as laminar flow or diffusion-based mixing with manipulation of fluids in channels with smaller sizes. These physical properties at the micron scale enabled the evolution of a variety of microfluidic tools for multiple research areas and more specifically, for biological analysis [63-66]**.** The micron-scale device makes microfluidic technology the ideal platform for portable, point-of-care diagnostic devices [67].

Miniaturization and microelectromechanical systems (MEMS) gave birth to microfluidics in the 1990s and today still constitute a large portion of this young discipline. Nowadays, a wide range of manufacturing- and industry sectors [68-69] use MEMS, micro opto electromechanical systems (MOEMS) and microfluidic systems. Microfluidics was realized initially as a sub-branch of MEMS technology for handling small amounts of fluids. Silicon was the primary material for the fabrication of these microfluidic devices. The typical microelectronic fabrication processes include photolithography, thin-film deposition and etching. These processes are surface-micromachining processes that can treat silicon surface of 1-6 inch in diameter. Today, many different deposition, bonding-, casting-, etching- and also new maskless patterning techniques are available to micromachine materials like polymers, glass, silicon and metals [70]. The critical fabrication process is still the photolithography. In this approach, the microstructures transferred to the wafer by selectively exposing a light-sensitive material (photoresist) and developing it to field a structured substrate [71, 72]. The recent developments of MEMS applications, namely micro total analysis systems (μTAS) or laboratory on-a-chip (LOC) operations, have been widely established and used in biochemistry, physics and engineering [73]. Fig.2 [74] shows the advantages of these systems.

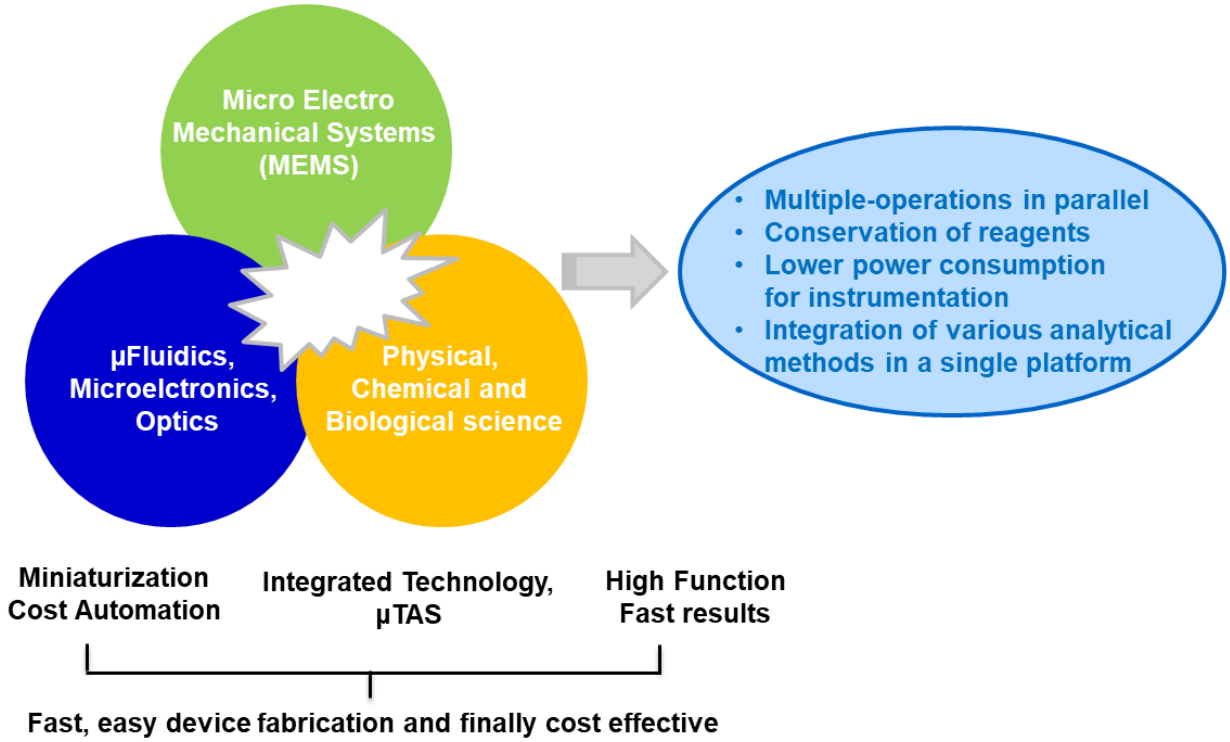

Fig.2: Technologies comprising for device development and future applications.

The field of microfluidics also offers many advantages when it comes to sample analysis in both academic and clinical research areas [75]. Recent rapid developments in the field of microfluidics have led to a vast array of novel technologies available for chemical analysis [76-79]. The benefits associated with promising chemistry in microfluidics is significant and a result of the scale-dependent processes of heat and mass transfer. Moreover, this gives rise to several advantages, including the ability to process improved reaction product selectivity, reduced reagent volumes, small reactor footprints, the acceleration of mass-transfer limited reactions, enhanced safety and facile routes to scale-out that have made the micro-reactor technology attractive as a synthetic tool [80-82]. Therefore, microfluidic reactors have found significant academic and industrial applications for the synthesis of nanomaterials, natural products and a range of small molecule drugs and pharmaceuticals [83]. Another emerging use of microfluidic systems is the handling and analysis of biological cells with X-ray studies [84]. However, chemical lysis is the most popular approach here due to its easy implementation into microfluidic devices, as it requires no dedicated equipment [85, 86].

Microfluidic channels are now being used to synthesize composite materials spanning the micro to nanometer scales. For example, multistep chemistry, rapid mixing and integrated separation steps make microfluidics a powerful platform for manufacturing fibers and a wide variety of nanomaterials, where shape, size and size distributions which are of incomparable precision [87-89]. Significantly, microfluidic devices readily allow for in-situ experiments and in most cases, continuous processes, both of which lead to higher process control and, thus, are preferred from an industrial point of view [90].

Furthermore, the combination of microfluidic technology and micro-focused X-ray facilities is a relatively new field of research [91]. However, the transfer of microfluidic technology to X-ray experiments is technically very challenging due to the interface between microfluidic construction and experimental X-ray data collection. In the case of connecting a microfluidic device with an X-ray beamline, it is essential to consider all aspects, such as choosing compatible X-ray materials, designing the detection window, the path lengths (X-ray though sample) and the interplay of flow rate (flow velocity) and exposure time to the beam. Moreover, increasingly strong X-ray beam intensities, available at both synchrotrons and XFELs facilities, require sample environments for being able to investigate the fast dynamics. One route to achieve this is through the use of microfluidic liquid jet sample injectors.

1.4 Microfluidic liquid jet devices for X-ray studies

The developments of increasingly bright and micro-focused synchrotron X-ray beams, as well as the advent of XFELs, reduce the requirements for both sample volume and data acquisition time. Furthermore, this creates new possibilities for various types and several sample conditions that can be examined but simultaneously increases the demands in terms of sample preparation and delivery [92].

During the past few years, the significant growth of microfluidics shifted to the introduction of new materials for the fabrication of microfluidic chips, primarily driven by the interest in time-resolved experiments at synchrotron beamlines [93]. The recent development of microfluidics enables to study the minimal amounts of samples such as membrane proteins or deoxyribonucleic acid (DNA). There is another field where 3D microfluidic device technology offers excellent

potential to analyses anisotropic particles under defined shear and elongation conditions [94]. The flow profile in the microfluidic channels may also be actively used, e.g., to shear the sample, leading to structural reordering or alignment, which can then be used to investigate them using the X-ray probing technologies.

The designs of the microfluidic chip, choice of material and fabrication method are essential factors to be considered in the fabrication of microfluidic devices for X-ray experiments. It has to be ensured that the rapid and low-cost manufacturing of material has to be well processable for the fabrication of modern microfluidic devices that allow microchannel geometries based on computer-aided design (CAD). Moreover, different materials such as PDMS, cyclic olefin copolymer (COC) and Kapton, each are having different optical and mechanical properties to withstand the applied pressures for handling the fluids. The above requirements generally require bonding, surface treatments/modifications and sealing steps for microchannel [95].

The fabrication approaches and their limitations, together with the proposed provisional application, mainly determine the size, shape and material of microchannels as well as the layout configuration of their arrays. The correct selection of materials used in the microfabrication process is necessary for the successful realization of advanced and low-cost microfluidic liquid jet devices.

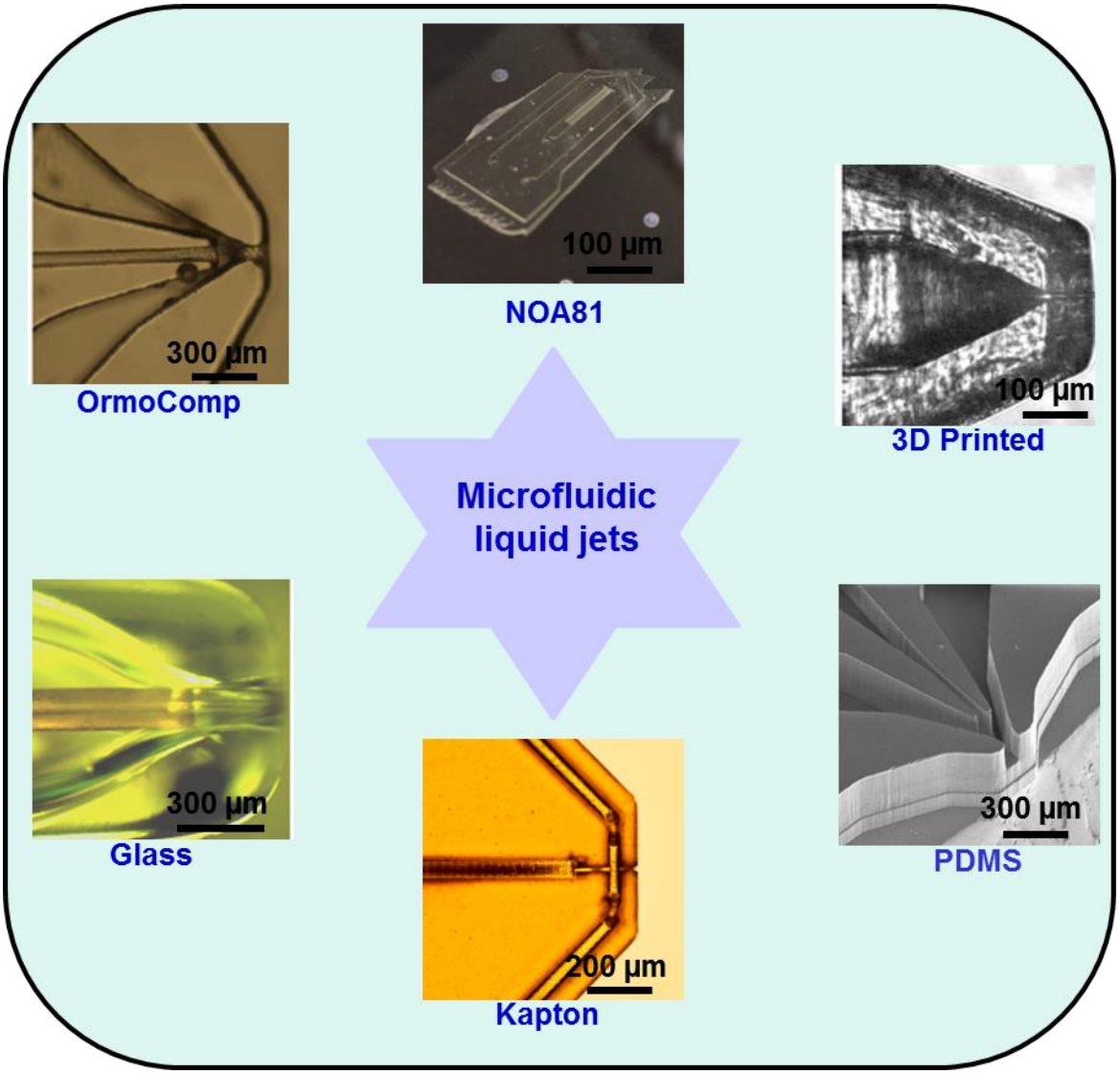

Fig.3: Illustration of different materials (glass [96], OrmoComp, Norland Optical Adhesive 81 (NOA81, Reproduced with permission from Trebbin, M.), 3D printed [97], PDMS [94] and Kapton jets [98], used in microfluidic liquid jet fabrication.

Over the past few years, a variety of techniques have been established for the fabrication of liquid jet devices including, soft lithography, hot micro embossing, laser machining and 3D printing [99-101]. However, most of these techniques present issues, such as complicated fabrication steps, geometry control, channel alignment and device placement at X-ray beam. Hence, design evolution, reproducibility and mass production are limited. To overcome these limitations, the

fabrication of microfluidic liquid jet devices based on soft-lithography has been established during the last years [102-104].

Many polymer materials were introduced to fabricate microfluidic devices/systems of which the soft lithography based poly-(dimethylsiloxane) (PDMS) is the most prominent one as it allows rapid prototyping and takes advantage of the high flexibility of design variations. Other material such as hard/rigid materials, in terms of material properties and compatible processing strategies (i.e., Kapton, silica and glass) usually depends on microfabrication techniques, which can be complicated and challenging to produce with same design flexibility as that of soft lithography. Fig. 3 shows an overview of the different available microfluidic device types suitable for liquid jet applications. And Table 1 describes that in more detail.

Table 1: Overview of the material properties based on literature and Trebbin lab sources for X-ray applications. Here the marks shows the (+ = good / o = neutral / - = bad) performance of the devices.

	Kapton	Glass	Ormo - Comp	NOA81	Photoresin	PDMS
X-ray resistance	+	+	o	o	o	-
X-ray transparency	+	-	+	+	o	-
Mechanical properties	+	+	+	+	+	-
Chemical stability	+	+	o	o	o	-
Temperature resistance	+	+	o	o	o	o
Vacuum compatibility	o	+	+	+	+	o
Prototype time frame	-	-	o	o	-	+
Design flexibility	o	-	+	+	o	+

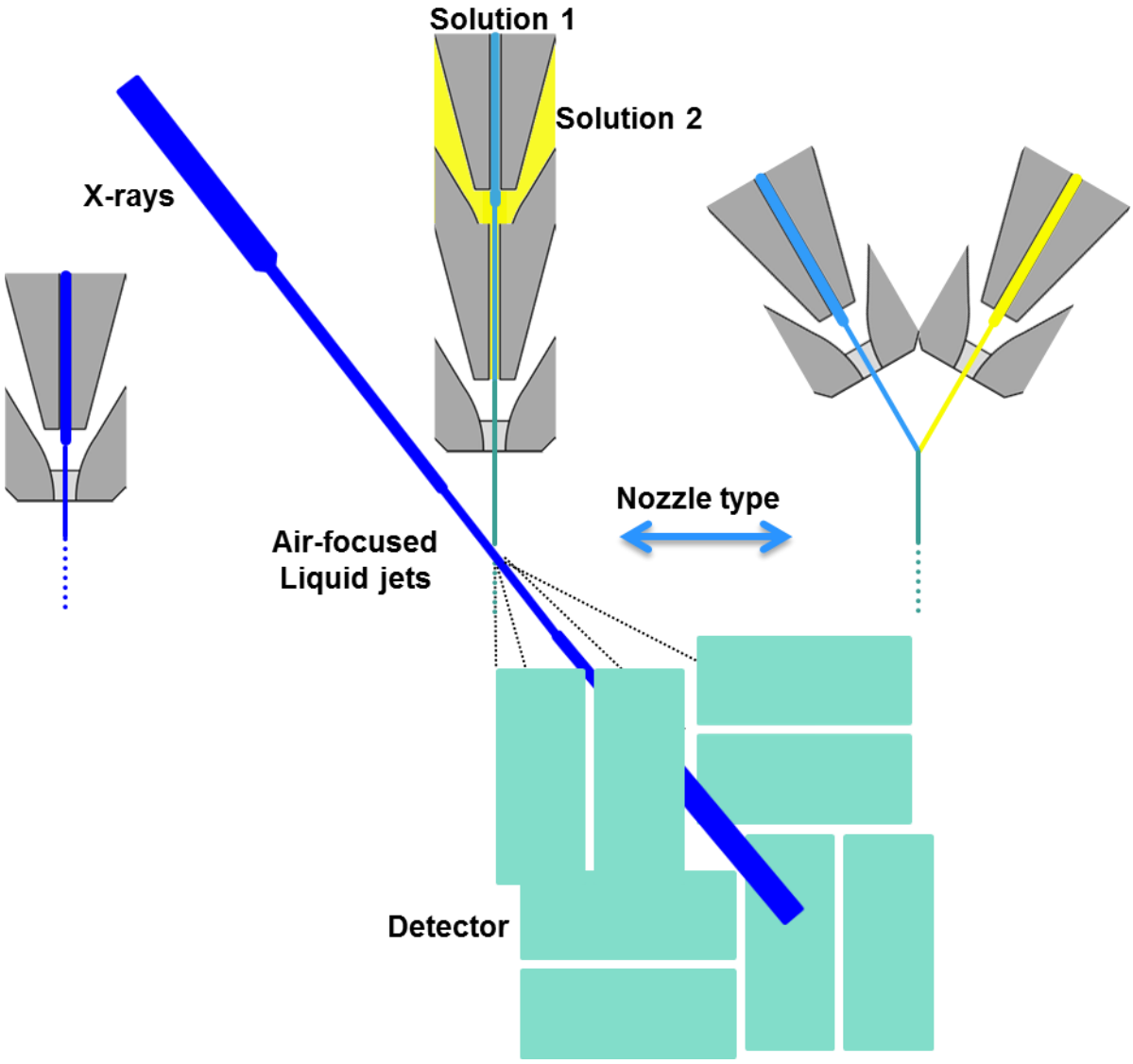

Fig. 4: Illustration of the experimental setup for combining the liquid jet principle with microfluidics. The advantages are that these novel microfluidic liquid jet devices enable fast nozzle changes, sample consumption and minimize wasted beamtime at the X-ray free-electron lasers (Reproduced with permission from Trebbin, M. [248]).

The recent development of 3D printing technology is now bridging the gap between micro and macro 3D printing terms of precision [105]. In comparison to other fabrication technologies, 3D printing nozzles/ liquid jets can print channels in sizes that range from a few hundred nanometers to several millimeters [106-108]. In particularly intriguing feature of the two-photon polymerization (2PP) 3D printing process is the ability to fabricate nested structures, which are

difficult or even impossible to achieve in conventional glass capillary, injection mold based GDVN nozzles [101]. This ability overcomes geometry constraints imposed by traditional fabrication processes, thereby facilitating the development of new types of injectors such as for the solution scattering, single-particle imaging, mixing nozzles, flow focusing and pulsed jets. However, the drawback of this 3D printed technique is an increased need optimization steps for complex internal geometries and it is hard to place the device at an X-ray beam due to lack of flexibility [109]. However, a critical advantage of photo- and soft lithography approaches is the fast and easy device fabrication, cost-effectiveness and that they are ideally suited for systematic screenings of nozzle micro-geometries. Additionally, these fabrication techniques allow for the implementation of unique features, such as high aspect ratio microchannels, rapid micromixers, multiple-focusing zones and complete nozzle arrays for fast sample change during an X-ray experiment as shown in Fig.4.

The key element of soft lithography is an elastomeric polymer, PDMS, that is used to replicate the desired patterns. PDMS consists of an inorganic siloxane backbone and attached organic methyl groups. The PDMS can easily be converted into a solid by cross-linking. [71] In the 1990's, Whitesides and co-workers published several papers using PDMS as elastomeric mold for micrometer patterned devices. PDMS offers a decent replication resolution, is optically transparent, non-toxic and has much lower costs per volumes compared to silicon [110]. Due to the latter fact, the fabrication is still cost-efficient at small quantities, which are essential for rapid prototyping and often-changing microstructures. PDMS functions in a wide range of temperatures (-50 up to 250 °C) and common solvents such as water, acetone, methanol and ethanol [111].

In this thesis, microfluidic flat liquid jet based devices that produce stable liquid sheets with few micrometer thicknesses are presented. These GDVN based microfluidic flat liquid jet devices offer unique characteristics such as precise delivery of small sample volumes in the mL/h-range and potentially high throughput analysis [112, 113]. This approach would allow minimizing sample consumption up to tenfolds in comparison to the traditional colliding jets (i.e., non-gas focused/impinging) for thin flat sheets [114-116]. Also, another advantage of this technique is that the liquid does not contact the nozzle exit surface, which allows for smooth and reproducible operation of the nozzle for long periods. These gas-focused microfluidic flat liquid jet devices

offer a sample environment that allows for interdisciplinary studies and have first been shown in the past few years, such as fast analytical systems, spectroscopy, nanorheology and fiber spinning applications [117, 118].

1.4.1 Spectroscopy

Previously, cylindrical liquid jets have been used for spectroscopic applications, but the problems with these jets are (i) photon scattering and (ii) refraction due to the cylindrical liquid boundary. Recently, an upsurge in flat liquid sheet-based sample delivery for X-ray experiments can be observed to understand local molecular integrations in neat liquids and solutions. It has increased due to the need for continuous sample replacement at strong photon sources. One reason is that for experiments in absorption, i.e. X-ray spectroscopy. When it comes to experiments in reflection configuration, i.e. XFEL beam position monitoring, optical flatness and spatial stability, are also critically important [119-121]. As well as, stable liquid sheets of thicknesses submicron range helps to minimize any unwanted background signal from the liquid when used as a sample carrier. Finally, incorporating mixing strategies and fast hydrodynamic focusing with stable sheet generation can be ideal for quick reaction studies.

1.4.2 Nanorheology

The orientation of particles is relevant for the behavior of various human-made and biological materials. It determines the material properties of molded or spun fibers, influencing the flow of particles and cells through capillaries and the aggregation of proteins. In silk fibers and nanocomposite materials such as CNT-enhanced polymers, the alignment of the particles is crucial for the mechanical properties [39, 122-125]. Microfluidic liquid jet systems represent a versatile tool to precisely control fluids, study the alignment of liquids and analyze dispersed particles. Hence, this technology is very attractive for studying nano-rheology in colloidal liquids [126-128]. However, a detailed characterization of the shear- and orientation effects on the sample within the liquid sheet is missing [129]. This knowledge will not only be highly beneficial for controlled experiments of colloids under extreme shear conditions, but also for fine-tuning the nozzle designs to minimize stressful effects on soft samples, such as micron-sized membrane

protein crystals, for optimizing the sample injection at high-intensity X-ray sources (i.e. XFELs, 3rd generation synchrotrons) [120-132].

1.4.3 Fiber spinning

Whether in nature or modern industry, micro-/nanofibers are ubiquitous because of their unique properties and utility. On account of their high specific area, surface roughness and strong interfacial interactions, micro-/nanofibers are already applied in textile fabrics, as reinforced materials in tissue engineering, high performance filters and as optical sensors [133]. A variety of techniques can be used for the fabrication of continuous (or end-less) microfibers such as melt spinning, wet spinning, coaxial spinning, electrospinning and blow spinning [134-138]. However, most fibers generated by these techniques suffer from shape- and size-nonuniformity. Furthermore, manufacturing problems such as clogging of the hardware, complex setups and low-throughput pose industrial obstacles. Therefore, the fabrication of continuous submicron/nanofibers with tunable morphologies and uni-formity remains a great challenge [139-144].

Electrospinning is the only well-developed technique for fabricating nanofibers, making it the current state of the art manufacturing process [139, 145-147], even though it has a number of major drawbacks. Electrospinning requires hazardous operating conditions such as high voltages and in most cases the use of toxic and volatile organic solvents. The manufacturing conditions are also highly susceptible to local environmental changes, such as temperature or humidity, which can make reproducibility an enormous challenge. Thus, all of these factors need to be carefully controlled and have called for the development of new techniques for nanofiber spinning. One such technique is solution blow spinning, which also allows the fabrication of fibers in the nm-range without the need of a high voltage gradient, which can be advantageous when working with cells or other bio-systems [148, 149]. Additionally, this fabrication process is performed under atmospheric pressure, does not involve harsh chemical conditions and can be carried out at room temperature [150]. Nevertheless, blow spinning is still in the state of initial development [151] and fabrication of customized nozzles is challenging. One possible way around this difficulty is to employ well-established soft lithographic techniques used in the fabrication of microfluidic devices to facilitate nozzle production. Microfluidic approaches allow for fast prototyping and

easy mass production of the nozzles. Furthermore, the miniaturized nature of the device reduces the needed space for a spinning setup and allows easy nozzle parallelization for high throughput operation with excellent reproducibility [139].

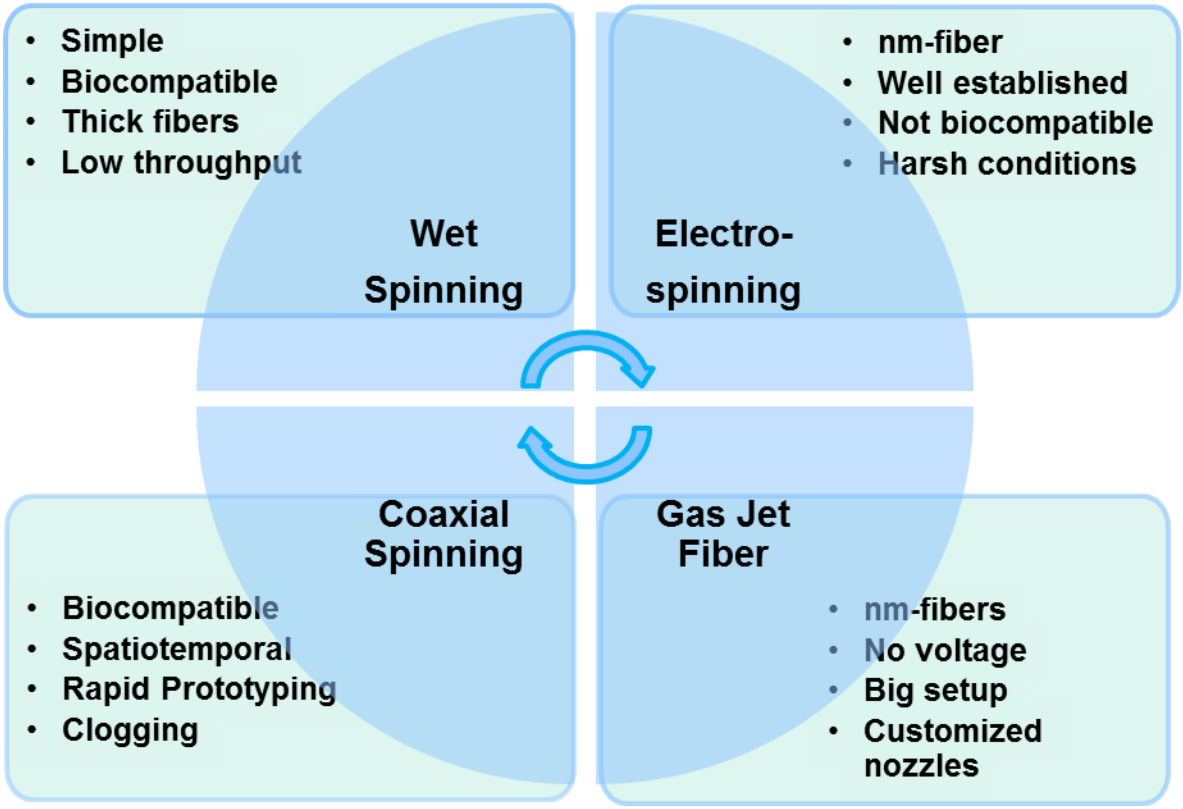

Fig. 5: Illustration of drawbacks of several techniques used for the fabrication of microfibers.

Several fibers have been successfully spun using microfluidic techniques, but to our knowledge, single fibers with controlled diameters in the nm-range have not yet been achieved via the here-presented microfluidic approach [139, 152-154]. Developing a new method for spinning fibers using Gas Dynamic Virtual Nozzles (GDVN) microfluidic devices allows the combination of advantages from coaxial spinning, electrospinning and blow spinning, while minimizing the current drawbacks of the individual techniques. GDVNs have been developed to allow the formation of free-standing liquid jets by gas-flow-focusing liquid samples [155]. The main advantage of this GDVN-technique is that the liquid does not contact the nozzle exit surface which allows for smooth, reproducible and continuous operation of the nozzle for long periods of time by avoiding the deposition of material at the nozzle exit.

2. Theoretical background: flow characteristics

The dynamics of fluids at microscopic scales are found to be significantly different than those observed at the macroscopic scales. For example, in microscopic scales, the surface to volume ratio increases to a larger extent, resulting in a considerable change in the surface and interfacial properties of the material [156]. It is beneficial to develop a physical understanding of the phenomena that are becoming dominant at the microscale; this understanding will allow us to categorize and target micro designs and to fabricate them from computer-designed photomasks using lithography reproducibly. These designs can be optimized before the actual device fabrication by numerically predicting the fluid flow via computational fluid dynamics (CFD) and, therefore, enable simulation-based rapid prototyping.

The liquid jets produced from the microfluidic nozzles have paved themselves for considerable importance in the past few decades through their continuous utilization in advanced technological fields like biomedicine, bioanalytics and nanorheology [157-159]. Recently, they have started being utilized to deliver samples in SFX (Serial Femtosecond X-ray crystallography) experiments [160]. Many of the samples studied using SFX applications are hard to crystallize protein samples that are only available in limited amounts. Hence, low consumption and an efficient sample delivery system are required for these hard to prepare, precious samples [161]. The present chapter deals with a two-phase (gas/ liquid) flow problem, where a gas co-flows with a liquid stream and shaping it in the form of a jet by transferring momentum to it. This chapter studies the effects of the gas on the liquid and instability problems based on the capillary-to-orifice distance, nozzle outlet orifice diameter and nozzle height.

2.1 Flow focusing microfluidic liquid jets

Understanding the flow behavior of the microfluidic liquid jets and the physical parameters behind them is necessary to study the different areas related to the flows. From this short review, the jet, breakup, droplet, sheet and whipping regimes depend on the liquid/gas flow rates, nozzle designs, viscosity, density and surface tension on the jet. Therefore, the information of the jet properties is essential to study its performance in different microfluidic liquid jet devices [162-165]. Thus to develop or upgrade the design of the new sample microfluidic flat liquid jet

systems, these flow properties should be taken into account. The use of different microfluidic liquid jet devices became famous with the advent of micro-focused X-ray Free-Electron Lasers (XFELs) and synchrotron sources [166, 167]. These sample environments are critical in the control of the jets, samples and flow studies.

2.1.1. Rayleigh nozzles and droplet generation

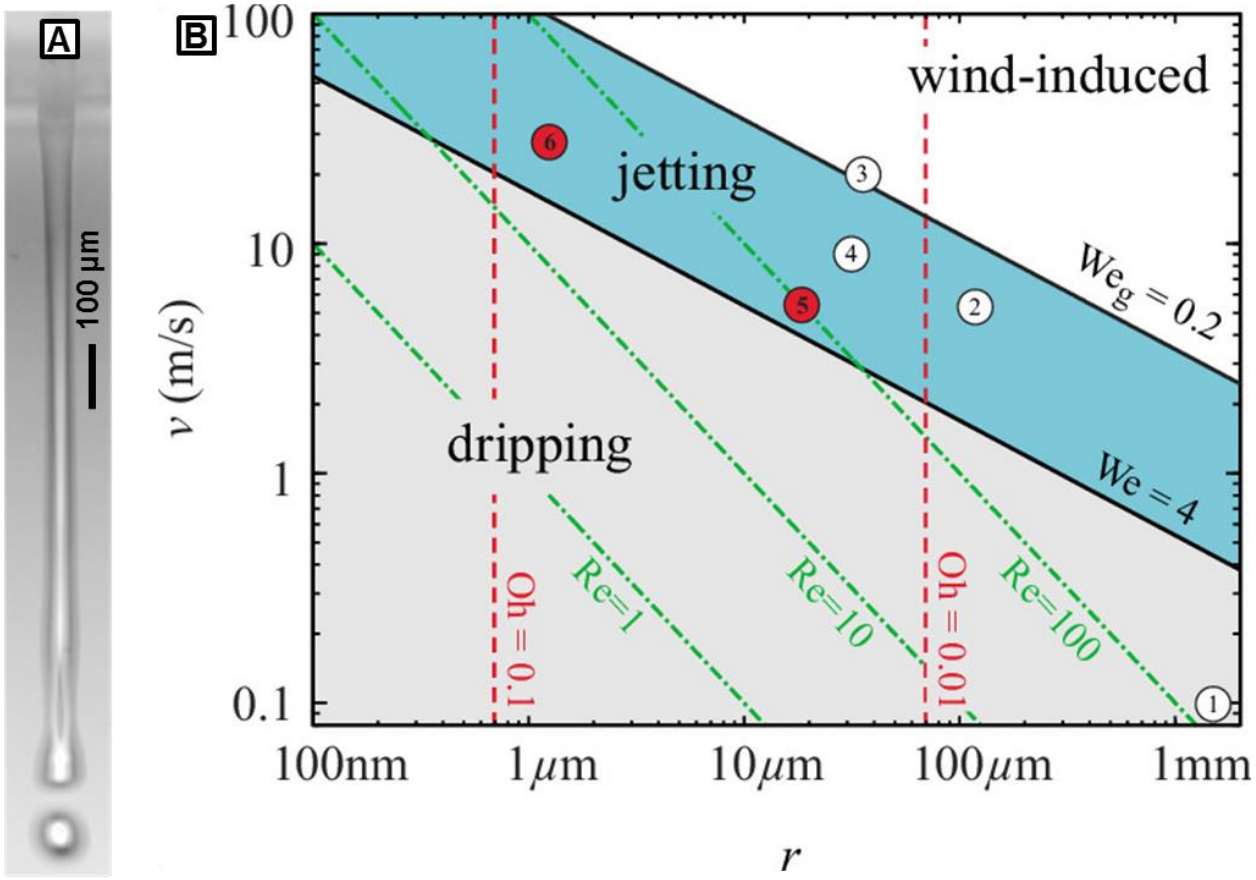

Fig.6: (A) typical snapshot of Rayleigh nozzle, (B) Classification of droplet formation regimes for a liquid discharging an orifice of radius r with liquid velocity v. Droplet formation through the Rayleigh breakup mechanism in jetting is bounded by a lower and upper critical jet velocity (Image from [170], copyright Lohse D.).

Liquid jets based on the Rayleigh concept, as shown in Fig. 6 (A), are produced by discharging liquid from a channel through an orifice. In 1878 Rayleigh showed the first mathematical study of the mechanism responsible for instabilities of jets generated by liquid nozzles [168]. A steady liquid jet is emanated from the nozzle only when equilibrium is maintained between the

interfacial and momentum forces in the fluid. At very low flow rates when the liquid momentum forces are not strong enough to overcome capillary forces, a stream of droplets is produced (dripping), which slowly grows in size, as shown in Fig.6 [169].

Later, Weber had started in 1931 by including the effect of viscosity on the stability of a liquid jet under the influence of surface tension from Rayleigh's analysis [170]. Fig. 6 (B) shows a classification of the dripping and jetting regimes of Rayleigh nozzles. Hilbing and Heister in 1996 used a boundary element method to study the nonlinear nature of the instability [171]. They explained the mechanism of satellite droplets formation and that it depends on the magnitude of disturbance, the Weber number (We) and the wavelength. At the break-up point, the jet radius goes to zero. Moreover, this is due to the velocity of the jet, which goes to infinity. These singular phenomenons were further studied by Eggers using Navier-Stokes equations to derive a one-dimensional model describing the break-up region [172].

As Rayleigh jets require higher liquid flow rates, it is not economical while being operated for precious samples. These issues with Rayleigh jets motivated research in the development of a robust apparatus for producing liquid jets.

2.1.2. Macroscopic GDVNs (Plate orifice nozzles)

A new class of microscopic fluid jet flows satisfies two requirements i) minimum flow rates and ii) steady jets. In this case, a force initiated by a co-flowing stream stretches an inner fluid meniscus until a thin fluid ligament is ejected [173]. Later, the work started by Ganan-Calvo with modeling studies is considered as a step forward in the fabrication of controlled micron-sized flow geometries [174]. The critical geometrical parameters determining the behavior of liquid at nozzle outlet are orifice diameter D and capillary-to-orifice distance H, as shown in Fig.7.

However, the plate-orifice nozzle geometry presents significant drawbacks: (i) orifice surface (ii) the sharp edges of the orifice due to the strong recirculation close to the orifice surfaces and (iii) the minimum sizes of round orifices fabricated with conventional techniques are limited to tens of microns [175]. Since the drop/jet diameter from the plate orifice nozzle depends upon the orifice diameter, this apparatus has limitations in the fabrication of smaller diameter jets. It can

produce the jet diameters of the size ranging between 10-200 µm, which is not realistic for X-ray experiments as it increases the background signal [176].

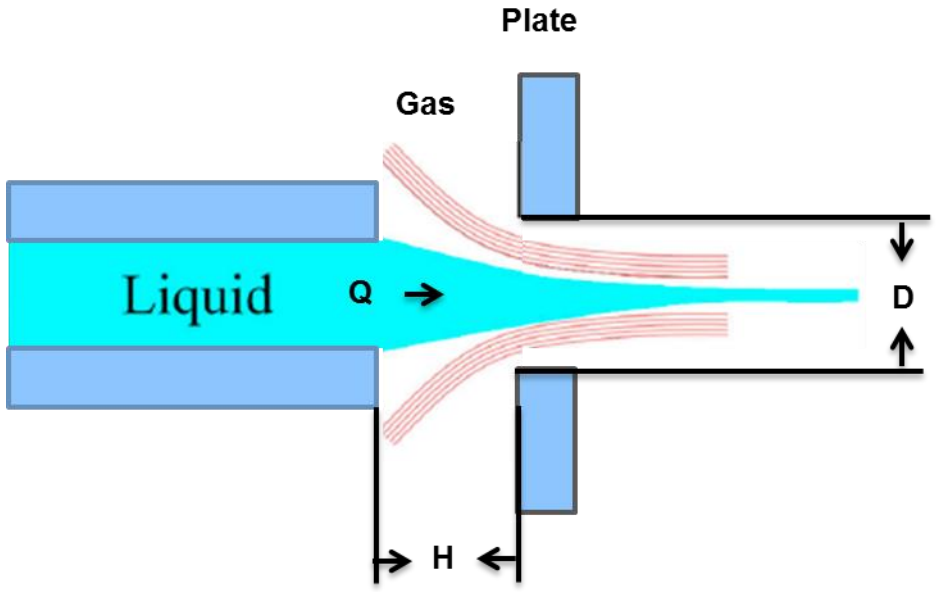

Fig.7: Illustration of a general macroscopic GDVNs design for the generation of liquid jets and the involved geometric parameter (Reproduced with permission from Sasa, B.) [177]. The main geometrical parameters of the fluid configuration are diameter D, flow rate Q and the capillary-to-orifice distance H.

The concept of a GDVNs technology is a modification of the Rayleigh nozzle and dates back to Ganan-Calvo et al. [178]. They developed the gas-focusing technique, which works with a gas stream surrounding the liquid jet. In the nozzles with flow-focusing arrangement, a hydrodynamic effect of a co-flowing gas is used to shape the liquid jet in a plate-orifice apparatus. Such a plate-orifice device was miniaturized to a flame polished converging nozzle, called GDVNs [157, 179-181].

2.1.3. Microscopic GDVNs

In this GDVNs principle, the flow and the shape of a liquid, e. g. diluted anisotropic particles is controlled by a gas flow towards the nozzle's exit. Therefore, a continuous liquid jet/sheet is formed smaller than the liquid inlet geometry. A different breakup process of liquid jet and

droplets has explained in terms of co-flow and flow-focusing microfluidic liquid jets [182-184]. Commonly used GDVN for synchrotron applications and studies are made using glass capillaries [185]. However, the fabrication of those nozzles requires many complicated steps such as flame polishing, grinding of the tip and, most importantly the alignment of the inner to the outer capillary. The procedure does not reproduce geometries well and due to the different manual fabrication steps, the nozzle dimensions and flow-focusing behavior may differ between individual nozzles making controlled geometry studies hard to realize. The high demand for liquid jets and aerosol generators for X-ray experiments requires an alternative technique in fabricating GDVN faster and more reliable [186].

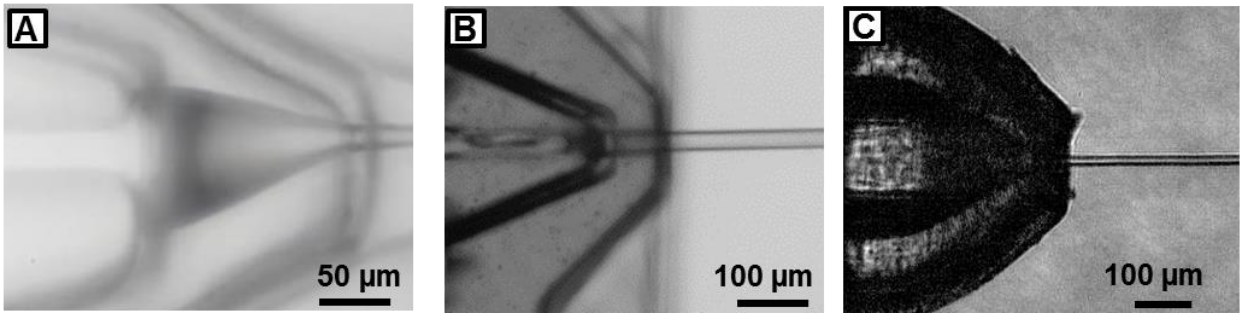

Fig.8: Microfluidic liquid jet systems with different fabrication techniques such as (A) soft lithography [Reproduced with permission from Trebbin, M., 7], (B) laser machining [98] and (C) 3D printing [Reproduced with permission from Nette, J., 97].

Later Trebbin et al. started to develop innovative microfluidic liquid jet devices with different lithographic fabrication techniques such as soft lithography, laser micro-machining and 3D nano-printing for GDVN production as shown in Fig. 8 [98, 94, 97]. With alternative fabrication routes, other microfluidic features become available such as mixing, integrated piezoelectric actuators, smart sorting and multiple-gas focusing inlets on generating monodisperse nano- and micro-droplets. In order to achieve a more efficient and more reproducible fabrication route, lithography based approaches are the most promising candidates. Since the miniaturized lithography based devices have mass flow rate for sample focusing it is a promising approach to achieve higher signal to noise ratios for diffraction studies, due to less diffraction of the X-ray with the gas molecules [187, 188].

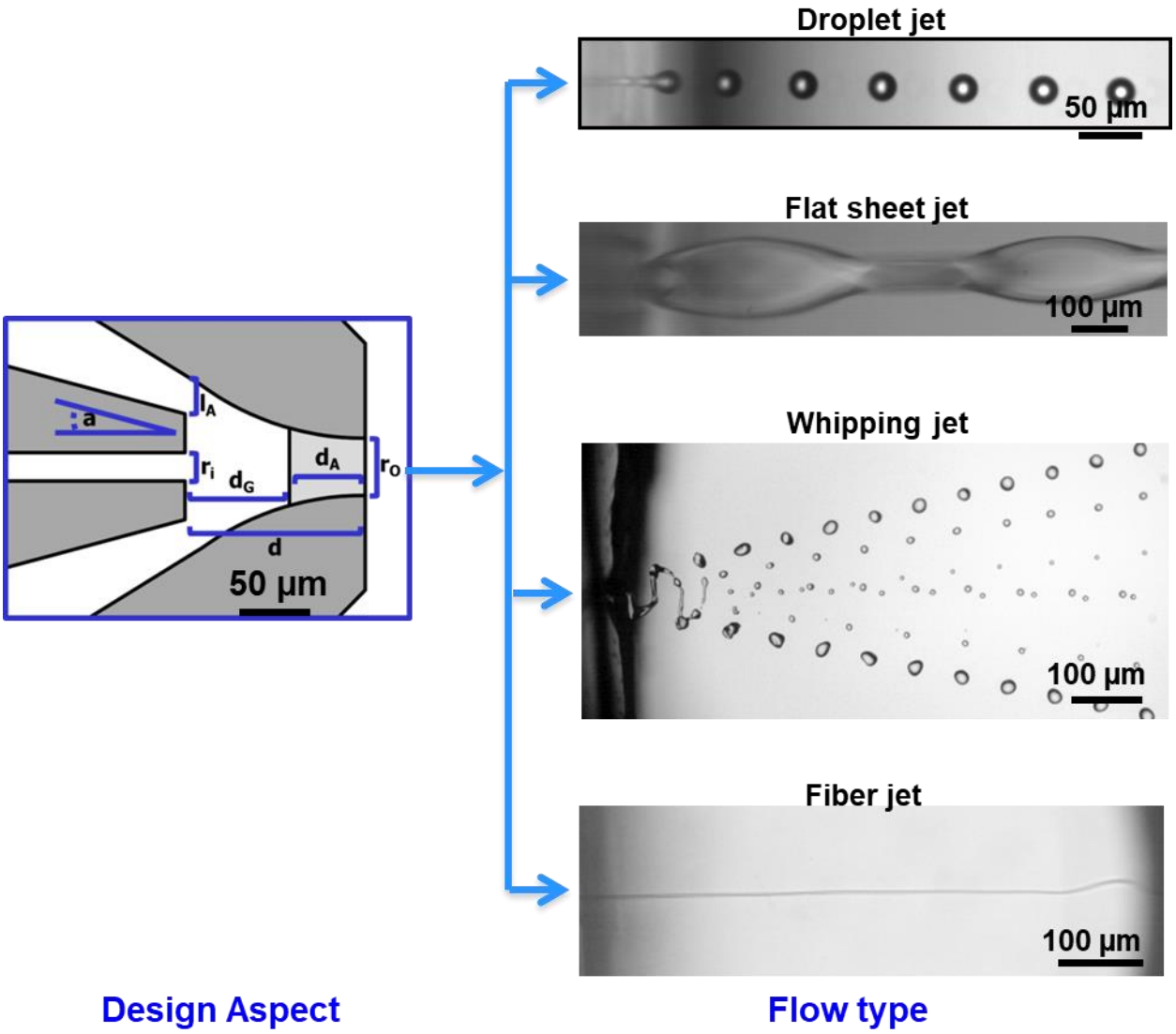

Fig.9: Optimization of nozzle parameters [7, 10, 189] to form different flow of liquid jets, which are droplets, stable sheets, whipping droplets and fiber jets.

One goal of this work is the development of a flat liquid jet environment with a GDVN and the needed diagnostics for experiments on liquids to enable the research of complex fluids such as colloidal dispersions and molecular liquids with X-ray scattering/spectroscopy. For this purpose, first experiments with high aspect ratio nozzle fabrication to produce stable liquid sheets were performed. Hence, in the framework of this thesis, the GDVN and the optimization nozzle parameters are used to form different flow of liquid jets such as stable liquid sheets, droplets, whipping droplets, bubble jets and fiber jets, as shown in Fig. 9.

2.2 Difference between GDVNs and other flat liquid jet systems

A variety of techniques is established in few years for liquid thin sheet formation such as impinging liquid jets [190], wire-guided flow jet (WGJ) system [191] and non-gas focused slit nozzles [192]. However, most of the thin sheets generated using these techniques have issues, for example, stable liquid sheet formation, long-term stability, volume consumption, *in-situ* experiments, etc. [193, 194]. These issues are addressed by microfluidic flat liquid jet devices which apply the GDVN-principle to a flexible and precisely manufacturable nozzle design [195].

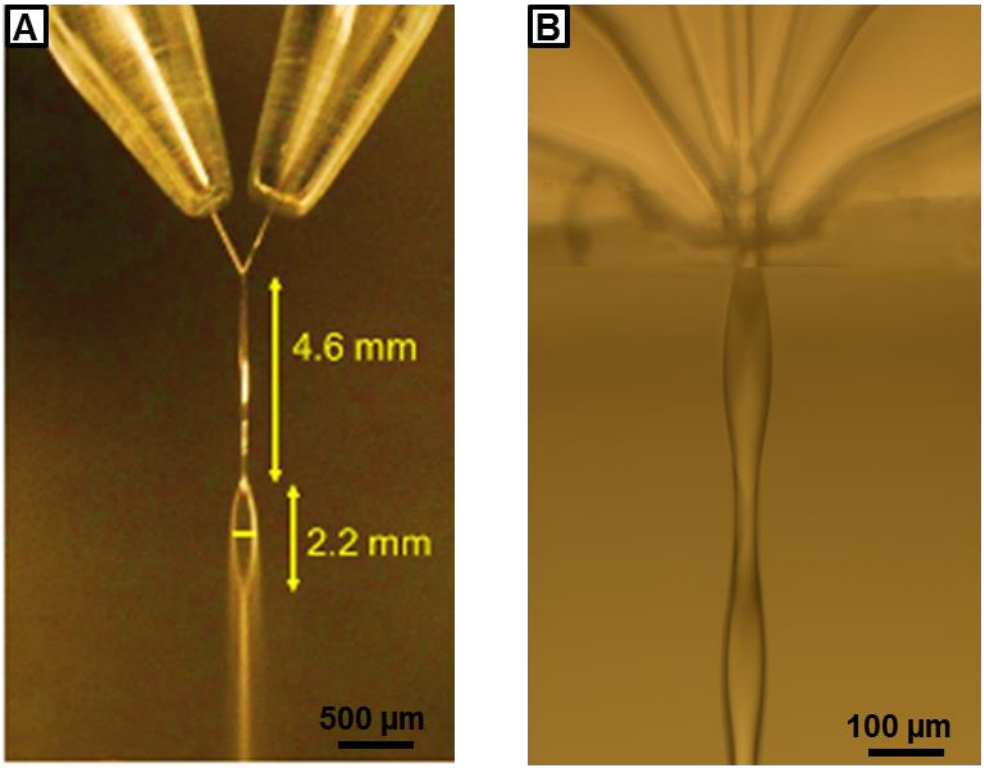

Fig.10: Photo of the flat liquid jet taken from (A) impinging liquid jets (Image from [6] copyright Nibbering T.J.) and (B) microfluidic flat liquid jet at flow rate at 60 mL/h using GDVN principle.

A later adaptation of this principle introduced the generation of micrometer-sized liquid sheets using three carefully assembled microfluidic channels in a borosilicate chip [196]. However, the production of such devices requires complicated fabrication steps, for example, careful glass etching process, channel alignment and device placement at beamtime experiments. However, the complicated assembly process and geometry control and production rate currently limit the

reproducibility of such liquid jet devices. However, a critical advantage of the fabricated flat liquid jet devices using soft-lithography is the much more relaxed approach to fabricate such high aspect ratio nozzles, as shown in Fig.10.

2.3 Governing equations of incompressible flow for Newtonian fluids

The descriptions of the dynamics of Newtonian fluids are based on the conservation of mass, momentum and energy principles. By considering the flow properties (density, viscosity, surface tension) of pressure and temperature, the energy equation is also included. Moreover, this leads to a set of two partial differential equations (PDE), called Navier-Stokes equations. The Naiver-Stokes equation is a set of two-second order PDEs and can be written as [197]

$$\rho\left[\frac{\partial \mathbf{v}}{\partial t} + (\mathbf{v}.\nabla)\mathbf{v}\right] = \eta\nabla^2\mathbf{v} - \nabla \mathrm{p} + \mathbf{F} \tag{1}$$

Here, the dynamic viscosity as η, fluid density is ρ and **v** expresses the velocity of the fluid flow. **∇** is the Nabla operator and **F** denotes additional long-range forces per unit volume directed to the fluid. The left part of the equation is the acceleration term, whereas the right part describes the forces acting on the fluid. These PDEs can be solved numerically by computational fluid dynamics (CFD) simulations. For this task, the finite volume method (FVM) is used [198].

2.3.1 Conservation laws

The major governing equations describing the physics of Newtonian fluid flow are the Navier-Stokes equations based on the mass, momentum and energy conservation principles. The study of microfluidic flat liquid jets is based on the conservation of three extensive quantities, namely, the mass, total energy and the total momentum. By the law of conservation of mass, the total mass entering the microfluidic device must be in balance with the one leaving the nozzle. Moreover, the mass of the system indeed remains constant overtime throughout the jetting regime. The system conserves its momentum by balancing the total momentum with the net forces acting on the fluid regime. Considering the entire liquid emanating in the fluid domain to be incompressible, isothermal Newtonian fluid, one can solve the famous Navier-Stokes equations, which describe the micro-scale fluid flow of these liquid sheets. Also, it is noted that the viscous

friction has different microscopic origins and hence, this is an essential factor to be considered while understanding the dynamics of fluids at micro and nanoscales [199, 200].

2.3.2 Condition for incompressibility

If the fluid is incompressible, that means ρ =constant, so that the condition eliminates from the fluid-dynamic system the mass continuity equation and considerably simplifies the Navier-Stokes equation. Contrary to gases, liquids can be compressed only using very high forces. Therefore, a fluid behaves almost like an incompressible material, i.e.,

$$\nabla . \mathbf{v} = 0 \tag{2}$$

Which is Cartesian coordinates id

$$\frac{\partial \mathbf{u}}{\partial \mathrm{x}} + \frac{\partial \mathbf{v}}{\partial \mathrm{y}} + \frac{\partial \mathbf{w}}{\partial \mathrm{z}} = 0 \tag{3}$$

In momentum equation

$$\rho \frac{\mathrm{D}\mathbf{v}}{\mathrm{D}t} = -\nabla \mathrm{p} + \mu \nabla \mathbf{v} \tag{4}$$

Incompressibility is not a property that can be enforced in a physically justified way by means of an external condition. Incompressible behavior, if existing, will have to follow self-consistently from the full system of transport equations [201].

2.3.3 Boundary Conditions

After determining all relevant aspects, the boundary conditions are translated into mathematical relations, where one arrives at a system of partial differential equations for various field quantities, which have to be solved in a suitable domain. Moreover, appropriate boundary conditions are needed, taking into account physical conditions. In order to consider any flow domain, the flow equations must be solved, which is subjected to a set of circumstances that act at the domain boundary [202, 203]. For a rigid boundary condition, wall moving at velocity **u** and having unit normal $\hat{\boldsymbol{n}}$**,** we assume for the local fluid velocity **v** that, the wall is impermeable: $\mathbf{v} \cdot \hat{\boldsymbol{n}} = \mathbf{u} \cdot \hat{\boldsymbol{n}}$.

2.4 Nonlinear flow problems

The fluid flow phenomenon of macro and micro scale environment is entirely different due to the length scale effects. As a consequence, in microscale, viscous dissipation, as well as pressure effects, dominate over inertia and result in a laminar flow without any turbulence [204]. Nowadays, most of the microsystems which are of attention to science and their applications are non-linear due to the complexity of nature [205]. So, now, it is essential to understand the fundamental physical phenomena and fluid flow properties. Further, when it comes to micron to submicron, these systems can lead to interesting non-linear scientific problems, of which a few examples will be discussed below.

2.4.1 Fluids and interfaces

The surface to volume ratio in microfluidic channels is very high and this is why surface properties have a more significant influence on the fluid dynamics [206]. In general, in the microfluidic channels, the hydrodynamic interactions between solids and liquids can be described using the no-slip condition [207]. The velocity vector of a flowing fluid is assumed to be zero at the wall. This condition remains valid in the sub-micron range, which has been shown by molecular dynamics calculations that assumed a hydrodynamic wall that corresponds to a monomolecular layer of fluid molecules resting on a solid wall.

The Navier boundary condition can be applied while describing the interaction of a flowing fluid and a solid surface. It is based on the assumption that the flow velocity $\mathbf{v_x}$ parallel to the surface is proportional to the shear stress at the surface.

$$\mathbf{v}_x = \boldsymbol{\lambda} \frac{d\mathbf{v}_x}{dy} \tag{5}$$

Where $\boldsymbol{\lambda}$ denotes the slip length or Navier length [208]. The slip length can be illustrated as the distance between the surface and an imaginary point inside the solid wall, where the velocity profile extrapolates to zero, as drawn in Fig.11.

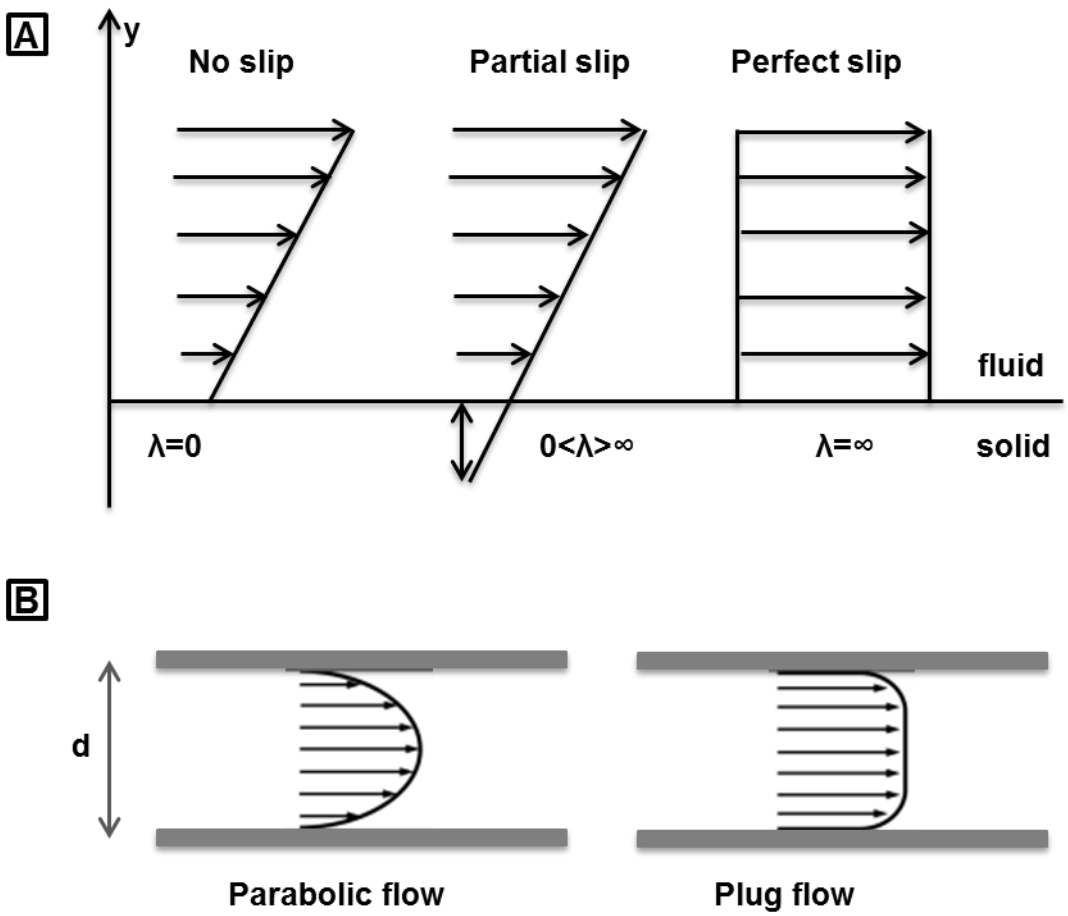

Fig.11: (A) Schematic illustration of the Navier length λ for no-slip (left), partial slip (middle) and perfect slip (right) condition. (B) Flow velocity profiles for parabolic (left) and plug (right) flow.

2.4.2 Liquid jet stability

For analytical reasons, it is essential to generate a stable liquid sheet and droplet breakup regions [209-211]. Therefore, Ganan-Calvo et al. started to investigate the hydrodynamic stability of the liquid jet concerning its initial moment of droplet generation [212]. Microfluidic flat liquid jet stability is one of the most important considerations when designing nozzles for synchrotron and XFEL experiments [213]. Microfluidic flat liquid jets starting from the capillaries under the influence of momentum being transferred to them from another co-flowing (gas) has received an increasing amount of interest over the last few decades [214-216]. Stability of the jet summarizes (in Fig.12), the work that has been carried on the jet/sheet formation and breakup physics when co-flowing with the gas streams. For experimental validation, some numerical studies performed

were overtime to understanding the jet/sheet formation and breakup mechanism. The experimental phase diagram for particular nozzle studied the stability of jets formed by a GDVN and identified three different regimes: (I) the steady jetting regime, where the liquid meniscus and the jet are stable; (II) whipping regime, where the meniscus is and jet is unstable; and (III) the dripping regime, where the liquid meniscus is unstable and the jet is not formed, as shown in Fig.12.

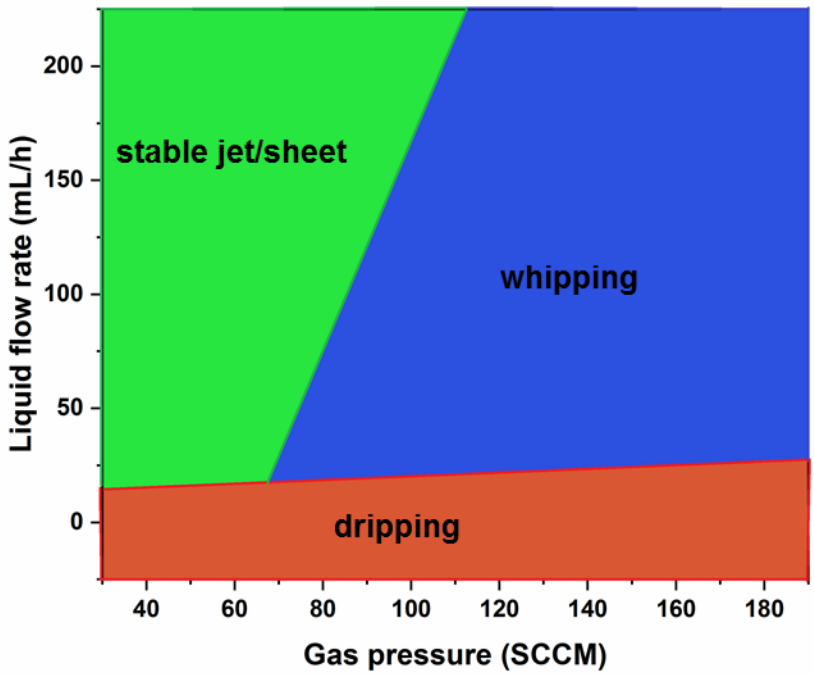

Fig.12: The experimentally obtained jet stability phase diagram shows three distinct regimes for a high aspect ratio nozzle flowing water with a liquid capillary inner diameter of 100 x 15 µm (hxw) and distance of the gap between main channel inlets is 355 µm.

The change in design aspects and gas/liquid flow rates alter the influence of liquid inertia and surface forces on the jet, allowing its breakup to fall into different categories: dripping, jetting and whipping are shown in Fig.13. As the liquid jet emanates from the nozzle outlet, it is subjected to different instabilities that determine its behavior. These instabilities are extreme due to the dominant aerodynamic interaction at the interface. The breakup due to these instabilities is sometimes also known as an air-assisted breakup due to gas focusing. The primary factors that define the jetting regime (jetting/dripping/whipping) are the geometry of the apparatus, material properties such as viscosity, the flow rates of liquid and gas, pressure gradient over the nozzle,

which depends on the mass flow rates and the geometry [Fig.29]. Thus, understanding the effect of the parameters mentioned above on the jet stability and its shape is required for proper nozzle design [217].

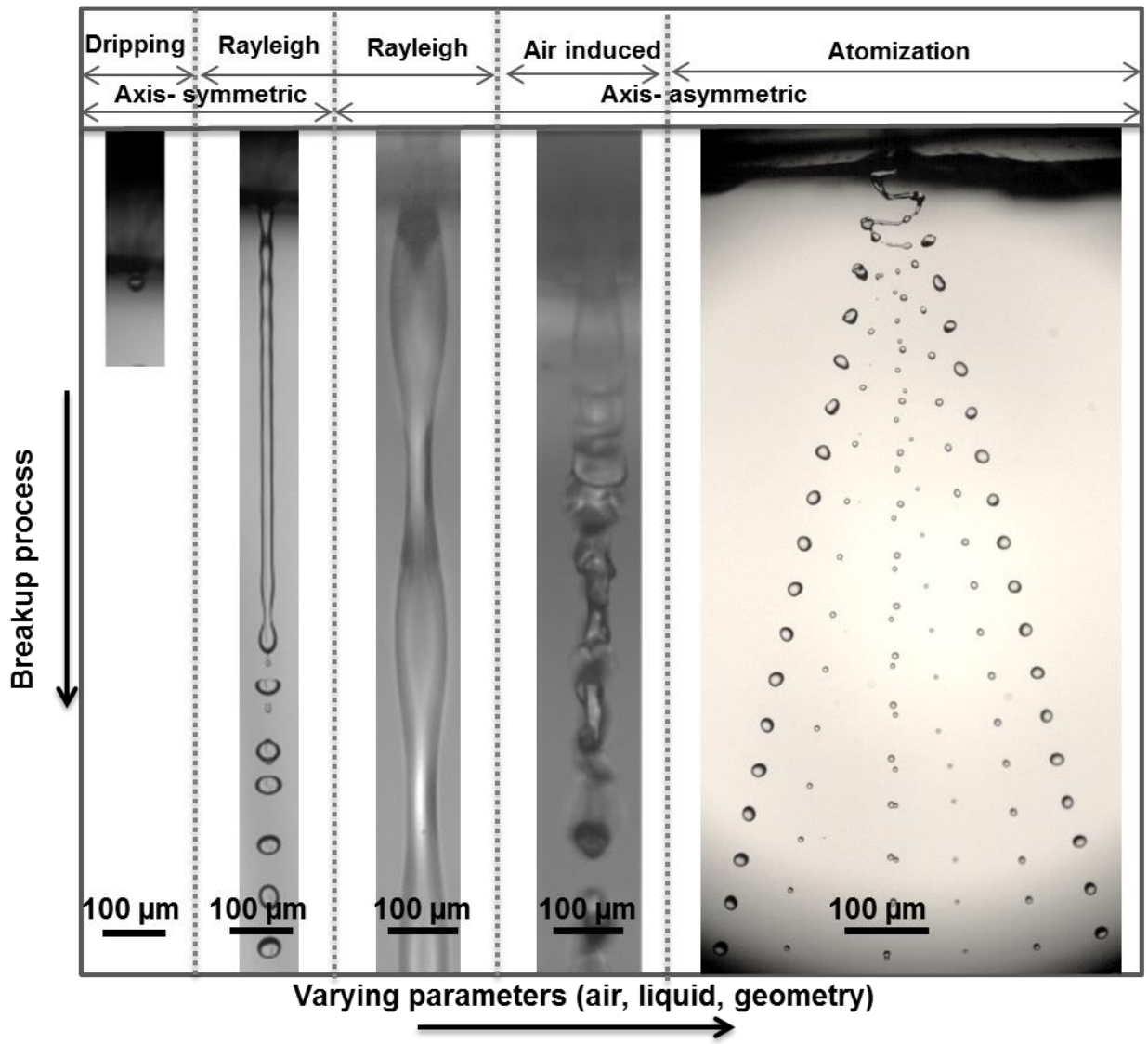

Fig. 13: Stability of a liquid jet in gas-focused microfluidic liquid jet system showing different breakup classes.

The non-dimensional numbers involved are Reynolds number (Re), Peclet number (Pe) and the Weber number (We). These non-dimensional numbers are defined as,

$$\mathrm{Re} = \frac{\rho v D}{\mu} \tag{6}$$

$$\mathrm{Pe} = \frac{Lv}{D} \tag{7}$$

$$We = \frac{\rho v^2 D}{\sigma} \quad (8)$$

Where D is the diameter of liquid nozzle outlet, **v** represent the velocity at nozzle outlet, **μ** is viscosity, **ρ** is density, characteristic length L (i.e., droplet diameter) and **σ** is surface tension [218].

2.5 Fluids under external forces

In microscale flows, even a small change in the local flow conditions can result in a structural or orientation change of self-assembled or colloidal particles [219]. Fluids are classified depending on the relationship between the shear properties such as shear stress and shear rate. These changes explain the influence of the microscopic properties and the local shear effects on the liquids or fluids. Due to the small length scales, the microfluidic channel, enhance the nonlinear response of complex fluid-flows. Based on these characteristics, there are several applications, from micro-rheometry techniques to the investigation of purely elastic instabilities [220, 221]. Additionally, these shear flows can be useful for viscoelastic fluids. Microfluidic flat liquid jet technology is an excellent platform to study this intrinsic ability to enhance the shear flow of the viscoelastic fluids at low Reynolds numbers. Due to the hydrodynamics of gas focusing, the small channels of microfluidic devices are an ideal platform to perform rheological characterization beyond the limits of the commercial rheometers [222]. Microfluidic flat liquid jets allow investigating complex liquids which are, spatially confined under shear flow conditions in small dimensions. In particular, fluid samples, that are sensitive to shear, can be affected by the jet. Therefore, the understanding of the flow properties of a microfluidic liquid jet and their influence on the liquid sample is of importance [223].

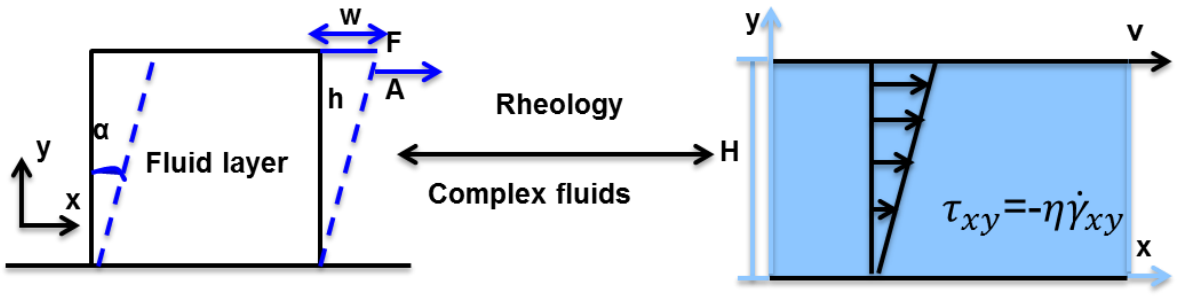

Fig.14: Illustration of a fluid deformation and flow of complex fluids to connect rheology of two ideal behaviors.

Non-Newtonian fluids do not follow Newton's law of viscosity. For Newtonian fluids, the shear stress $\boldsymbol{\tau}$ is linearly proportional to the shear-strain-rate $\dot{\boldsymbol{\gamma}}$. The constant proportionality known as shear or coefficient of viscosity $\boldsymbol{\eta}$ describing Newton's law of viscosity's defined by:

$$\tau = -\eta\dot{\gamma} \tag{9}$$

The shear flow is the movement of fluid layers such that they slide over each other when a force **F** acts on a specific cross-sectional area of the fluid (Fig.14). The shear force **F** always works in the parallel direction to the surface plane [224]. The shear stress is defined as the shear force acting per unit area and known by $\boldsymbol{\tau}$:

$$\tau = \frac{F}{A} \tag{10}$$

The influence of the particle orientation to the viscosity in a shear flow was first studied by Brenner in 1974 [225]. If an anisotropic particle is aligned with its major axis parallel to the flow direction the flow resistance of the particle is minimized thus leading to particle orientation (shear thinning) [226]. If the major axis of the particle is aligned perpendicularly to the flow direction, the maximized flow resistance of the particle is known as shear thickening [227]. At small concentrations, the particle-fluid interaction is pronounced and a microfluidic device plays a significant role in the rheological response, while at high concentration, the interparticle interactions dominate the colloidal dispersion in the fluid [228].

Small particles tend to move with the same local fluid velocity as that of the fluid when the particles are very small in the colloidal solution (drag force). For large aspect ratio particles, this depends on the density of the fluid and preferred aligned directions. This behavior clearly shows for small rods, presenting different aspect ratios was studied in shear flow, they concluded that the aspect ratio of this elongated particles plays the leading role in shear flow [229, 230]. Several groups have studied orientation dynamics in flows where the effects of aspect ratio and inertia have been investigated. The orientation distributions and the rotational diffusion have been measured in complex flows, which lead to study rheological properties [231-234].

Microfluidic liquid jet systems are a promising sample environment for rheology studies on complex fluids under extreme shear flow [159, 235]. Microfluidic liquid jets also offer the

possibility to study molecular and atomic liquids such as water or liquid metals via X-ray scattering [236]. In all these applications, the microfluidic liquid jets carry dispersed particles whose spatial and orientational distributions within the jet critically influence the properties of the fabricated structures. Due to its importance, a few research groups are working on the orientational distribution of particles within the flow (cylindrical) and droplets. However, there is hardly any knowledge about the orientational distribution of particles within the free liquid sheet because this requires to develop a challenging methodology that so far has not been available. In the framework of this thesis, the orientational behavior of spindle hematite particles under shear flows has been studied as a function of particle volume fraction and aspect ratio of nanoparticles in microfluidic flat liquid sheet.

3. Microfocus SAXS/WAXS theory

The interaction of X-rays with matter offers possibilities to study its structure down to the atomic scale. Since the early 20th century, scientists have been using X-ray scattering techniques to probe the structure of matter. Recently, advanced X-ray methods have been developed to study different properties of matter. Among these techniques, small-angle X-ray scattering (SAXS) and wide-angle X-ray scattering (WAXS) are suitable methods to investigate soft matter systems, in particular, colloidal dispersions. This chapter will give an overview of the theoretical background of SAXS and WAXS, the instrumentation and the analysis relevant for this thesis. The necessary concepts and relevant equations to understand the structure of the samples in this study are adapted from [237-240].

3.1 Elastic scattering

The scattering of electromagnetic waves is a useful tool for the characterization of colloids and polymers (241). A schematic illustration of the basic setup of X-ray scattering is shown in Fig. 15.

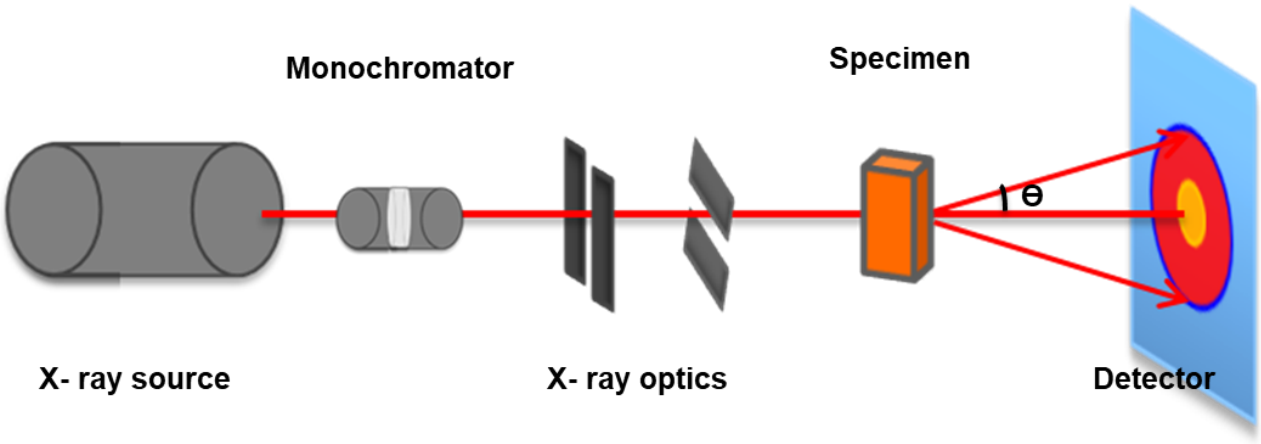

Fig.15: Schematic setup of an X-ray scattering experiment. The collimation system adjusts the beam size on the sample. The detector records the characteristic scattering patterns of the sample, where ɵ is scattering angle (Image adapted from [243]).

Emitted X-rays (e.g., synchrotron source, rotating anode) pass through monochromators X-ray optics and collimation systems before they hit the sample. The scattering process of interest for

SAXS/WAXS is an elastic one because the scattered photons have the same energy as the incoming photons. If the scattered X-rays are coherent, a phase difference between the secondary waves appears originating from different spatial positions of the scattering electrons. 2D digital detectors record resulting scattering patterns from the constructive or destructive interference. These patterns are characteristic of the given sample structure in case of samples in a regular lattice and are fundamentally described by Bragg's law (see equation 11) for principles of wave interference.

$$2d\sin\theta = n\lambda \tag{11}$$

where d is the lattice distance between the scattering electrons, θ is the half scattering angle, n is a positive integer and λ is the wavelength of the used X-rays. The Bragg equation is schematically illustrated in Fig.16 (A), showing the path difference between incoming and reflected X-rays on two scattering planes [242, 243].

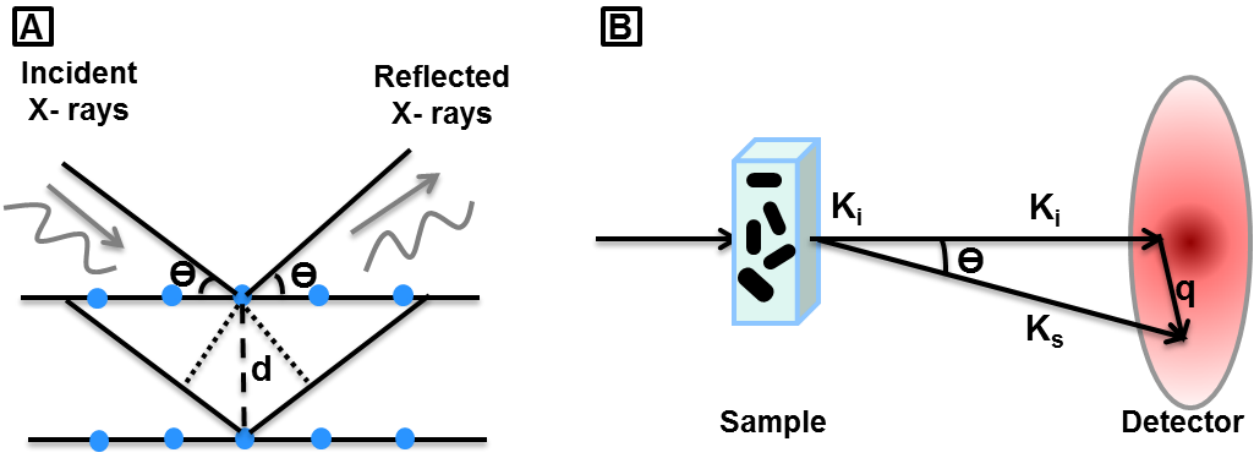

Fig.16: (A) Schematic illustration of the Bragg equation with incident and reflected X-rays on two scattering planes, showing the lattice distance d, the half scattering angle **θ**, the wavelength λ and the path difference defined by Bragg's law. (B) Schematic representation of scattering geometry. The sample scatters the incident X-ray radiation with the wave vector $\mathbf{k_i}$ into different directions with scattered wave vectors $\mathbf{k_s}$. Scattered radiation observed at the angle θ from the incident wave can be described by the wave vector transfer **q** (Image adapted from [243]).

For a better understanding of the scattering processes, a typical geometry for a scattering technique is shown in Fig.16 (B). A sample scatters an X-ray wave with an initial wave vector $\mathbf{k_i}$ and wavelength λ_i. After the scattering process, the scattered X-ray wave changes its propagation direction by an angle θ and propagates with wave vector $\mathbf{k_s}$ and wavelength λ_s.

$\mathbf{k_i}$ is the wave vector and its amplitude is inversely proportional to the wavelength λ of the incoming wave

$$|\mathbf{k_i}| = \mathbf{k} = \frac{2\pi}{\lambda} \tag{12}$$

Consider a scattered wave propagating in the direction characterized by the scattering wave vector $\mathbf{k}_s$. The wave vector transfer **q** is then introduced as

$$\mathbf{q} = \mathbf{k_s} - \mathbf{k_i} \tag{13}$$

In the case of elastic scattering, the moduli of scattered and incident wave vectors are equal

$$|\mathbf{k_i}| = |\mathbf{k_s}| \tag{14}$$

From eq.(11)-(13) the magnitude of the scattering vector q can be derived as

$$\mathbf{q} = \frac{4\pi}{\lambda}\sin\left(\frac{\theta}{2}\right) \tag{15}$$

where the scattering angle θ is the angle between wave vectors $\mathbf{k}_i$ and $\mathbf{k}_s$.

To describe the interference of the waves, the scattering amplitude E**(q)** dependence on the density and position of the scattering centers ρ**(r)** in the sample is introduced and described by,

$$\mathrm{E}(\mathbf{q}) = \text{const.} \int \rho(\mathbf{r}).\, \mathrm{e}^{-\mathbf{ikr}}\mathbf{dr} \tag{16}$$

The mathematical form of equation 16 is a Fourier transformation; therefore, the scattering density function ρ**(r)** and the scattering amplitude E**(q)** are a pair of Fourier transforms and link the real space to the reciprocal space. However, E**(q)** is experimentally not accessible, as only the scattering intensity I**(q)** can be measured. Hence, their relationship is defined with I**(q)** as the time-averaged square of the absolute value of the scattering amplitude E**(q)** as

$$\mathrm{I}(\mathbf{q}) = \langle |\mathrm{E}(\mathbf{q})|^2 \rangle \tag{17}$$

In the form of a Fourier transform, I**(q)** can also be expressed as,

$$\mathrm{I}(\mathbf{q}) = \langle \int \gamma(\mathbf{r}) \mathrm{e}^{-\mathbf{iqr}} \mathbf{dr} \rangle = 4\pi \int_0^\infty \gamma(\mathbf{r}) \mathbf{r}^2 \frac{\sin(\mathbf{qr})}{\mathbf{qr}} \mathbf{dr} = 4\pi \int_0^\infty \mathrm{p}(\mathbf{r}) \frac{\sin(\mathbf{qr})}{\mathbf{qr}} \mathbf{dr} \tag{18}$$

with γ**(r)** as the autocorrelation function of a statistically isotropic system without any long-range order, given by

$$\gamma(\mathbf{r}) = \langle \int \rho(\mathbf{r_e}) \rho(\mathbf{r_e} - \mathbf{r}) \mathbf{dr_e} \rangle \tag{19}$$

With $\mathbf{r_e}$ as the wave vector of the first scattering electron and the pair distribution function **p(r)** given by

$$\mathrm{p}(\mathbf{r}) = \mathbf{r^2}.\gamma(\mathbf{r}) \tag{20}$$

Whereas p**(r)** results from the self-convolution of the scattering center density ρ**(r)**. [244] To clarify the relations between real and reciprocal space, a graphical illustration of the mathematical operation is shown in Fig.17.

In this Fourier-transformation, both directions, while the square of the absolute value is fully reversible, but the self-convolution are not. Moreover, this leads to the phase problem due to the required scattering center density ρ**(r)**, which is not extractable from the experimentally measured scattering intensity because the phase information is missing [245]. Therefore, two different approaches have been developed to receive the scattering center density ρ**(r)**. The so-called

indirect method is based on the modeling of the scattering center density ρ**(r)** using spline functions. The splines are transformed into the measurement space and fitted to the scattering curve. The desired scattering center density ρ**(r)** is finally received by the deconvolution of these fitted spline functions [246].

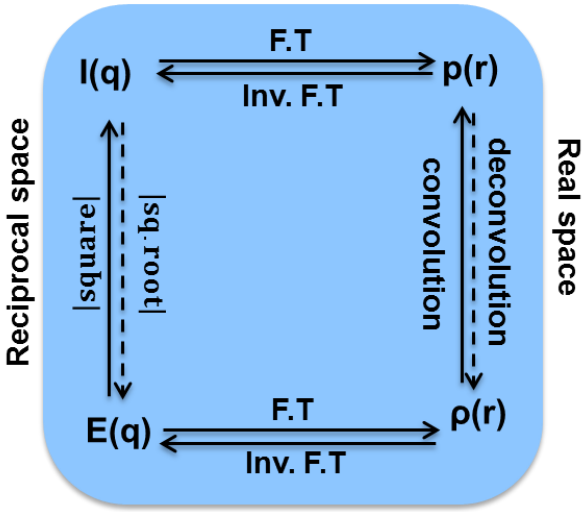

Figure 17: Graphical illustration of the relationship between the mathematical operations linking the reciprocal space and the real space for small-angle X-ray scattering. The pairs of Fourier transforms scattering intensity I**(q)** and pair correlation function p**(r)**, as well as the scattering amplitude E**(q)** and scattering density function ρ**(r)**, are shown (Image adapted from [248]).

One approach for obtaining the scattering center density ρ**(r)** is the so-called indirect method. And this is based on modeling ρ**(r)** using spline functions, which are Fourier transformed into the measurement space and fitted to the scattering curve, leading to the scattering center density by final deconvolution [247-250]. Another approach is the direct method, which uses structure with a known scattering center density ρ**(r)** that is Fourier-transformation to receive scattering amplitude E**(q)**.

3.2 Form factor

Another approach is the model-based or direct method, which uses a given structure where the scattering center density function ρ**(r)** is known, to describe the scattering curve as a basic function by

$$I(q) = I_0 . P(q) \tag{21}$$

with $\mathbf{I_0}$ as the intensity of the incident beam at an angle of 0° and the form factor P(q) [251]. Just as the name states, the form factor describes the particle's form and shape. One of these simpler equations is the form factor of spherical particles with the radius **R** and homogenous shapes that have a constant scattering length distribution. These can be described by an analytical expression that is given by [252]

$$P(q) = \rho^2 V^2 \left(3 \frac{\sin(qR) - qR.\cos(qR)}{(qR)^3}\right)^2 \tag{22}$$

For example simple anisotropic particles, cylinders can be described by the following formula which uses the parameter **R** to describe the cylinder radius and the parameter for the cylinder length **L**

$$P(q) = \frac{L\pi}{q} . P_c(q) \tag{23}$$

with

$$P_c(q) = 4\rho^2 \mathbf{R}^2 \left(\frac{\sin(q\mathbf{R})}{q\mathbf{R}}\right)^2 \tag{24}$$

This formula is valid for rigid cylinders [253], but it has to be altered to describe the spindle-shaped particles which have been investigated in this thesis.

A form factor from a spindle shape particle describes a body of revolution resulting from two intersecting circles with radius ***R*** (Fig.18). The geometry is influenced by a minor semi-axis *R1* and a major semi-axis ***L***, which are parallel to the *x* and *z*-axis of the particle, respectively.

Since $\boldsymbol{L} > \boldsymbol{R_1}$ the resulting form factor is anisotropic and the form factor can be expressed for a single spindle-shaped particles by

$$P_{single}(q,\theta_q,\mathbf{R}_1,\mathbf{R}_2,\nu) = \left(\frac{4\pi}{V(\mathbf{R}_1,\nu}\int_0^{L/2}\cos(qz\cos(\theta_q))\frac{\mathbf{R}_1-\mathbf{R}_2+(\mathbf{R}_2^2-Z^2)^{\frac{1}{2}}}{qsin\,(\theta_q)}.J_1\left\{qsin(\theta_q)\left[\mathbf{R}_1-\mathbf{R}_2+(\mathbf{R}_2^2-Z^2)^{\frac{1}{2}}\right]\right\}dz\right)^2 \quad (25)$$

where V($\mathbf{R}_1$,ν) is the particle volume, J_1 is the Bessel function of the first kind, dz is a differential increment of $\boldsymbol{L}$ and the radius $\boldsymbol{R_2}$ is given by $\boldsymbol{R_2} = {(\boldsymbol{L^2}+\boldsymbol{R_1^2})}/{\boldsymbol{4R_1}}$ The particle volume is given by

$$V(\mathbf{R}_1,\nu) = \frac{2\pi}{3}\left\{\frac{(2\mathbf{R}_1)^3}{8}\nu\left[\frac{3}{4}(1+\nu^2)^2-\nu^2\right]\right\}$$
$$+\frac{2\pi}{3}\left\{\frac{3(2\mathbf{R}_1)^3}{32}(1+\nu^2)^2\left[1-\frac{1}{2}(1+\nu^2)\right]\arcsin(\frac{2\nu}{1+\nu^2})\right\} \quad (26)$$

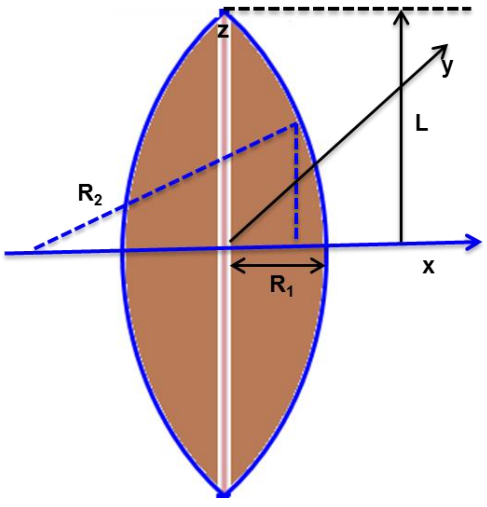

Fig. 18: Sketch of the geometry of a spindle-shaped particle (Image adapted from Joana Valério. Dissertation: "Structure of complex fluids under shear flows", University of Hamburg/DESY 2018).

The real particle system underlies a natural distribution of particle sizes, quantified by the size polydispersity. To consider the polydispersity, a Schulz-Flory distribution can be utilized to modulate the size of the minor semi-axis [254]. Thus, the form factor of a polydisperse spindle-shaped particles system can be derived using:

$$P_{poly}(q, \theta_q, \mathbf{R}_1, \mathbf{R}_2, Z, \nu) = \frac{1}{\langle V^2 \rangle} \int_0^{\infty} c(\mathbf{R}, \mathbf{R}_1, Z) V^2(\mathbf{R}, \nu). P_{single}(q, \theta_q, \mathbf{R}, \mathbf{R}_2, \nu) \mathbf{dR} \quad (27)$$

where c**(R, $\mathbf{R_1}$,** Z**)** represents the particles size distribution with particle radius **R** particle semi-minor axis $\mathbf{R_1}$ and ***Z*** is related to the polydispersity by:

$$p = \frac{\Delta \mathbf{R}}{\mathbf{R}_0} = \sqrt{\frac{1}{Z+1}} \quad (28)$$

here $\mathbf{R}_0$ is mean particle radius.

3.3 Structure factor

The structure factor describes the relationship and interaction between particles when the solution is more concentrated. The structure factor **S(q)** which appears as an additional factor while calculating scattering intensity formula

$$I(q) = I_0 . p(q) . S(q) \quad (29)$$

Whereas the structure factor **S(q)** is specified as

$$\mathbf{S}(q) = 1 + \int_0^{\infty} [g(r) - 1] \frac{\sin(qr)}{(qr)} 4\pi^2 dr \quad (30)$$

where g(r) is the radial distribution function, for systems with increasing concentration, it takes higher-order and, the structure factor **S**(q) generates peaks that decay exponentially. For increasing concentrations and more ordered systems, the structure factor creates peaks with exponential decay due to the repulsive interaction potentials. The change in the peak intensity increases the concentration and the order of the system. Dilute systems, on the other hand, are

defined solely by the form factor, as the structure factor becomes 1 [255]. The orientation of anisotropic particles along a particular direction, however, was not yet considered in the above discussion. However, those within a stream or a sheet-like liquid jet, such anisotropic particles, were shown in the results and discussion chapter.

3.4 Small and wide-angle scattering

Based on the magnitude of the scattering angle, the elastic X-ray scattering is divided into two regimes which are small and wide-angle X-rays regimes, SAXS and WAXS, respectively. These techniques with the modern X-rays sources have become a promising methodology for analysis of structural dynamics in solutions. As discussed in the above section, small beam sizes directly influence observable volume and hence, the temporal resolution of the microfluidic-SAXS/WAXS-experiment. The high brilliance of the third-generation synchrotrons enables short exposure times. Although the base equations for the scattering intensity calculations are equivalents for atoms, molecules and nano-particles, the measured scattering for these systems differs in the characteristic structural sample size d or wave vector, q. The domain of the X-ray scattering intensity holds a law of reciprocity between the scattering vector $|\mathbf{q}|$ and the characteristic length, L, of the scale within objects are being studied, such that $L \sim 1/q$ [256].

SAXS is employed when the system contains larger correlation distances from nano to micrometer regimes. Through this technique, the structure of the particles can be probed by measuring the scattering intensity at lower angles, such as those below few degrees. WAXS is utilized for short correlation distances regions, therefore, is a useful technique for solving the orientation of the particles, whereas, in SAXS, the scattering originates from larger-scale inhomogeneities in the electron density. Commonly, the WAXS region deals with scattering angles exceeding 10^{o} at the atomistic scales [256, 257].

In the framework of this work, WAXS experiments were performed at ID13 (ESRF, Grenoble). The WAXS technique was used to reveal the orientation of spindle-shaped particles along shear flows through the analysis of the azimuthal angle calculations (see section 5.4).

4. Experimental section

4.1 Materials

3-inch silicon wafers were purchased from Si-Mat Silicon Materials. SU-8 2050 photoresist and mr-Dev600 developer were purchased from Microchem Co. The PDMS Sylgard 184 kit from Dow Corning Co and 0.38 mm inner / 1.09 mm outer diameter PE tubing was purchased from Scientific Commodities. The polymer THV 221 GZ was obtained from Dyneon GmbH (Germany) as granulates. Acetone was bought from Carl Roth GmbH + Co. KG and was used without any further purification. IPA was bought from Carl Roth GmbH + Co. KG and was used without any further purification. Hematite spindles were obtained from Joana Valeria from Prof. Grubel Group at DESY, Hamburg. Carbon Nanotubes (CNTs) were obtained from Prof. Alexander Haas (Polymer Composites) at Hamburg University of Technology.

4.2 Instruments

Photolithographic emulsion film masks were designed using AutoCAD (Autodesk). The mask aligner MJB4 by Suss MicroTec AG was used for master production. All UV lithography steps were carried out in a cleanroom (CFEL, Prof. Henry Chapman). Soft lithographic fabrication was carried out in a laminar flow box. Plasma activation was carried out using an Atto vacuum plasma cleaner with 13,56 MHz by Diener Electronic. High-speed video microscopy was performed with a Phantom v711 camera (Vision Research Europe). The jetting experiments were carried out with gas-tight 1700 Series Syringes by Hamilton on a Nemesys 290N syringe pump system by Cetoni. The experiment was observed with a Phantom v711 camera, which was connected to an IX73 light microscope from Olympus Europa SE & Co. KG. The homogenization of the polymer nanocomposite was performed using an UP400St sonotrode (Hielscher Ultrasonics GmbH). Rheology experiments were carried out with a modified Haare MAR 22 rotation rheometer with a 35 mm plate-to-plate sensor. SEM images were taken at 1000x and 5000x at 1kV with an Everhart-Thornley detector with Dual-beam focused ion beam instrument SCIOS, FEI.

4.3 Photolithographic master fabrication

The microfluidic flat liquid jet devices were fabricated using a previously described lithography workflow, (7) but was optimized to yield high aspect ratio structures for solution-phase X-ray scattering and spectroscopy in this study. The fabrication process can be divided into two parts: the UV-lithography master fabrication followed by molding and the bonding using soft lithography.

The master mold fabrication process was started by spin coating a 3" silicon wafer with a negative photoresist (SU-8 2050, Microchem Co). The optimized protocol is based on the fabrication of multi-layer SU-8 microstructures [263], but the optimized parameters for our designs are different. The key points of processing parameters are outlined below

1. Spin coat
   (a) Dispense SU 8-2050 photoresist on 3" silicon wafer surface
   (b) 1500 revolutions per minute (rpm), 30 seconds (s), acceleration of 1000 rpm s^{-1}
   (c) 500 rpm, 10s for control the edge bead
2. Soft bake
   (a) 65 ^{o}C for 5 min on the hot plate,
   (b) 95 ^{o}C for 20 min on the second hot plate,
   (c) 15 min of cool-down period (relaxation, cool at 35 % rate, 5 ^{o}C/1.5 min) until room temperature (RT)
3. Exposure
   (a) Vacuum contact between the mask and silicon wafer,
   (b) 360 nm wavelength UV
   (c) Exposed 3 times 4.5 sec
4. Post bake
   (a) Ramp (heat at 35 % rate, 5 ^{o}C/1.5 min) to 65 ^{o}C for 5 min on the hot plate,
   (b) Keep wafer at 65 ^{o}C for 3 min,
   (c) Ramp (heat at 35 % rate, 5 ^{o}C/1.5 min) 95 ^{o}C for 3 min,
   (d) Keep wafer at 95 ^{o}C for 10 min,
   (e) 15 min of cool-down period (relaxation, cool at 35 % rate, 5 ^{o}C/1.5 min) until room temperature (RT)

Once these optimized process parameters are finished, steps are repeated as three times as layers are desired for a 3D focusing device, as shown in Table 2.

Table.2: Fabrication protocol for three-layer SU-8 layers using a single developing step.

Layer	**SU-8 resist**	**Spin coat**	**Soft bake**	**Exposure**	**Post bake**
1	SU-8 2050	1500 rpm for 30s 500 rpm for 10s	65 ^{o}C for 5 min 95 ^{o}C for 20 min 15 mins relaxation at RT	3 times 4.5 sec	65 ^{o}C for 3 min 95 ^{o}C for 10 min 15 mins relaxation at RT
2	SU-8 2050	3000 rpm for 30s 500 rpm for 10s	65 ^{o}C for 5 min 95 ^{o}C for 9 min 15 mins relaxation	2 times 7.0 sec	65 ^{o}C for 5 min 95 ^{o}C for 8 min 15 mins relaxation at RT
3	SU-8 2050	3000 rpm for 30s 500 rpm for 10s	65 ^{o}C for 5 min 95 ^{o}C for 10 min 15 mins relaxation	2 times 47.0 sec	65 ^{o}C for 5 min 95 ^{o}C for 9 min 15 mins relaxation at RT

The exposed wafer was developed in mr-Dev600 (micro resist technologies) for 45 min, followed by washing with isopropanol and dried with compressed air.

Photolithographic emulsion film mask designs were exposed under vacuum contact mode using an MJB4 mask aligner. The process of final mold involves sequential three layers. The schematic representation of the master fabrication is shown in Fig. 19.

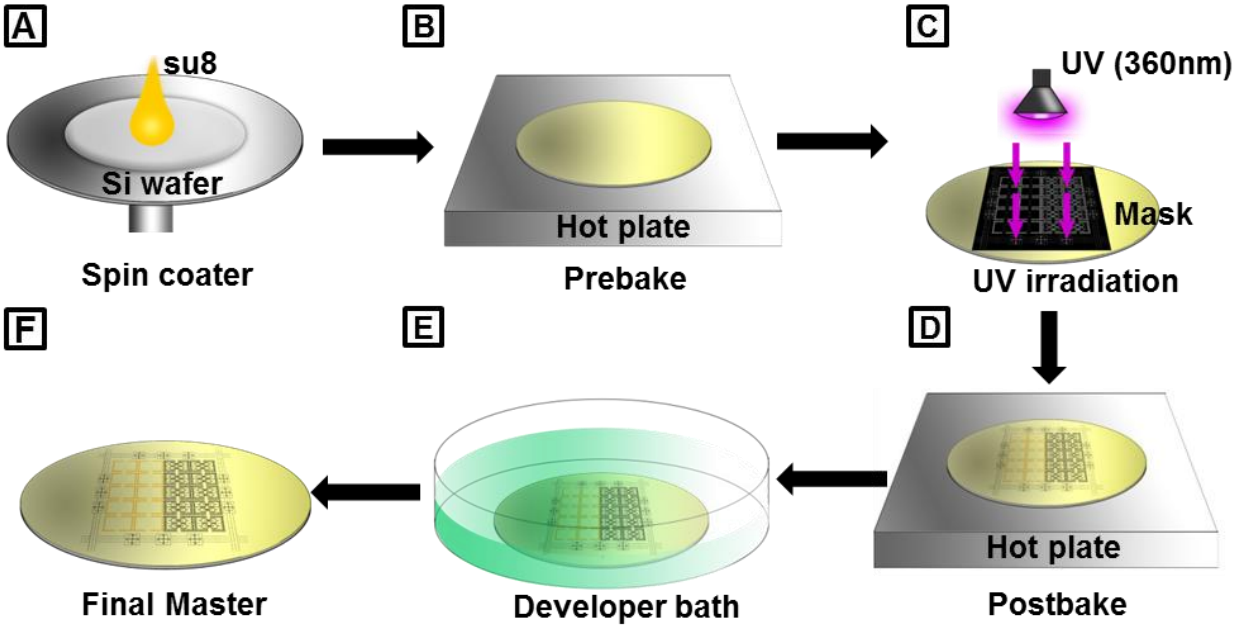

Fig. 19: Schematic representation of the microfluidic liquid jet master fabrication steps using standard photolithography technique involves repeating steps to fabricate multilayered master: spin-coating a layer of the desired photoresist on a silicon wafer (A) prebake until the solvent is evaporated (B) UV-exposure (C) post bake to crosslink the exposed structures (D) then follow the steps three times to fabricate 3D focused device (E) develop the final structure to remove exposed polymer and (F) final master.

4.4 Microfluidic device fabrication

The PDMS (Sylgard 184 kit, Dow Corning CO) was mixed with curing agent at a 10:1 ratio, poured onto the SU-8 master placed on an aluminum foil-covered Petri-dish. The mixture was degassed in a desiccator to remove all air bubbles and was baked at 75 ^{o}C for 2 hours. The cured PDMS structure was peeled from the master and inlet ports, which were punched using a 0.75 mm biopsy puncher. The PDMS devices were separated and the nozzle outlets and was precisely cut under a microscope. The two device halves were cleaned using isopropanol and compressed air, as shown in Fig 20.

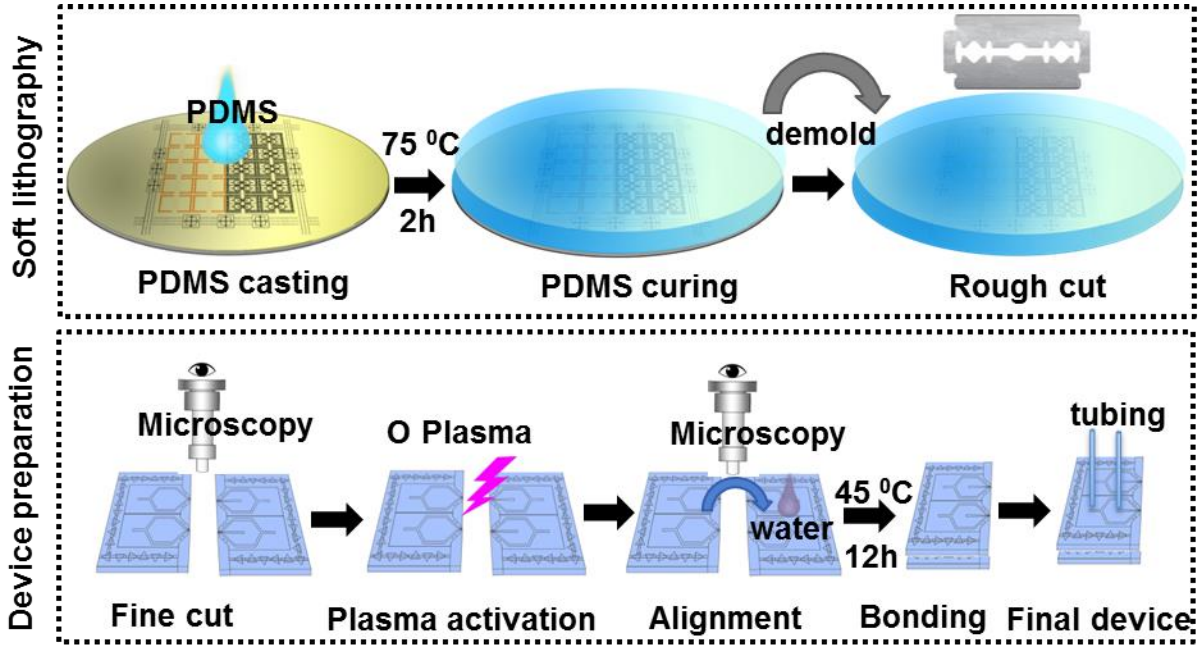

Fig. 20: Microfluidic nozzle devices for stable flat sheets are fabricated by using soft-lithography techniques. Structured master was used as a template for polydimethylsiloxane (PDMS); after curing, the device was prepared for bonding the two precisely tailored PDMS halves under oxygen plasma. Water was used as a lubrication agent to facilitate the precise alignment.

The two micro-structured halves have to be aligned and bonded together to achieve a 3D flow-focusing device. Hydroxyl surface activation of the PDMS can be performed by oxygen plasma [258]. Hydroxyl groups can substitute the methyl groups of the PDMS surface while plasma activation as seen in Fig.21. When hydroxyl groups come into contact with each other, a covalent silanol bond is formed with the expulsion of water. The PDMS surfaces were plasma-activated using oxygen at 0.38 mbar for 100s. The activated device halves were aligned under the microscope and bound in an oven overnight at 45 ^{o}C as shown.

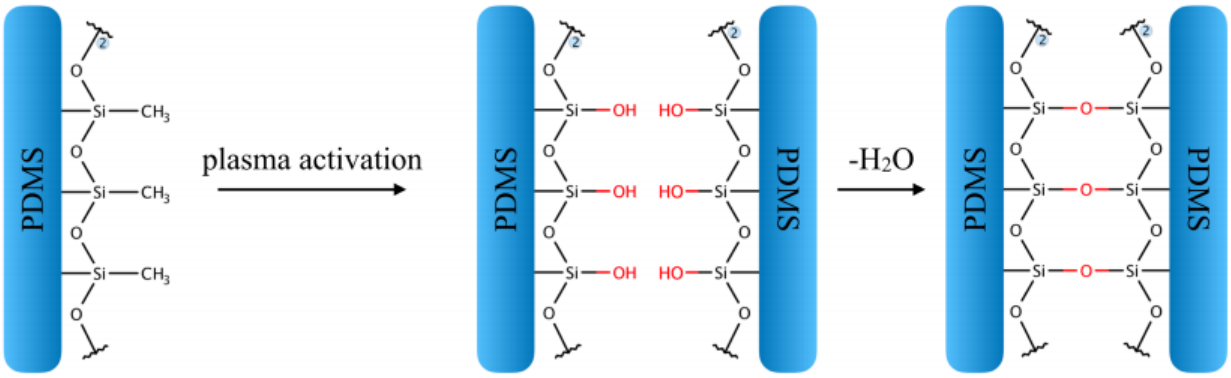

Fig.21: Schematic mechanism of the PDMS-PDMS bonding due to oxygen plasma activation. The plasma activates the PDMS surface by substituting the methyl group with the hydroxyl group. By placing two plasma-activated PDMS pieces onto each other, the hydroxyl groups can react and form a covalent bond by condensation reaction removing the generated water [adapted from 259].

4.5 Preparation of hematite nanoparticles

A spindle-shaped hematite nanoparticle with an aspect ratio of ten was chosen to be investigated to perform WAXS experiment at ID13 (ESRF, France). Hematite is an attractive material due to the secure synthesis method, varying physical properties by modification of nanoparticle shape and sizes. In the framework of this project, spindle-shaped hematite monodisperse, single-crystalline particles with tunable aspect ratios were prepared by forced hydrolysis [260]. This anisotropic sample system can be used to characterize flow effects due to the sample is sensitive to shear forces via aligning to a preferred direction [261, 167]. These hematite spindles are of great interest for researchers because it is possible to vary their physical properties by the modification of particle shape and size.

4.6 Sample recycling system

For a microfluidic flat liquid jet system based on the GDVN environment under atmospheric pressure conditions, an efficient recycling system was built, as shown in Fig. 22 due to little higher flowrates (60 mL/h). The lab-scale experimental setup comprises of various parts, such as

the high-speed camera, microscopes for *in-situ* observation and diagnostics of the liquid jet, as well as a nozzle holder with multiple diagnostics tools, optical light source and reservoirs.

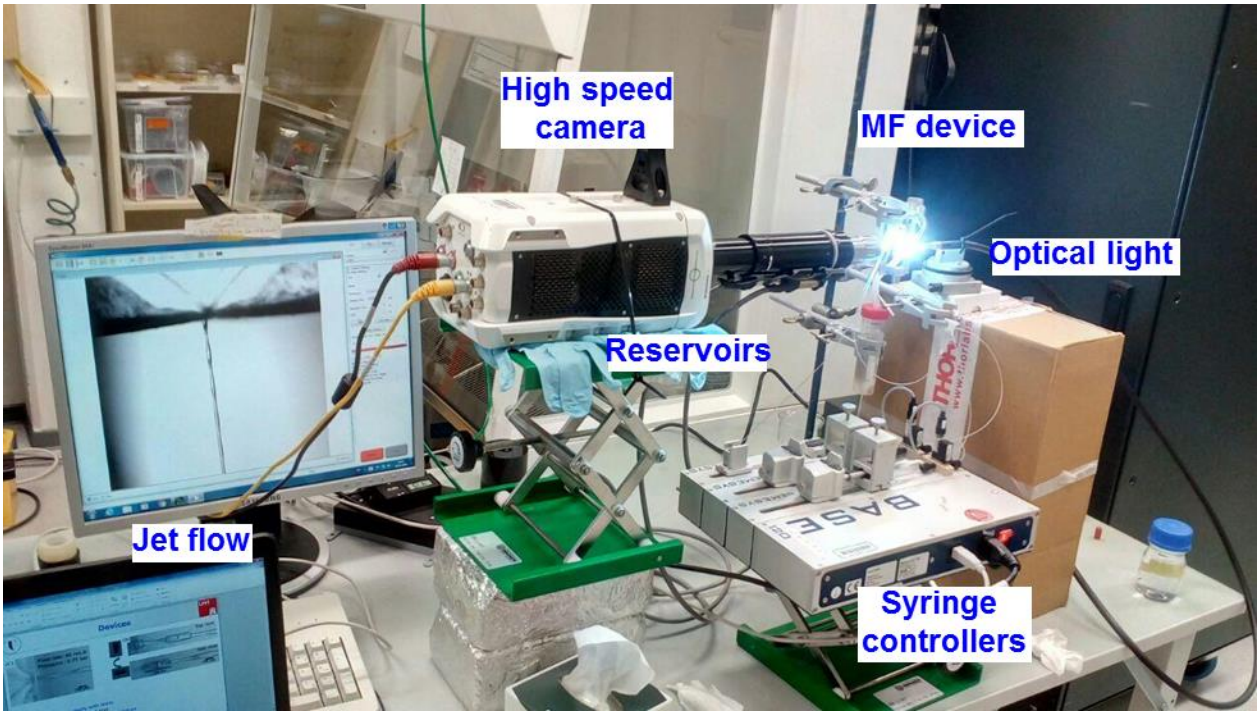

Fig.22: Overview of the lab-scale experimental setup.

Despite being the fact that the flat liquid jet setup to be a proven valuable for X-rays measurements, pre-experiments were performed in the lab to maximize the stability of jet and hence operating procedure of some parts of the setup, such as reservoirs, sample delivery systems and the jet characterization mechanisms were generated. This section describes the several improvements implemented to the microfluidic flat liquid jet setup to perform the actual experiment at beamline to save time and minimize the errors, such as:

High-speed camera: A high-speed camera was implemented to reach higher frames rate and high magnification to track the sheet, jet and droplets formation in slow motion to measure the velocity of the jet and droplets. It was a megapixel camera capable of taking 1.5 million frames per second (fps) allowing for exposures times down to 300 ms.

At 512 × 48 (with a field of view of 1026 µm by 96 µm), the high-speed camera, enables precise study of the jet instabilities and droplet formation in the long axis with low exposure time 0.29 µs at a frame rate of 187327 fps. To be able to follow the droplet formation in a continuous mode and being able to monitor the shape alterations during the break-up regime in a μm range scale is of utmost importance since the break-up region is always an undefined zone of characterization as shown in Fig.23.

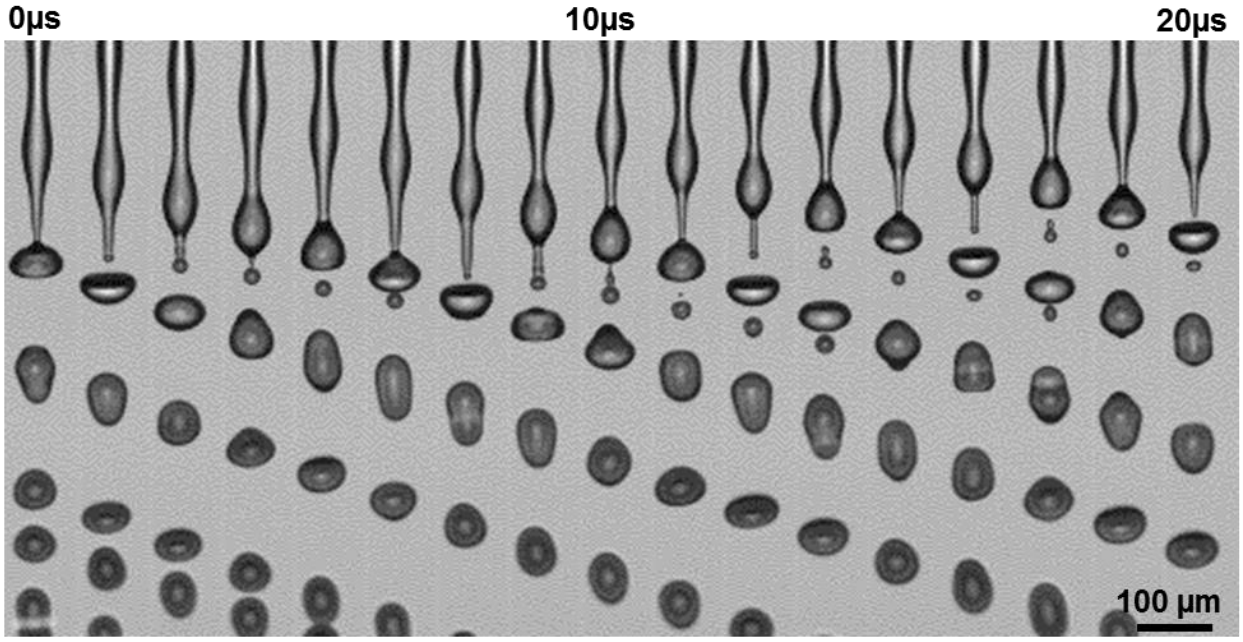

Fig.23: The experimentally obtained Droplet breakup mechanism using a high-speed camera for a microfluidic liquid jet flowing water with a liquid capillary inner diameter of 40 x 15 µm (hxw).

Jet device holders: New magnetic nozzle holders were created to increase the mechanical stability and decrease the time between nozzle changes at the beamline. These holders allowed faster nozzle change flexibility without losing its stability.

Microfluidic (MF) device: A new microfluidic liquid jet system was implemented to increase the stability of the gas focused liquid sheet formation without clogging and at lower flow rates.

Optical light fiber: Illumination was provided by a light source connected to an optical fiber along the camera axis to better image the flow direction and alignment of the nozzle etc.

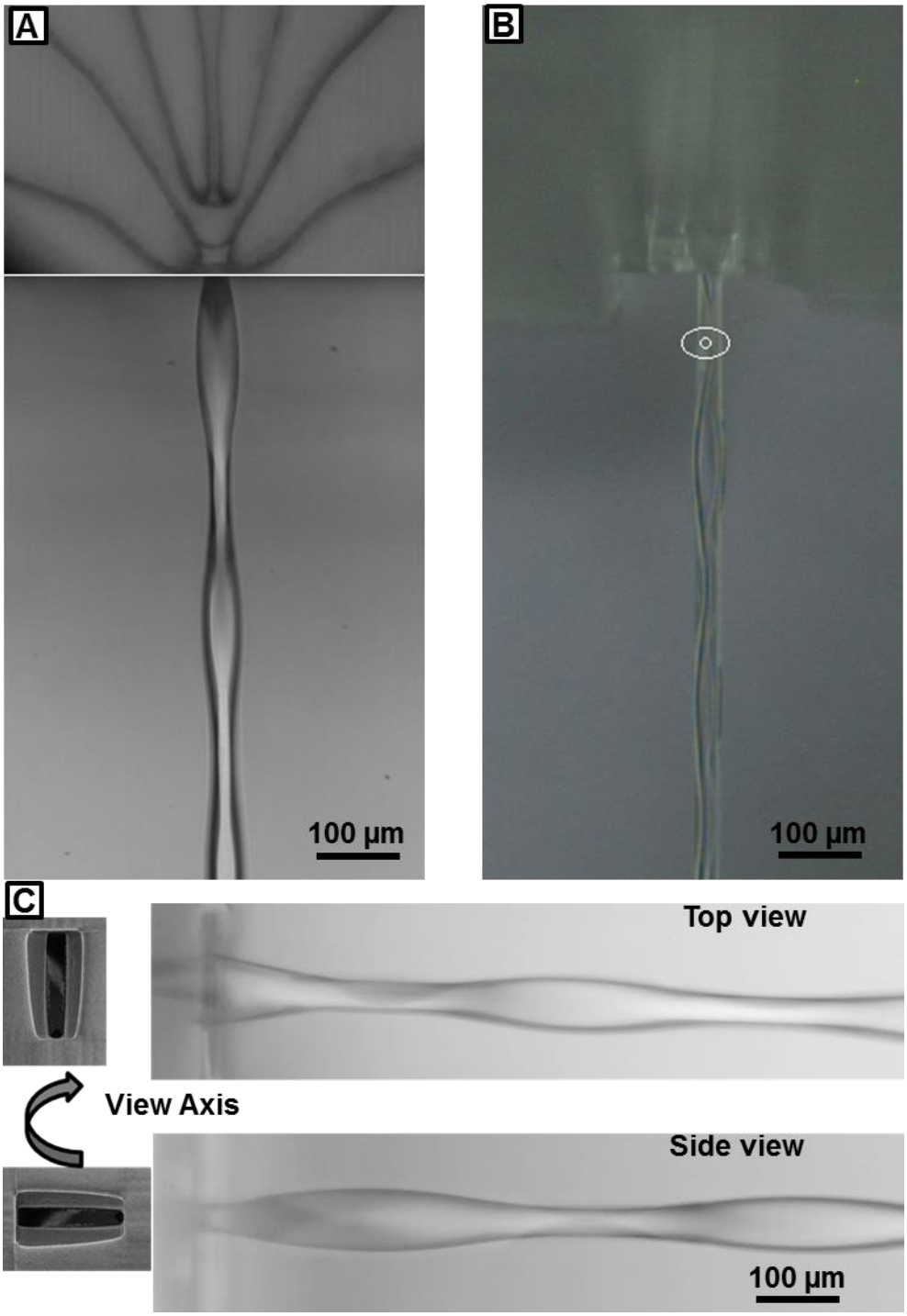

Fig. 24: (A) Optical microscopic image of one nozzle during operation using the high speed camera setup. The liquid in the central channel is focused on pressured air, which drives stable flat liquid sheets, (B) nozzle operation during beamline and (C) view of the flat liquid jets from different view angles.

Reservoirs: Due to high sample consumption, a sample recycling system was employed during the beamtime. This recycling system consisted of a tubing and funnel that caught the sample stream for reusing it using the syringe pumps.

Syringe controllers: Two neMESYS low-pressure syringe pump modules were used simultaneously in continues flow mode, i.e. one pump pushes liquid into the tubes connected to the nozzle (from syringe 1) while the other pump is drawing liquid from the collection tube below the jet (into syringe 2). Once one cycle was completed, at valve switched and the pumps reversed their pumping directions to maintain a smooth continuous flow. The syringe pump system allows for dosing liquids with high accuracy towards nano-liter range without any vibrations, thereby ensuring smooth delivery of liquids. Moreover, the control software is intuitive, making the syringe pump a user-friendly system.

These devices combined with the recycling system could be operated with normal air under atmospheric pressure conditions and using a fixed amount of sample, as shown in Fig. 24 (A and C). Fig 24 (B) shows a nozzle running during beamtime at ID13, ESRF, Grenoble, France. These nozzles are clog-free and their design prevents the confinement effects and allowing small volumes of sample for analysis.

4.7 Experimental setup at ID13 beamline

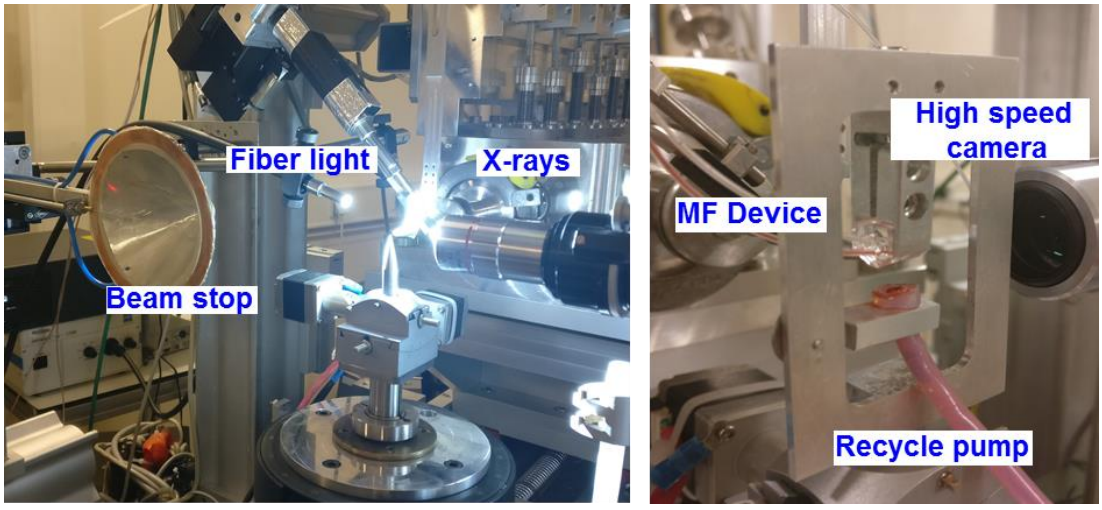

Fig.25: Experimental set-up for WAXS measurements at ID 13 at ESRF (left) and device holder with nozzle and collection tube (right).

The WAXS experiment using a microfluidic flat liquid jet was performed at beamline ID13 at ESRF (European Synchrotron Radiation Facility), Grenoble, France as shown in Fig. 25. The nozzle was mounted on a specially designed holder (right) with a collection tube below that, which was connected to an in-house developed sample recycling system. The nozzle was imaged with a high-speed camera (left) and the illumination was provided by a light source connected to an optic fiber cable (left). The experiment involved an investigation of spindle-shaped hematite nanoparticle dispersed in water using different concentrations and different particle aspect ratios. As described above, two neMESYS low-pressure syringe pump modules were used simultaneously in continues pump mode. The experiments were performed at 60 mL/h flow rate to obtain a stable liquid sheet. The measurements were done in small time intervals of 3 min with gaps of 2 min, to overcome the issues with pumping system. The sample to detector distance was 130 mm, which provided access to momentum transfer values between q min = 0.8 $A^{\circ -1}$ and q max = 3.5 $A^{\circ -1}$. A micro-focused X-ray beam of dimensions 3.0 μm × 3.0 μm (h × v) was achieved at energy of 13 keV. An overview of the liquid jet setup is presented in Fig.25.

4.8 Spindle-shaped particles inflow

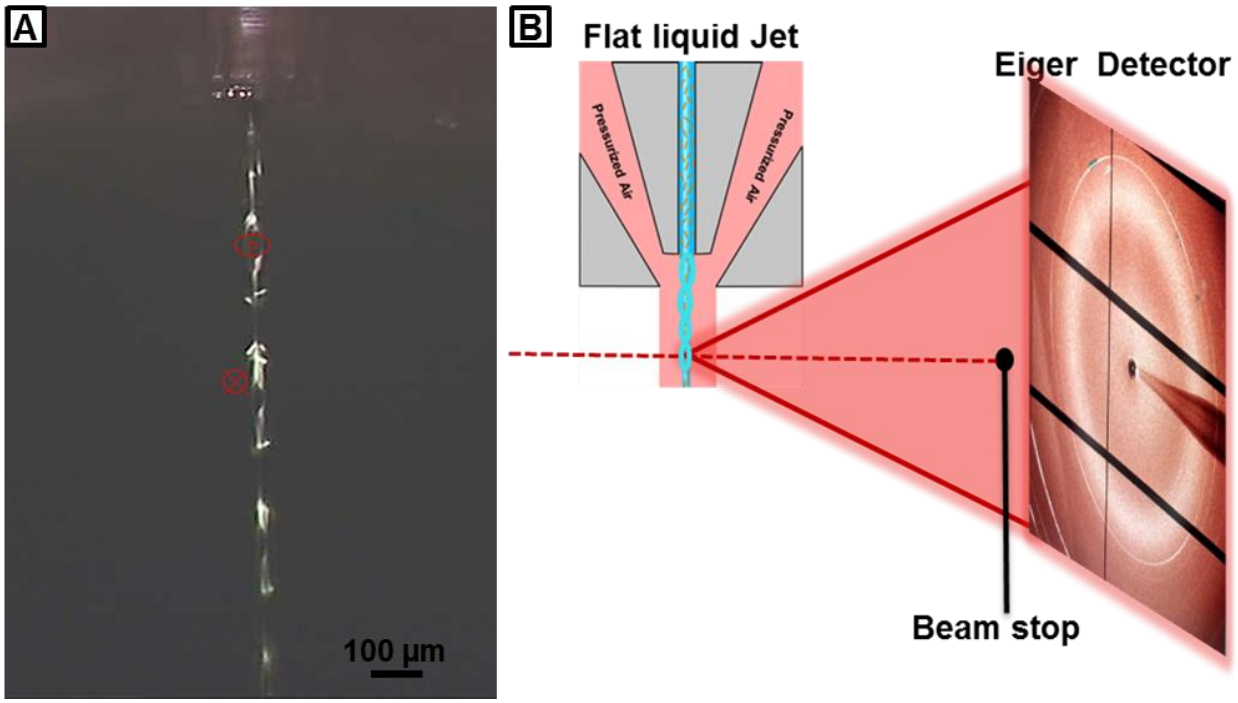

Fig.26: (A) nozzle operation during beamline imaged by in-line microscope. (B) Typical WAXS patterns taken on the liquid jet with an exposure time = 200 ms.

The alignment of anisotropic hematite particles in a flow produced by GDVN will be discussed within this section. Two different aspect ratio samples of hematite spindles dispersed in water, H1 (650:65 nm) and H2 (400:120 nm), were studied in continues liquid sheet formed by flat jet. The sheet diameter and length were controlled by the nozzle height, at constant gas pressure (43 SCCM) in the nozzle and the liquid flow rate (60 mL/h). The stable jetting condition during beamtime is shown in Fig. 26(A). Due to high sample consumption, an in-house developed sample recycling system was employed during the beamtime.

4.9 Fiber spinning procedure and characterization

The setup drawn in Fig.27 was used to fabricate the fibers and to analyze the jet in real-time. The thermoplastic fluoropolymer THV-221GZ (THV) was obtained as pellets and used without further purification. 10, 15, 20 and 25 wt% THV solutions in acetone were prepared by slowly stirring until complete dissolution at room temperature. The polymer solution was loaded into a 10 mL syringe and connected to the liquid channel and a compressed air inlet to the gas channels of the spinning device, both using 1.09 mm outer diameter (OD) PE tubing as shown in Fig. 27.

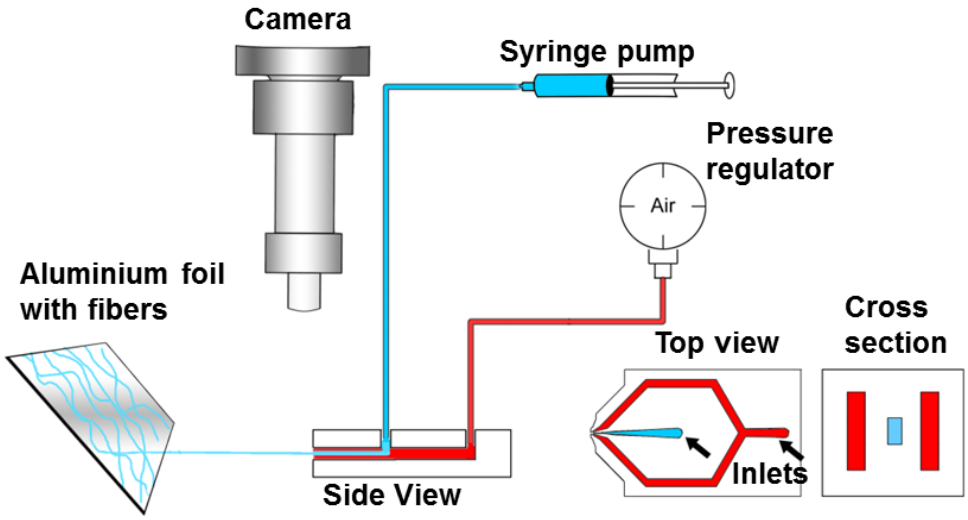

Fig. 27: Schematic view of the experimental setup for the analysis of the fibers. The microfluidic nozzle was attached to pressurized air and the polymer solution. While operating, the nozzle and the jet were observed by a high-speed camera. The fibers were collected on a substrate covered in aluminum. The bottom right corner shows the top view and the cross-section of the three-dimensional gas focusing region of the nozzle. Air channels are marked in red and solution channels are marked in blue.

To start the spinning process, airflow was initiated first and stabilized at 90-352 SCCM pressure difference followed by the polymer flow, which was controlled using high-precision neMESYS syringe pumps at a flow rate of 100-3000 µL/h. The fibers were collected on substrates covered in aluminium foil, which were placed 7 cm away from the nozzle. Optical microscopy images were taken during the fiber fabrication process using an inverted optical microscope coupled to a high-speed camera at magnifications of 4x, 10x and 20x. The fibers collected on aluminium-coated substrates were directly used for SEM analysis while avoiding any sample alterations. Table 3 showcases the parameters investigated. All combinations of these parameters were carried out.

Table 3: Variation of the parameter of the spinning process.

Polymer concentration (wt%)	**Pressure (SCCM)**	**Flowrate (µL/h)**
10	90	100
15	176	250
20	262	500
25	352	1000
		3000

For the nanocomposite fibers, a similar setup was used. However, the experiment could not be observed with a camera. Since the used nanoparticles present a risk of being hazardous for humans, the experiment was executed in a fume hood.

For both nanocomposite (hematite and CNT) solutions, a similar mixing approach was used. First 3 mL of a 30 wt% polymer solution of THV 221 GZ in acetone was set up and let to stir overnight until the polymer was completely dissolved. Right before preparing the spinning solution, the nanoparticles (hematite or CNT) were dispersed in 1 mL of acetone into a high and thin 2.5 mL flask. The dispersion was then homogenized with a sonotrode (UP 400s by hielscher). Table 4 shows the sonication parameters that were used for the different nanoparticles.

Table 4: Sonication parameters for the dispersion process of hematite nanoparticles and CNTs.

Sonication Parameters	Hematite	CNT
Time (min)	1	5
Power (%)	100	50
Cycle	1	1

Once the solution was homogenous, it was mixed in a 1:1 ratio of the 30 wt% THV 221 GZ polymer/acetone solution with the nanoparticle/acetone solution to obtain a 15 wt% polymer solution with the desired concentration of nanoparticles in relation to the polymer weighing. Fig.28 shows the workflow for the mixing process of CNTs. The same procedure was used for the Hematite nanoparticles. After 5 min of vigorous stirring, the polymer/nanoparticle solution was ready to be spun.

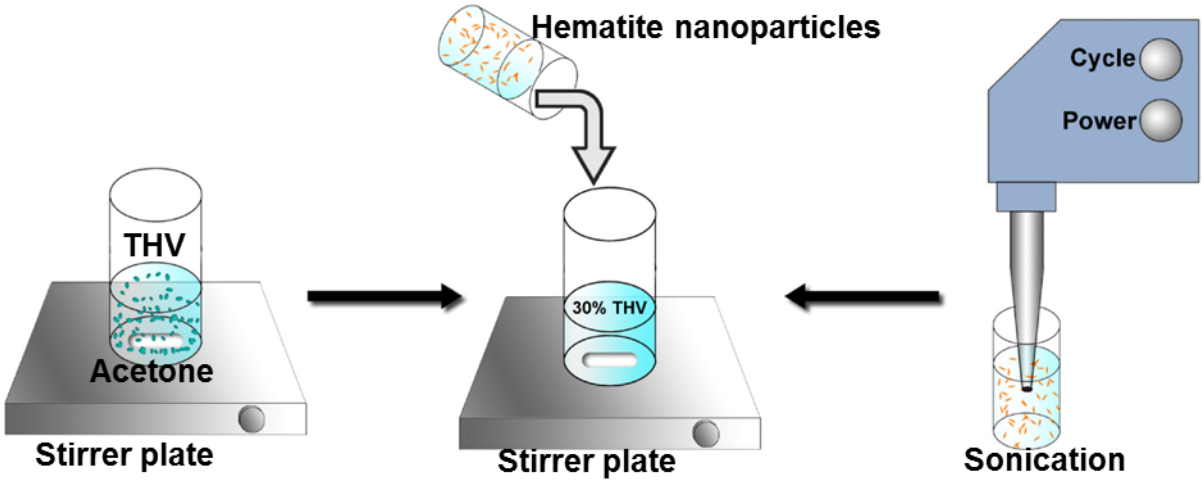

Fig.28: Schematic view of the solution prepared for the hematite nanocomposite solution. The same approach was used to process the CNT nanocomposite solution.

The fibers were collected on pieces of cardboard wrapped in aluminum foil. Rectangular pieces of the aluminum foil were cut out using a razor blade and were placed on copper tape glued to an SEM sample holder. The loaded sample holder was put under vacuum overnight. SEM images were taken at 1000x and 5000x at 1 kV.

5. Results and discussion

5.1 Nozzle design optimization parameters

High aspect ratio microstructures are the key for obtaining asymmetric liquid jet devices. Here, we built on the previously described work by Trebbin *et al.* for the fabrication of microfluidic GDVN liquid jet devices using multi-layered microchannel fabrication approach. In order to achieve high aspect ratios of such microstructures, a number of challenges had to be overcome that will be discussed below. The microfluidic flat liquid jet devices are designed using the modeling tool AutoCAD. The design parameters (Fig. 29A and 29B) are aided by exploring theoretical models predicted by [262] and followed by Trebbin et al. [7]. In brief, a different near-UV photoresist (SU-8 2050) was chosen and the photomask designs and photolithographic procedures had to be optimized. The optimizes fabrication resulted in microstructures with a 100µm : 15µm aspect ratio (height and width, respectively) suitable for the generation of flat liquid jets. Furthermore, whipping and fiber design parameters are optimized while performing experiments at the cleanroom due to optimization problems and a complete list of parameters is shown in Table 5.

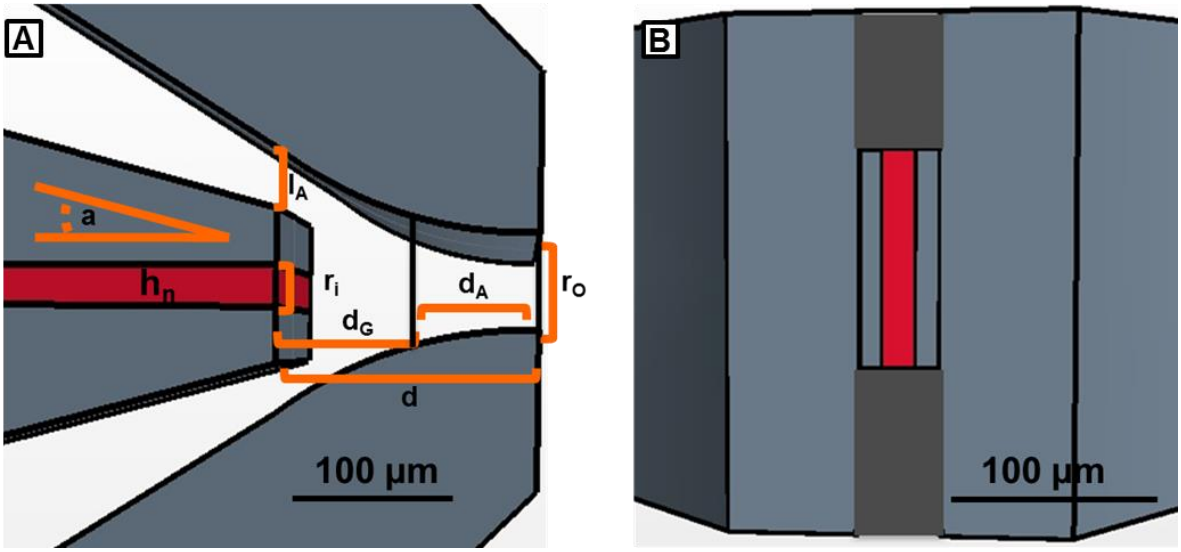

Fig.29: Nozzle design parameters. (A) Excerpt of a CAD drawing that contains features for aligning the mask during the photolithographic process and snap-in structures. (B) An illustration of the controllable nozzle outlet design.

Where, d = distance from main channel inlet to nozzle outlet, r_0 = width of the outlet, r_i = width of the main channel, d_G = distance of the gap between main channel inlet, d_A = distance of the aperture, I_A = length of the air inlet, a = angle of the air stream, c = curvature of the tapering and h_n = height of the layer.

Table 5: Design parameters and their definitions along with relevant parameter combinations.

Design parameter	Dimensions for flat jet (µm)	Dimensions for liquid jet (µm)	Dimensions for whipping jet (µm)	Dimensions for fiber jet (µm)
d	95	95	395	35
r_0	30	30	30	55
r_i	15	15	30	15
d_G	55	55	355	35
d_A	40	40	40	0
I_A	20.4	20.4	20.4	20.4
a	15^0	15^0	15^0	15^0
c	144.3	144.3	144.3	144.3
h_n	100	30	100	40

5.2 Cleanroom optimization for high resolution and high aspect ratio structures

The photolithography and development process on a SU-8 2050, near-UV photoresist has been optimized in order to obtain high aspect ratio structures. SU-8 is a negative photoresist which crosslinks upon UV-exposure. It is typically spin coated onto a silicon wafer and it is structured using a series of baking steps before and after the micropatterned UV-exposures. As described by Mata *et al*. (263) and Lorenz *et al*. (264), the fabrication of high aspect ratio SU-8 structures can suffer from difficulties arising from the use of traditional processing steps that were developed for low aspect ratio structures. These difficulties preventing high aspect ratio microstructure fabrication arise from the following effects: edge beading, wafer bowing and resolution of UV-exposure.

The first effect is edge beading, where the SU-8 layer has an uneven surface because it is higher near the wafer edge compared to its center (Fig. 30A). During the spinning step, the photoresist

moves outwards from the center of a wafer due to centrifugal force. However, when working with low spinning speeds and high viscosity resists (12900 cSt for SU-8 2050), the photoresist typically accumulates at the edges of the wafer because of surface tension, evaporation and viscosity effects (265). As a result, the accumulated material does not reflow just by gravity resulting in thicker areas near the edges. This uneven surface then creates an air gap between the photoresist and the mask which is detrimental to the resolution of exposed structures due to increased diffraction (Fig. 30D). However, this edge can be removed by spinning the pre-baked wafer and rinsing the outer edges (ca. 5-10 mm) with a continuous stream of developer (see edge bead removal protocol in experimental section 4.3). This continuous stream at a fixed position was achieved by mounting a small tube (inner diameter 380 µm) a few mm over the SU-8 surface as illustrated in Fig. 30B. Once the edges were removed by the developer, the surface of the photoresist was uniform as shown in Fig. 30C. The edge bead from each SU-8 layer is removed prior to coating consecutive SU-8 layers to avoid any thickness build-up at the wafer edges.

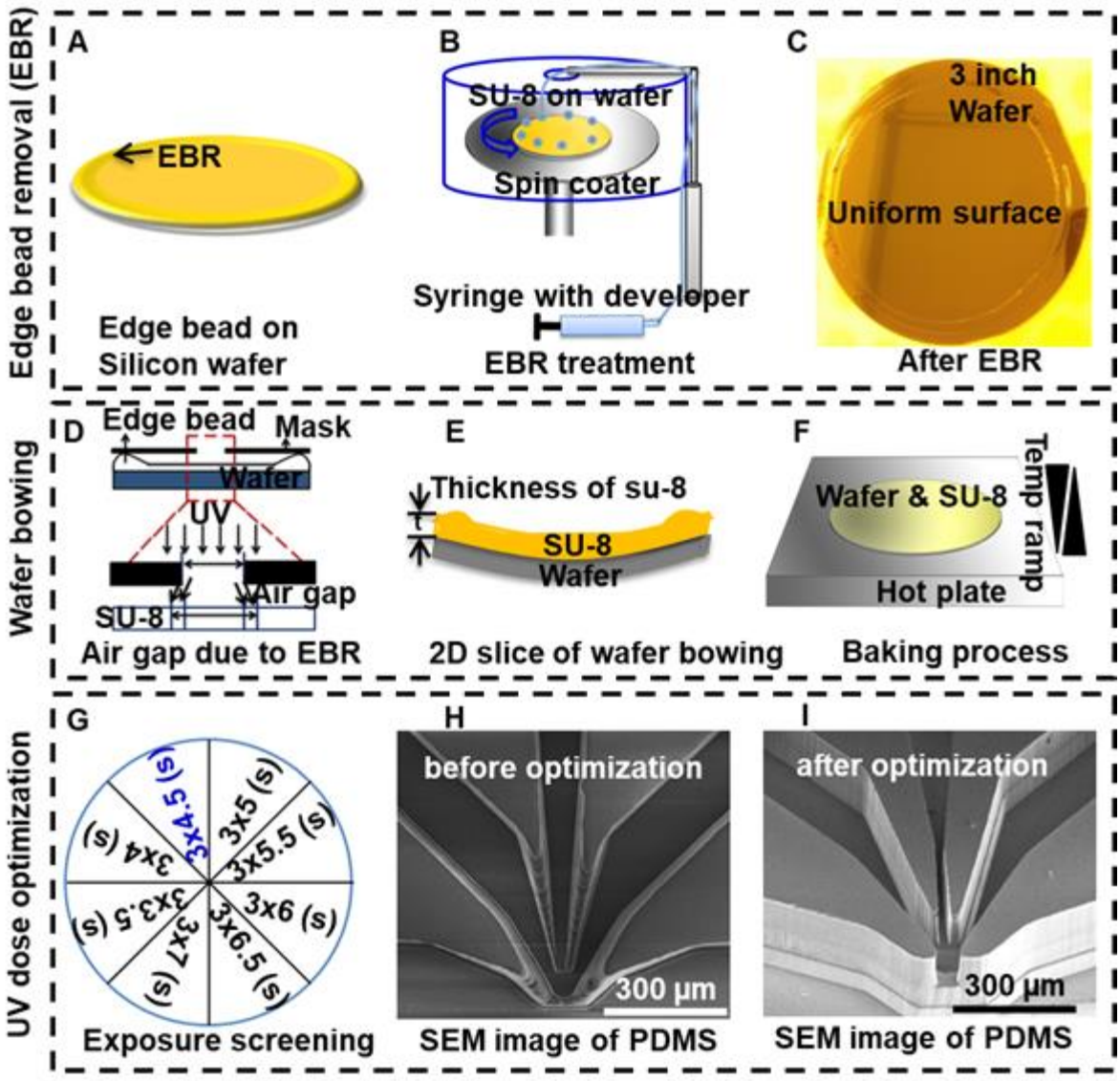

Fig.30: Overview of the challenges and optimization steps for obtaining high aspect ratio molding structures. (A) Edge beading from accumulated material near the wafer edges. (B) Removal of beaded edge by applying developer stream after the baking step resulting in an edge-free wafer (C). (D) Thicker edge would otherwise increase diffraction and light bleeding through a bigger gap between the mask and the resist. (E) This gap is even enhanced by wafer bowing caused by residual tensile stresses from thermal expansion coefficients mismatch. (F) This bowing effect can be overcome by controlled and lowered temperature rates during the baking processes. (G) Screening of UV exposures for achieving highest resolution. (H,I) Scanning electron micrographs of the replicated structure by molding with PDMS before and after all the optimization steps.

The second effect is wafer bowing where residual tensile stresses, resulting from a mismatch in thermal expansion coefficients of silicon and SU-8 during pre-baking, cause cracks in the SU-8 and bowing of the coated Si-wafer (Fig. 30E). This wafer bowing effect is further enhanced when stacking multiple SU-8 layers, as for this work. As a consequence of this effect, the previously mentioned gap between the mask and resist is enhanced which lowers the achievable resolution and aspect ratios. Furthermore, the wafer bowing effect also hinders the correct alignment and registration of masks with previously-exposed structures in SU-8 because the wafer does not lie fully flat on the wafer carrier. By reducing the tensile stresses through controlled and lowered temperature rates during the baking processes, the wafer bowing could be avoided and high aspect ratio and high resolution structures were achieved (Fig.30F). Once the edge bead is removed and the wafer bowing is reduced, operating the mask aligner in vacuum mode, to enhance the contact between photomask and SU-8, will further improve the achievable feature resolution.

The third effect preventing the fabrication of high aspect ratio structures is the loss of resolution during UV exposure due to an incorrect UV dose or from light bleeding from diffraction. The incident UV exposure triggers the photoacid in the exposed areas which then locally catalyzes the ring opening polymerization of SU-8. If the amount of this available catalyst is too low, i.e. from over- or underexposure with UV light, the degree of cross-linking is reduced resulting in missing structural features (Fig. 30H). Therefore, the maximum achievable resolution of the structured SU-8 depends on the optimal UV dose deposited on the photoresist as well as the definition of the exposed pattern (Fig. 30I). While the UV dose can be optimized by controlling the light intensity and exposure time (Fig. 30G), the definition of the exposed patterns depends on different factors. On the one hand, the edge bead and uneven wafer result in an air gap between the photoresist and the mask which in turn increases UV light scattering and lowers the achievable resolution. On the other hand, different mask types, such as emulsion film- or chromium masks, come with different resolutions which limit the achievable SU-8 structure feature size. Optimizing these two aspects will limit diffraction effects and increase the definition of the exposed patterns. An example comparing the achieved microstructures before and after all optimization steps is shown in Fig. 30H and 30I, respectively.

Once these optimized process parameters are finished, steps are repeated three times to obtain the desired number of layers for a 3D focusing device. The optimized master structure was replicated with PDMS, as stated by Trebbin *et al* (7).

The optimized procedure follows for all other microfluidic liquid jets, which are whipping and fiber jets shown the parameters in Table 5. The final SEM images of channel dimensions and nozzle outlet were shown in Figs. 31 and 32 for high aspect ratio structures.

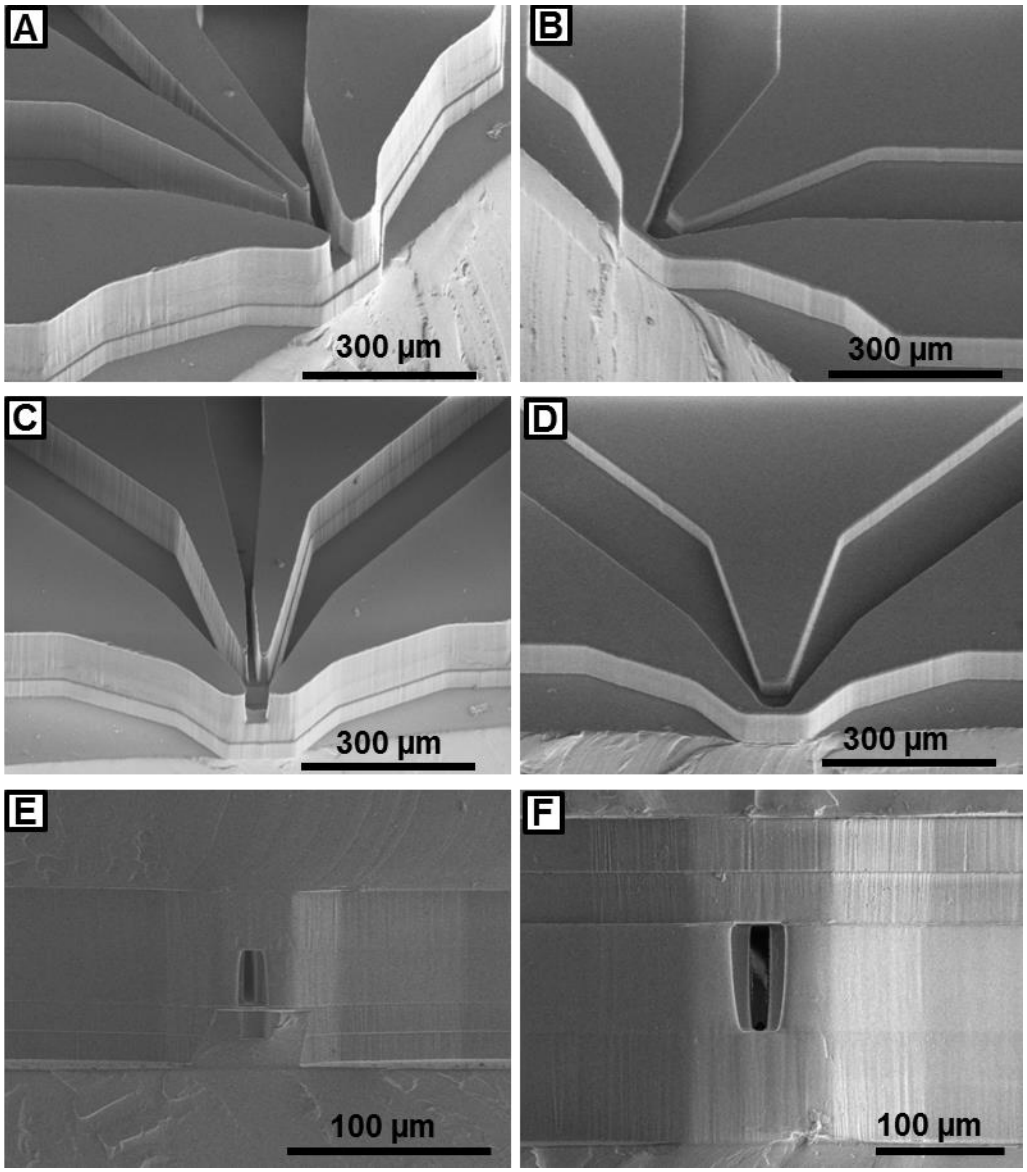

Fig.31: After process optimization: (A-D) scanning electron microscopic images show the PDMS halves of a 3D nozzle prior to the subsequent device bonding steps, (E, F) nozzle exits with respect to height for flat liquid jets.

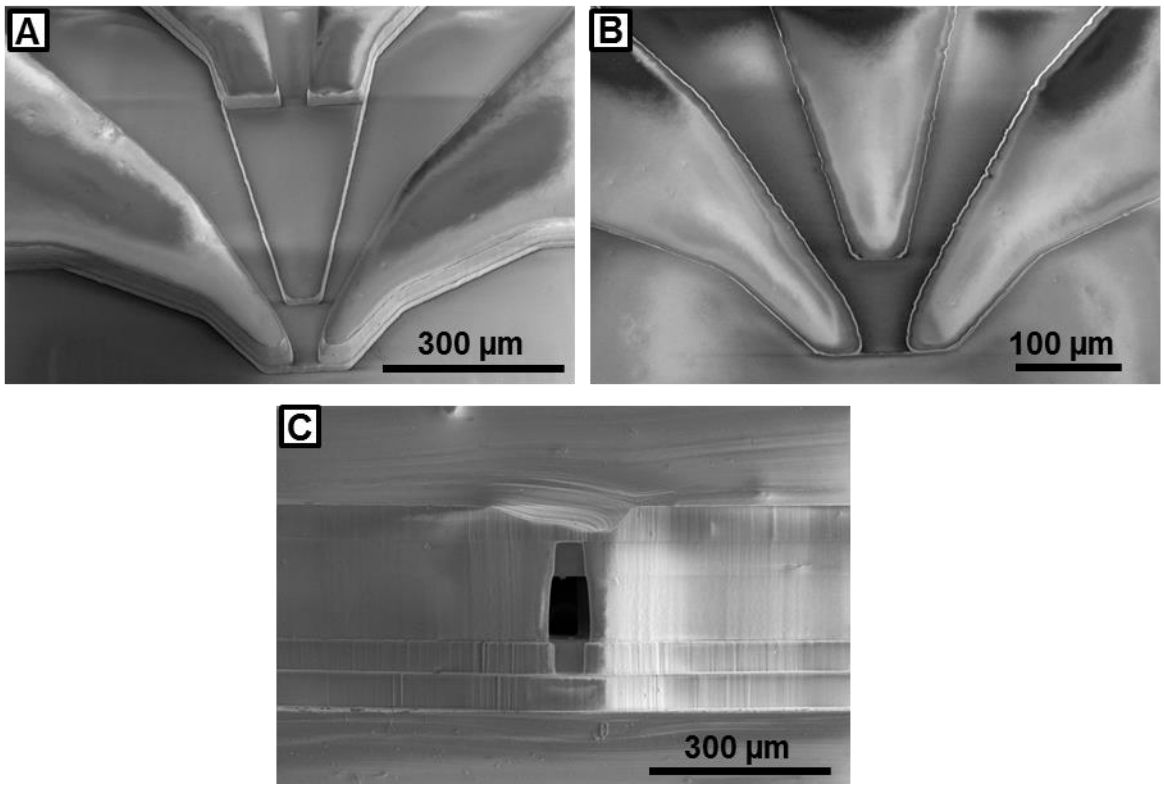

Fig.32: After process optimization: (A and B) scanning electron microscopic images show the PDMS halves of a 3D nozzle prior to the subsequent device bonding steps, (C) nozzle exits with respect to height for whipping jets.

5.3 Development of a stable microfluidic flat liquid jet system

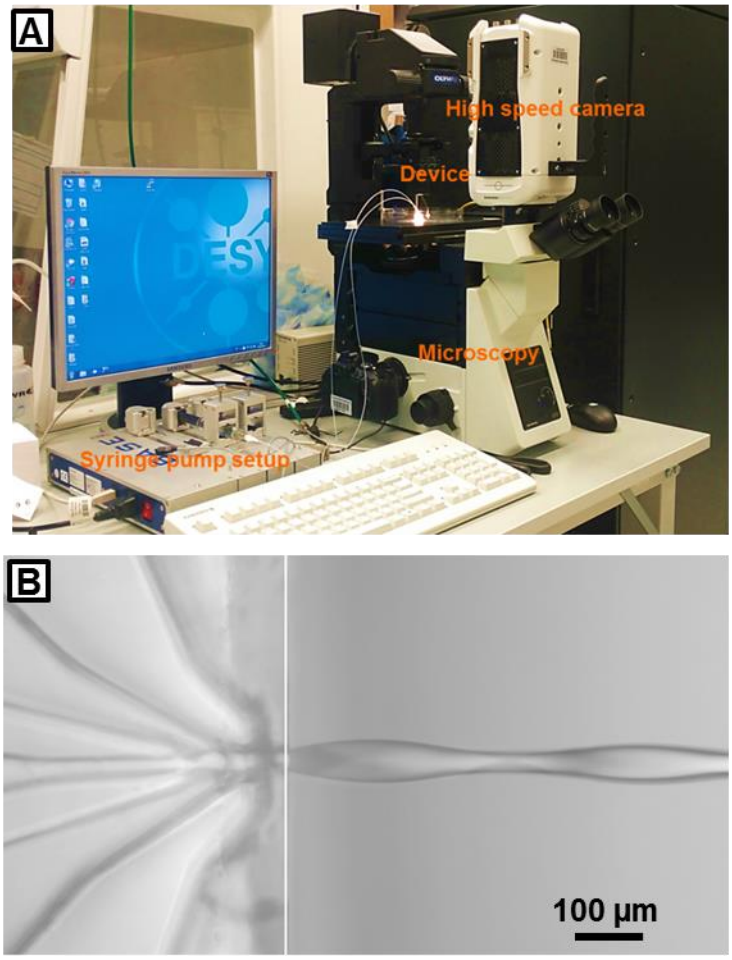

Fig.33: (A) Experimental set up: high-speed camera connected with microscopy (B) The water enters the nozzle and is shaped by the pressured airflow and the geometric device design. Moreover, this results in a constant and stable liquid jet. The image is merged from two frames (separated by the white line) at different focus positions due to the optical distortion of PDMS and is indicated by a white line.

The experimental set up consisted of a high-speed camera (Phantom v711 camera, Vision Research Europe) coupled to an optical microscope. The microfluidic device was connected with tubing (inner diameter 0.381 mm, outer diameter 1.09 mm, Scientific Commodities) to a gas-tight 1700 Series Syringes by Hamilton and mass flow at 43 to 352 standard cubic centimeters per minute (SCCM). While the experiment was running, the device and the jet could be observed

with the high-speed camera connected to a microscope. The different flow types are captured a sample rate 160,000 fps and at an exposure time of 3 µs, as shown in Fig.33.

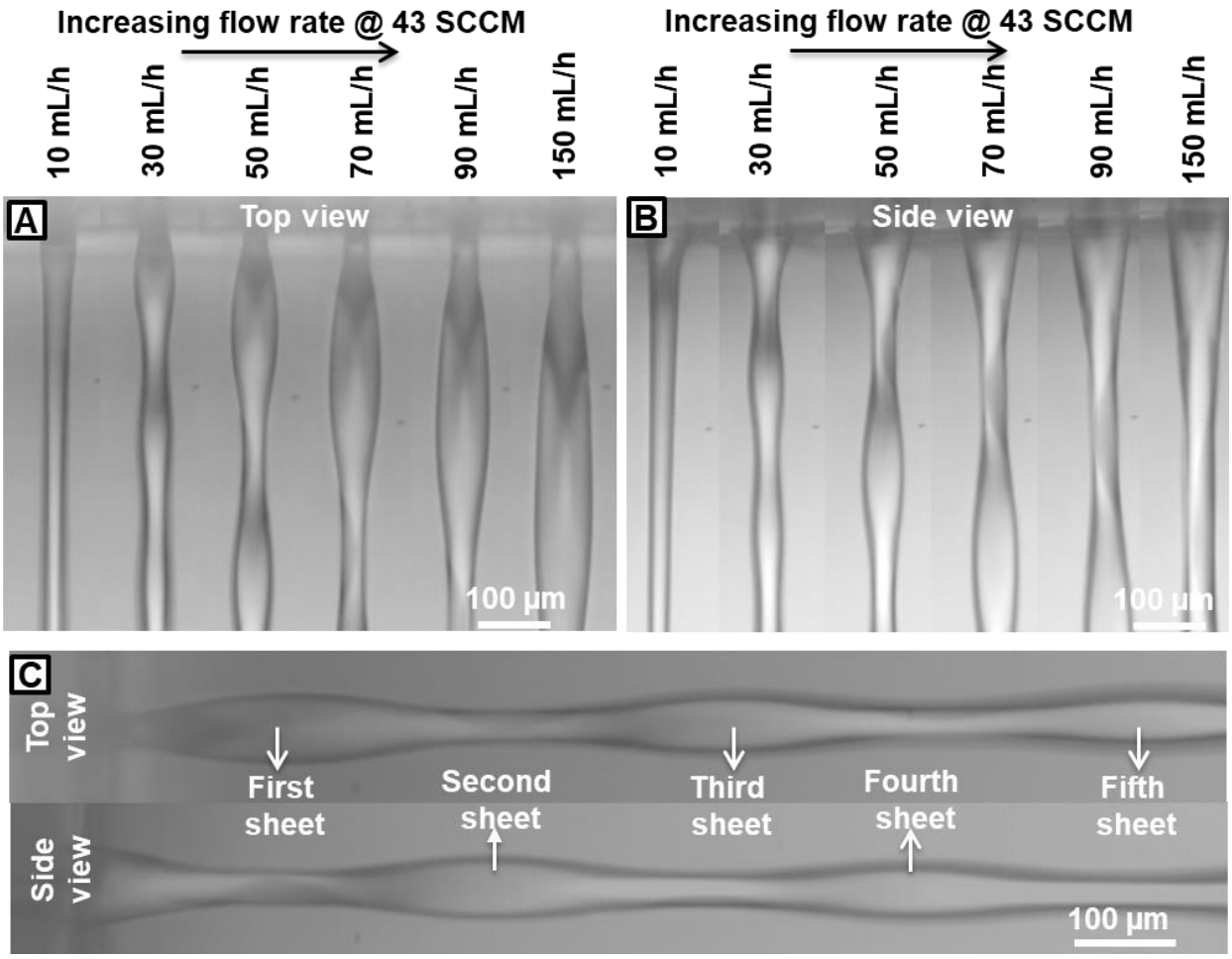

Fig.34: Sheet diameter control visualized by microscopic images from (A) top view and (B) side view of the microfluidic flat liquid jet nozzle during operation. The change of sheet diameter and length at varying flow rate is shown and the measurements were taken at the nozzle outlet at constant pressure at 43 SCCM. (C) The nozzle produces a series of liquid sheets; the one closest to the nozzle is the widest and longest, each sheet is perpendicular to the previous one as shown in the two microscopy images from orthogonal view angles.

The jet at the outlet of the flat liquid jet was imaged to analyze the relationship between its sheet width and length w.r.t. varying flow rate at constant pressure at 43 SCCM. We observed the trend that the sheet width and sheet length were increased while increases liquid flow rates, as shown in

Fig. 34. In this image series at atmospheric ambient pressure, the flow rates were varied between 10 mL/h to 150 mL/h at constant compressed mass flow 43 SCCM which result in width of the first sheet between 32 µm and 71 µm. The sheet closest to the nozzle was the first sheet and it is progressively wider in sheet width and sheet length than other following series of sheets.

Here, the radial momentum to the liquid from the initial flow focusing causes it to spread into a thin sheet, bounded by a thicker fluid rim. The sheet becomes progressively thinner moving outward away from the jet central axis and along the streamlines. Downstream from the gas-liquid interaction point, surface tension eventually overcomes the radial momentum, causing the thick rims of the sheet to reconverge, which then, in turn, produces a smaller sheet in the orthogonal orientation due to momentum conservation. This process repeats, resulting in a series of alternating orthogonal sheets, as shown in Fig. 34 C. We assume the decay to originate from energy dissipation and to depend on the interplay of the liquid's viscosity and surface tension. Therefore, the sheet closest to the nozzle, the first sheet, gets progressively broader and thinner as gas flow is increased, allowing in situ control of the sheet dimensions. The use of a focusing gas allows us to reduce the liquid flow rate by order of magnitude relative to traditional colliding liquid jets for liquid sheet formation, resulting in much thinner sheets.

5.2.1 Nozzle height control

The flow tests of liquid for various nozzle shape geometries were conducted in standard atmosphere at a constant pressure. The generation of liquid sheets is depicted in Fig. 35, where panel a show a series of images with respect to varying height of the nozzles. The gas flow rate was kept constant at 43 SCCM, but the liquid flow rate was increased incrementally from 10 mL/h to 150 mL/h. The sheet diameter is measured manually using ImageJ at multiple positions directly next to the nozzle exit. As shown in Fig.35 (A), at a lower flow rate, the jet seems circular and can observe the droplet breakup. Further, the length of the continuous jet, before it breaks up into droplets, increases while increasing the flow rate and started sheet-like behavior. While increasing the nozzle height from 50 µm to 100 µm (both with a width of 15 µm), the jet started forming sheet-like flow, as shown in Fig.35 (B).

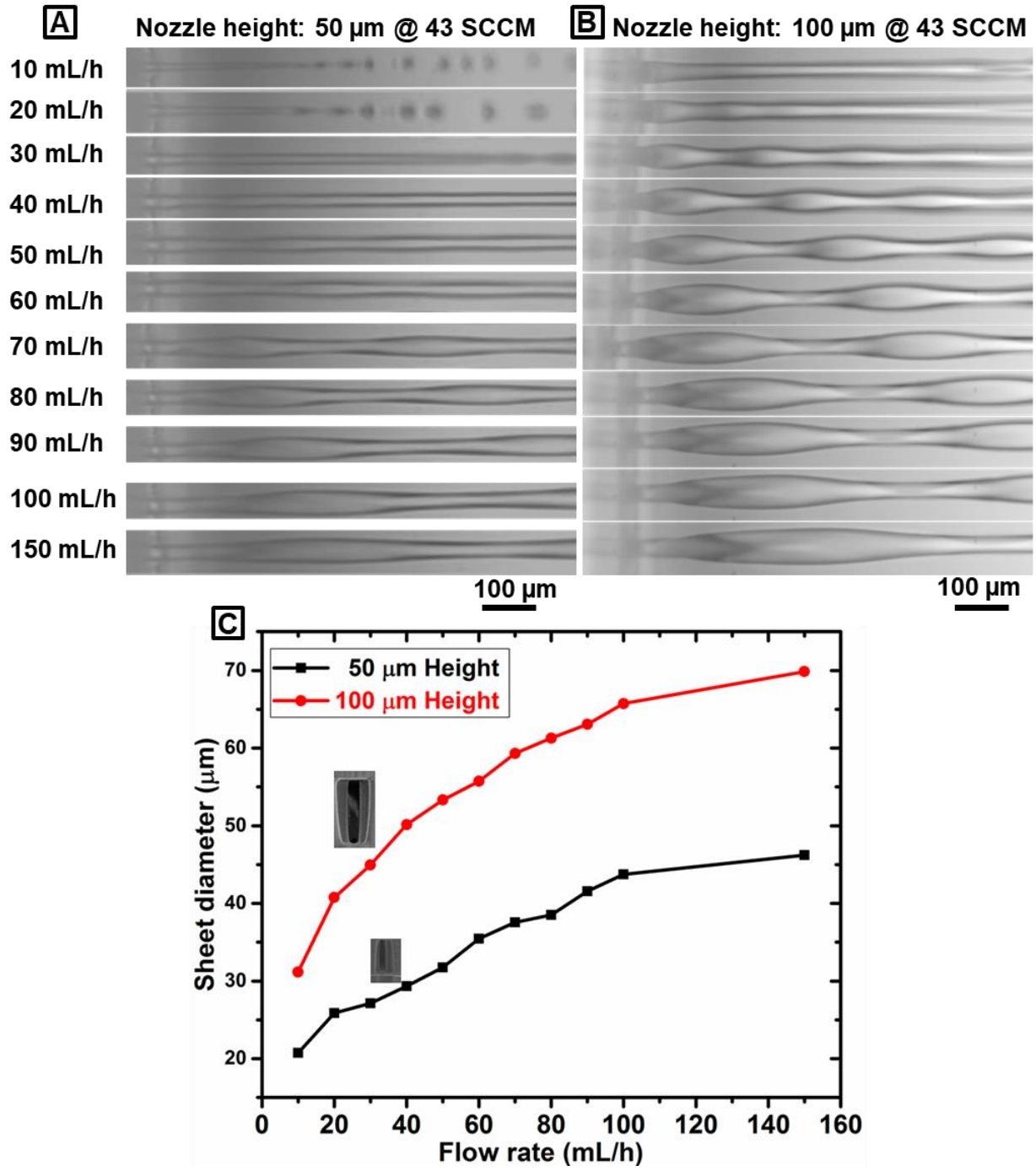

Fig.35: Sheet diameter control visualized by microscopic images of the microfluidic flat liquid jet nozzle height of (A) 50 µm and (B) 100 µm during operation (both at a width of 15 µm). The change of sheet diameter and length at varying flow rate is shown and the measurements were taken at the nozzle outlet (as indicated by the dotted line). (C) Comparison plot of the measured sheet diameters with the two different nozzles dimensions at different flow rates at constant pressure at 43 SCCM.

We observed the trend that the sheet width and sheet length were increased while increases nozzle height as shown in Fig. 35 (C). The physics underlying this sheet formation is similar to that underlying the formation of a sheet by two colliding cylindrical liquid jets (196). These fluid dynamical theories are particularly interesting for non-gas focusing liquid jets and that can be applied to the GDVN based microfluidic flat liquid jet devices as well. Furthermore, this would help tremendously with the theoretical prediction of jetting behavior as well as the development of future optimized devices. Such future optimized devices could potentially be used to generate thin sheets towards nanometer thickness at a constant and controllable rate if the flow rates and other relevant experimental parameters are adjusted accordingly. Moreover, nozzle height control has important implications for the integration of microfluidic liquid sheet devices for X-ray spectroscopy study because the thickness of the liquid stream dictates the absorption and proximity of the X-ray beam to the nozzle at a given flow rate.

5.2.2 Sheet diameter and length study

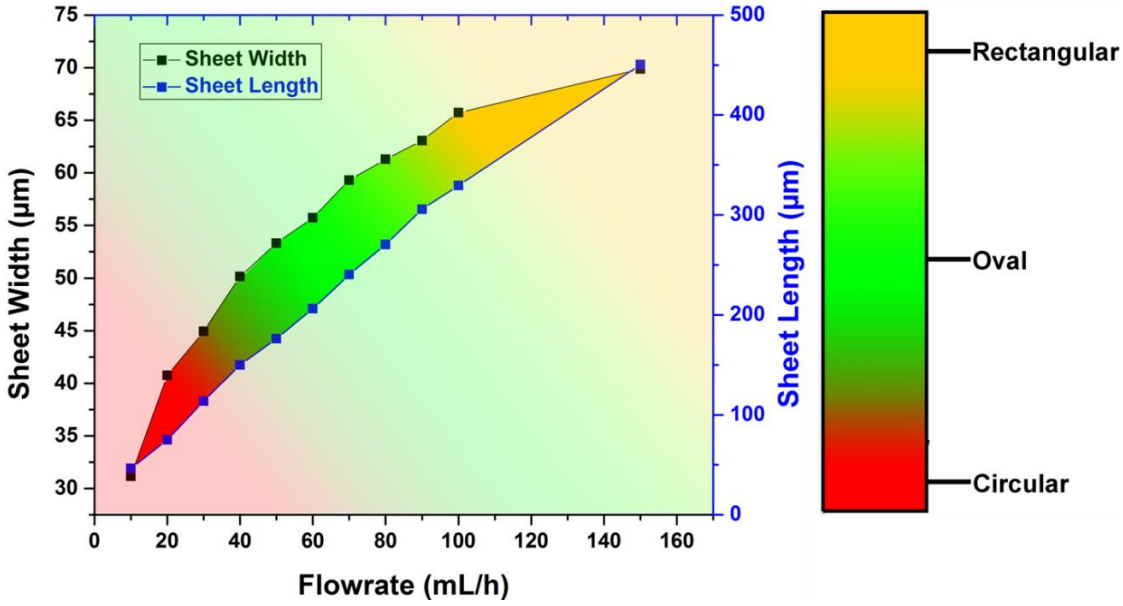

Fig.36: Phase diagram of flowrate vs. diameter vs. node distance at constant pressure.

As shown in Fig 35 (B), the sheet diameter and length increases while increasing the liquid flow rate at constant gas flow. Further, the high-speed video setup allows the experimental classification of the sheet diameter and length control. This sheet spreads and widens symmetrically along the flow direction. Surface tension forces eventually dominate the outward

liquid inertia limiting the dimensions of the sheet and causing the sheet to contract back. The rim regions of the sheet recruit liquid from the sheet and grow as the sheet contracts back on itself, eventually forming a downstream secondary sheet oriented in the flow direction. At lower liquid flow rate, the sheets are roughly oval (as shown in Fig.36) and oriented alternately in the perpendicular to the flow direction and the flow reminiscent of fluid chain structure. As increasing the flow rate, the sheet transfers from an oval shape to a rectangular or flat shape, which can observe in Fig. 35 (B).

5.2.3 Pressure and viscosity effects on liquid sheet

Surface tension forces dominate thin sheet flows. As a result of surface tension at the edges of the sheet, a flow that begins with a dimension, perpendicular to the flow direction, coalesces to a point at a distance, in the flow direction. As shown in Fig.37, the high-speed video camera images demonstrate that liquid sheets with high surface tension and viscosity were more resistant to disruption and also showed that an increase in viscosity from water to PEG 33%, the liquid revealed less surface waves and was more resistance to a breakup of the jet.

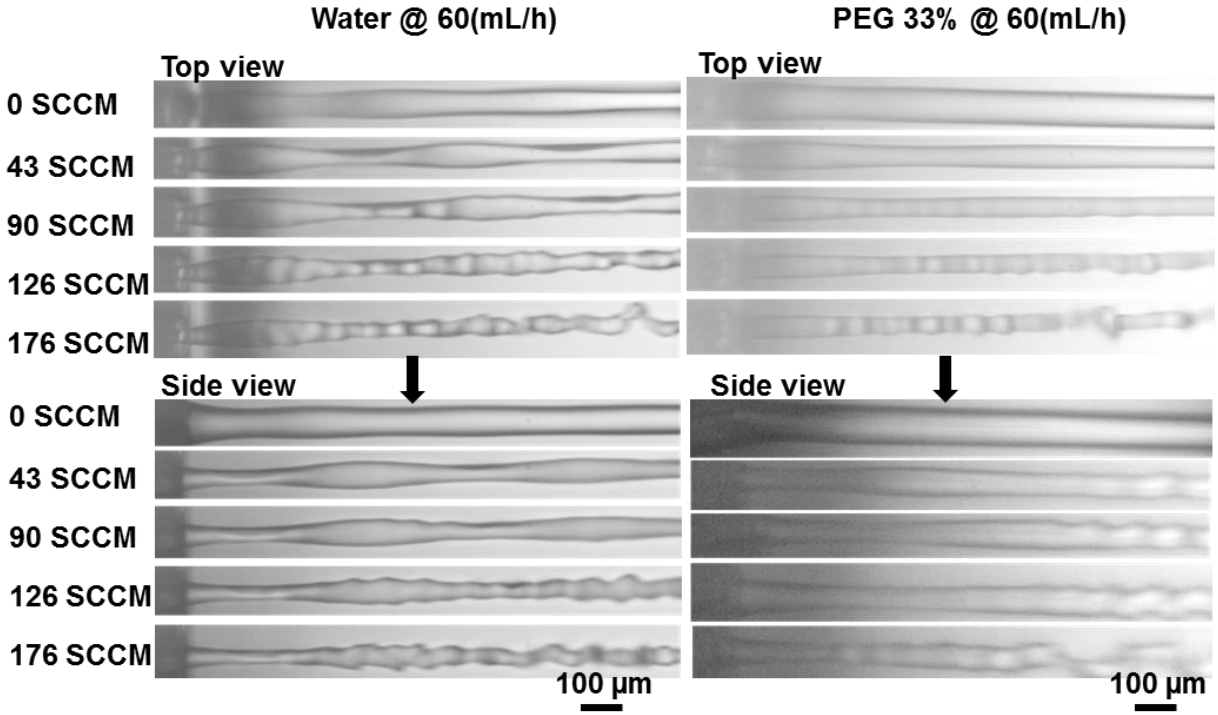

Fig.37: Comparison of viscosity effect (left top & bottom are with water and right top & bottom are 33% PEG solution) on sheet diameter and length at different pressures at a constant flow rate of 60 mL/h.

The sudden increase in static pressure at the exit of the nozzle results in the decrease in the driving fluid momentum, described by the convective term in the Navier-Stokes Equation (Eqn. 1). As a result, the dissipation increases with the increase in surface energy and the tendency to form droplets. Since, the shear stress is retained, the increase in dissipation is delayed, resulting in varicose perturbation, i.e, wavy effect.

For a given flow rate, here 60 mL/h, varying the coaxially focusing gas flow rate enables us to picture the Rayleigh instability with maximum perturbations. The increase in the flow gas pressure, i.e. increase in the coaxially flowing gas flow rate results in Kelvin-Helmholtz (KH) instability with m = 1 mode (266). At this stage (at high gas pressure), the KH instability tends to imbalance the viscous forces with the capillary forces of the free liquid jet. Furthermore, this results in quicker breakup of the liquid jet.

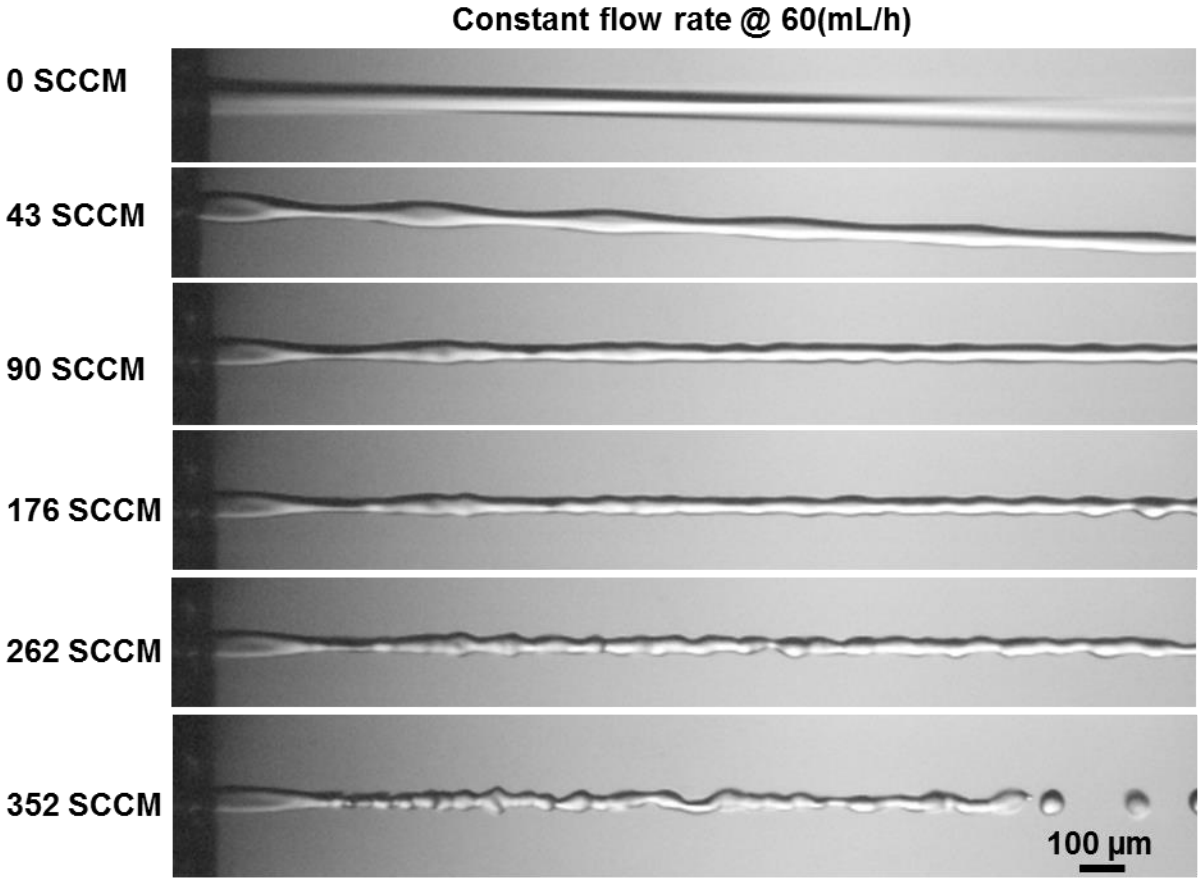

Fig.38: Effect of pressure on thin sheet waves (wave oscillation) at a constant flow rate of 60 mL/h.

With the decrease in the axial momentum of the liquid, the Plateau-Rayleigh instability initiates. However, Fig.38 shows the Chandrasekhar instability [266] due to the increase in the axial pressure gradient between the two co-axially flowing fluids. The increase in Reynolds number (Re) of air increases the critical Taylor number (T_c) written as,

$$T_c = 1708 + 26.5\, Re^2 \tag{31}$$

thereby conveying the onset of instability with the increase in air flow rate.

5.4 WAXS on microfluidic liquid sheets

The flow orientation of anisotropic particles in fluids is of importance in many fields ranging from the spinning and molding of fibers to the flow of cells and proteins through thin capillaries. For example, the material properties of CNT-enhanced polymers and silk fibres strongly depend on the nanoscale alignment of the particles inside the material. Anisotropic flow fields influence the flow of cells in capillaries and the aggregation behavior of proteins. GDVN based microfluidic flat liquid jet devices offer great potential for the analysis of (complex) fluids or anisotropic particles under defined shear and elongational conditions. The controlled design of micro geometries enables the generation of defined shear fields within the jet flow suitable for the study the orientation of anisotropic particles therein. The implementation of microfluidic liquid sheets is desirable because it enables flow orientation experiments (using X-rays) at very high shear rates. The gas focusing allows high pressures and shear stress distributions, which can be 2-3 orders of magnitude higher than traditional rheological experiments [159]. It is known that colloidal liquids under high shear forces and significant deformation rates can form nano-/microstructures, such as flocculated systems or layering of particles, which can change its bulk properties (e.g. viscosities). It is of high interest to investigate these effects and their influence on structures under high shear conditions by rastering flat liquid sheets with a micro-focused X-ray beam.

In the framework of this thesis, spindle-shaped hematite particles were prepared by forced hydrolysis of iron salt solutions at elevated temperatures based on the procedure of Ozaki et al. [267] (collaboration work with Prof. Grubel group). The morphology and the microstructure of the hematite samples were characterized by SEM at Nanolab (DESY) shown in Fig. 39.

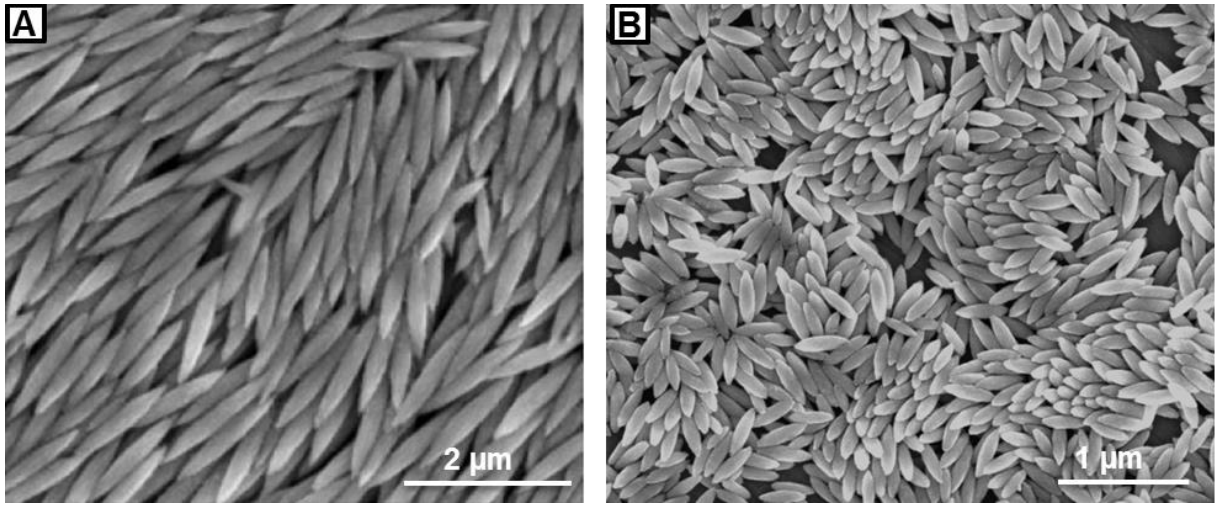

Fig.39: SEM micrographs of hematite samples (A) H1 and (B) H2 with an aspect ratio of v = 10 and 3.3, respectively.

In order to continuously produce stable liquid sheets that can be studied by microfocus X-ray scattering, a setup consisting of a high aspect ratio microfluidic flat liquid jet system was developed. It can generate stable liquid sheets and recycle the sample back to the microfluidic flat liquid jet to lower the amount of required sample.

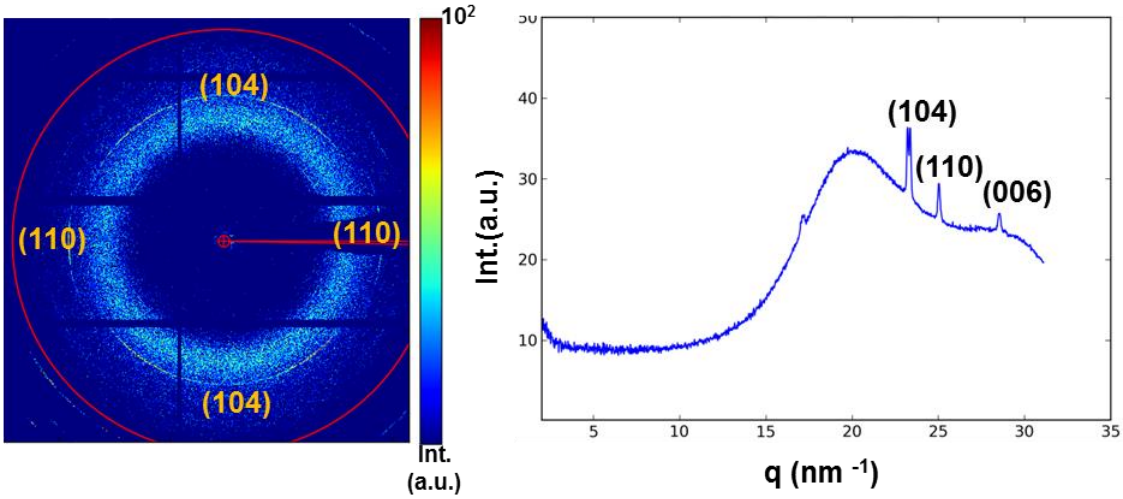

Fig.40: Diffractograms of sample H1 (v =10) hematite spindles at center of the first sheet and corresponding reflections (104) and (110) respectively produced at flow rate 60 mL/h.

Here, the optimized high aspect ratio nozzles with 100 µm height and 15 µm width of inner dimensions have been used to generate stable liquid sheets at a flow rate of 60 mL/h. The local orientational distribution of the dispersed anisotropic nanoparticles within the stable liquid sheet

is determined by scanning the liquid flqt jet containing anisotropic hematite nanoparticles with a 3 x 3 µm beam across and along the stable liquid sheet.

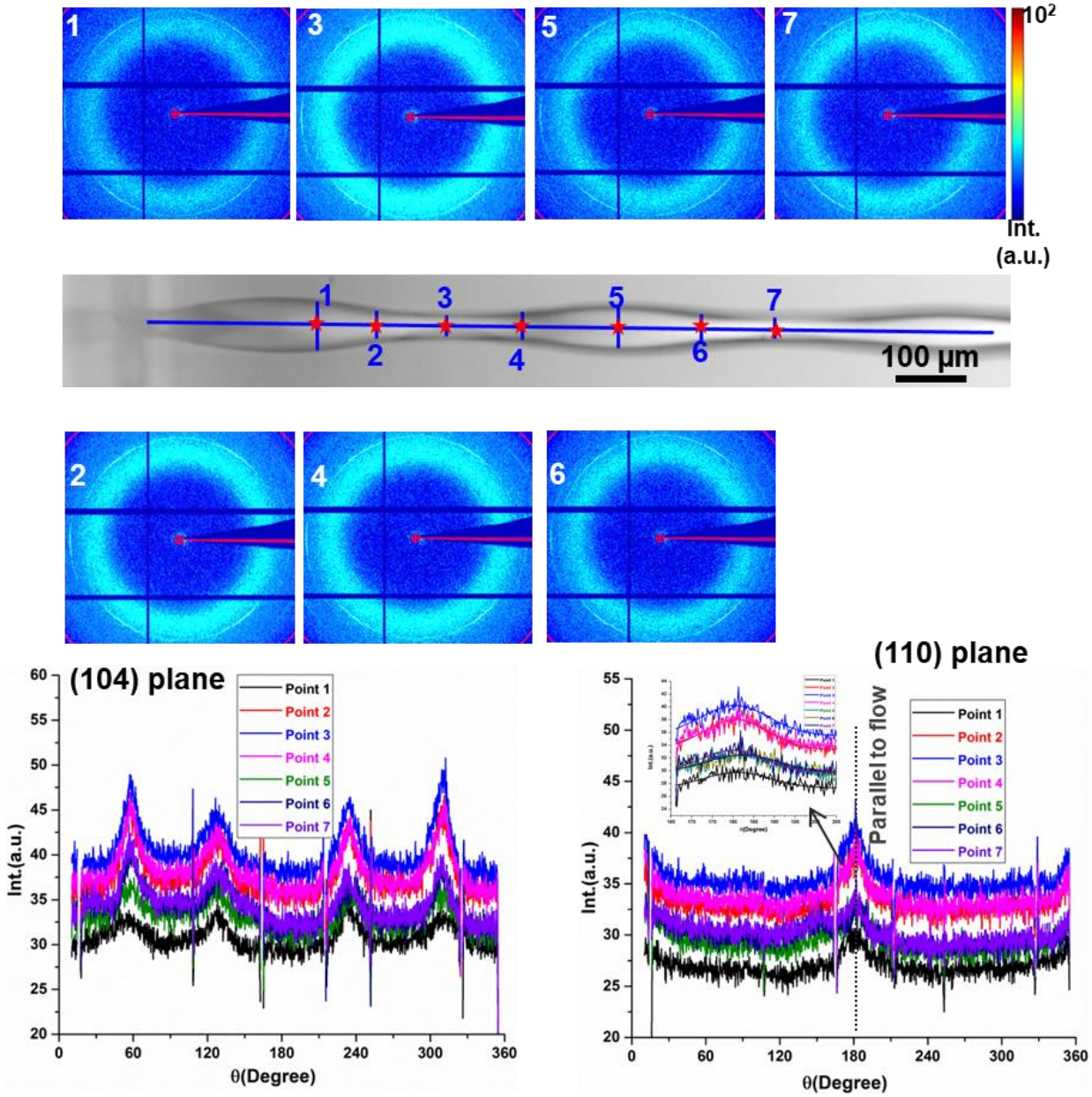

Fig.41: Scheme of stable sheet with dispersed hematite nanoparticles together with the WAXS patterns measured center of the sheet up to 170 µm sheet length. The corresponding azimuthal angle intensity profiles are shown below for each reflection. The scattering patterns indicate a parallel alignment to the flow axis.

WAXS patterns were collected at different distances along and across to the liquid sheet flow direction and towards the downstream direction of the nozzle allowing to build a map of the particles rheological behavior. The observed Bragg diffractions along and across the jet have been analyzed to study the alignment of spindle-shaped hematite particles in a sheet flow. Fig.40 shows the intense Bragg reflections from the hematite crystal structure at q = 23.3 nm^{-1} (104) and at q =25 nm^{-1} (110) at the center of the sheet, indicating a horizontal alignment.

Fig.41 displays the WAXS patterns of the hematite nanoparticles of aspect ratio 10 (650 L x 65D) measured at scan positions of center of the sheet up to 4 crisscross node formation. The extracted data showed a spindle orientation with the center of the sheet along the jet parallel to the flow direction. The observed Bragg reflections are (104) and (110) shown in Fig.40. For (110) from the two expected reflections, only one is completely visible since the detector partially covers the second reflection. The azimuthal angle of each Bragg peak is shown in Fig.41 was extracted for analyses of the scattering patterns. The azimuthal peak position shows parallel alignment along the sheet with no noticeable angle deviation. The peak full width at half maximum (FWHM) analysis shows wide angular distribution as shown in Fig.41. The peak distribution curves indicate weak alignment at center of the sheet (point 1) comparing to the flipping region (point 2).

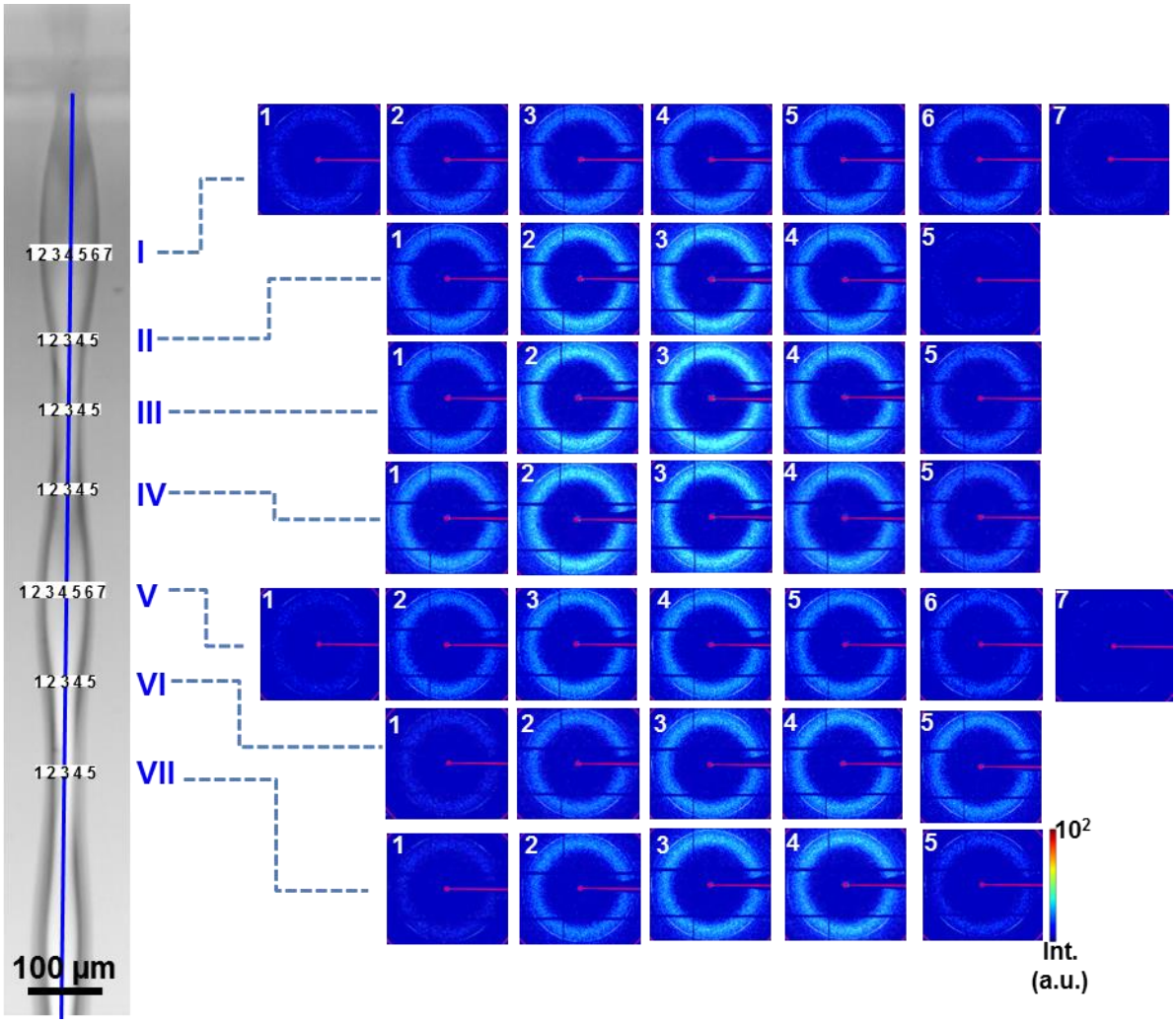

Fig.42: Scheme of stable sheet with dispersed hematite nanoparticles together with the WAXS patterns measured at across the sheet for 5 flipping zones up to 170 µm sheet length and the flow rate at 60 mL/h and mass flow rate at 43 SCCM.

From this, one can conclude that the effects of rotational diffusion are negligibly small for the spindle-shaped hematite nanoparticles at the center of the sheet. There is an experimental example of particle alignment for GDVN-spun fibers in the next chapter, which also shows a similar preferred orientation of anisotropic hematite particles along the fiber axis.

It is interesting whether the orientational changes observed for a sample of hematite nanoparticles of the same aspect ratio (ν=10), across the sheet at different scan positions of nodes. The resulting scattering patterns are shown in Fig.42. WAXS patterns were analyzed in different c-axis

deviations 0 to 360^{o}. The resulting WAXS patterns were plotted via the azimuthal angle intensity profiles with respect to each reflection for (104) and (110).

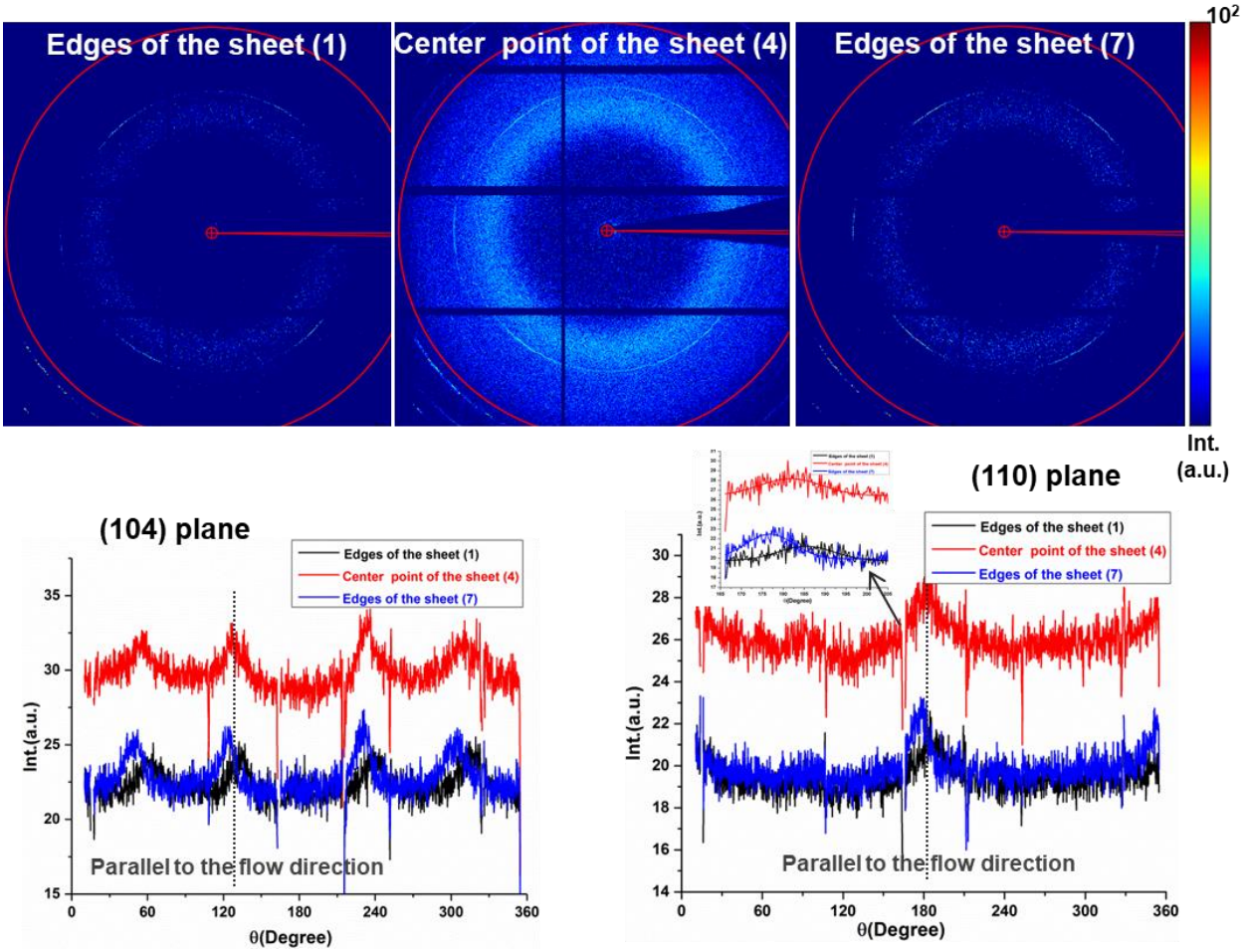

Fig.43: Diffractograms of sample hematite nanoparticles with aspect ratio 10 inflow patterns measured across the sheet regime I of scan points number 1, 4 and 7 of each distance between scan points is 21 µm.

The first observation of the starting node across the scan positions near to edges of the rims and center of the sheet is shown in Fig.43, which was measured in the liquid sheet. The WAXS patterns are characterized with respect to azimuthal angle intensity profiles. FWHM curves indicate weak alignment at center of the sheet (point 4) comparing to the edges of the sheet (points 1 and 7). It shows, the particle orientation at outer pattern is slightly tilted clockwise (cw) at an angle of 185^{o}, other one is slightly tilted counterclockwise (ccw) at an angle of 176^{o} with respect to center point of the sheet at an angle of 181^{o} as shown in Fig.43 for both the reflections (104) and (110) planes. Furthermore, this is due to shear forces possibly enhanced by gas

focusing, from the rims to the center of the sheet, where the shear rates are smaller, leading to reduced orientational order at center.

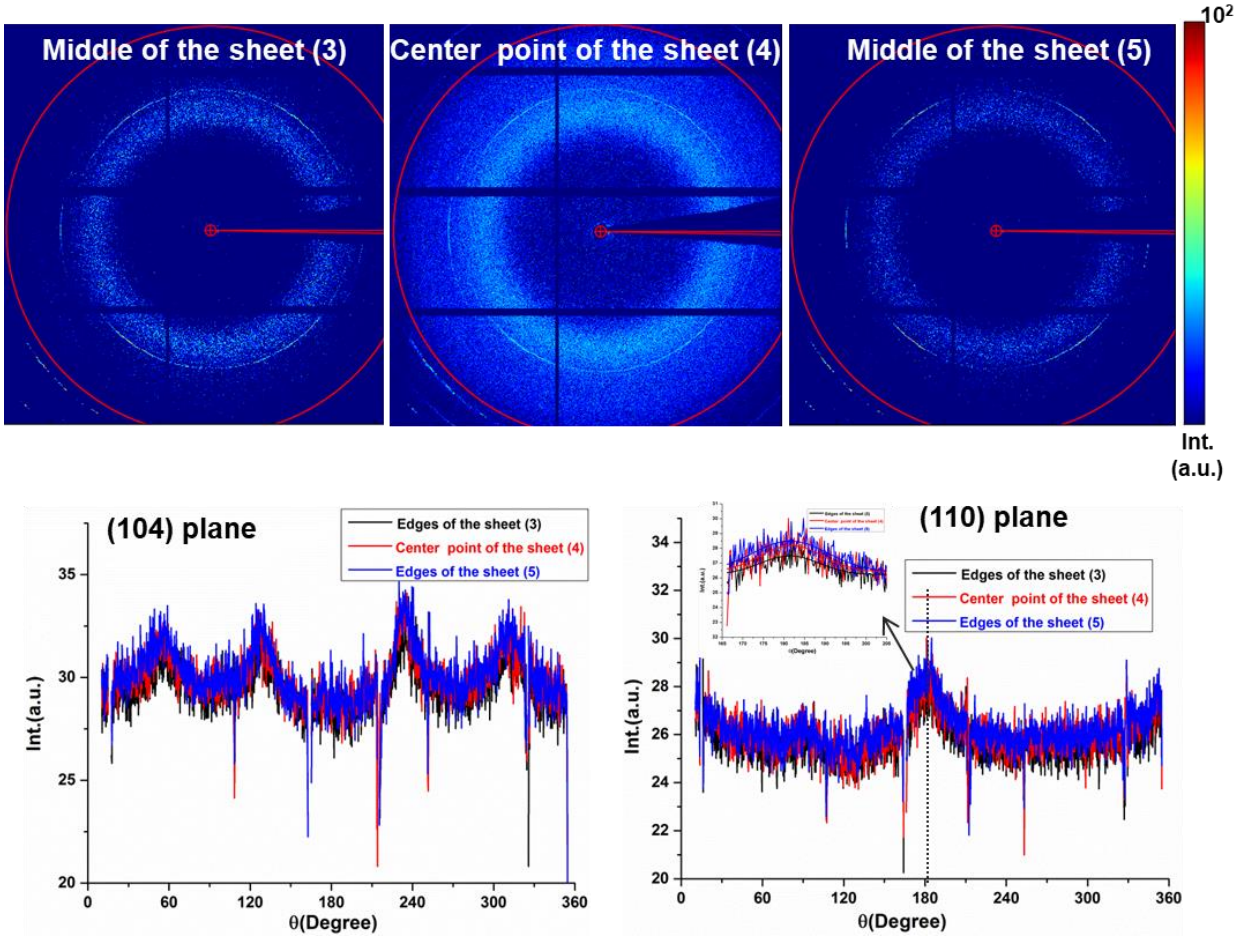

Fig.44: Diffractograms of sample hematite nanoparticles with aspect ratio 10 inflow patterns measured across the sheet regime I of scan points number 3, 4 and 5 of each distance between scan points is 6 µm.

A similar observation was done at the same node at different scan positions near the center of the sheet, as shown in Fig.44. The azimuthal angle intensity profile shows almost the same alignment with 0^o inclination angle. Thus, the result indicates an alignment of the nanoparticles (spindle-shaped) inflow direction at center of the sheet is particles orient parallel to the flow direction, corresponding to a 0^o inclinational angle and angle deviation increases towards the rims of the sheet with angle $4^o \pm 1^o$ with patterns clock and counter-clockwise direction with respect to center point of the sheet pattern.

5.5 Spinning of functional polymer microfibers using GDVN based microfluidic devices

(This work has been published in Scientific Reports 9: 14297 (2019, DOI: 10.1038/s41598-019-50477-6)

Microfluidics has become an important topic during the past years. Fibers have been successfully spun using microfluidic techniques, but to our knowledge, single fibers with controlled diameters in the nm-range have not yet been achieved via the here-presented microfluidic approach (139, 153,154). Developing a new method for spinning fibers using Gas Dynamic Virtual Nozzles (GDVN) microfluidic devices allows the combination of advantages from coaxial spinning, electrospinning and blow spinning, while minimizing the current drawbacks of the individual techniques. GDVNs have been developed to allow the formation of free-standing liquid jets by gas-flow-focusing liquid samples (160). The main advantage of this GDVN-technique is that the liquid does not contact the nozzle exit surface which allows for smooth, reproducible and continuous operation of the nozzle for long periods of time by avoiding the deposition of material at the nozzle exit.

Very recently, Hofmann *et al.* demonstrated the first use of a microfluidic GDVN for fiber spinning (139), obtaining continuous fibers in the micrometer range by gas flow-focusing in a nozzle and coupled with fiber pulling. The fiber pulling step spools the fiber onto a surface and the spooling speed determines the final fiber diameter. Here, we demonstrate the development of a different microfluidic GDVN nozzle capable of continuously producing fibers down to nm-diameters without the need for external fiber spooling. Its reliable operation was made possible through our optimized gas flow-focusing geometry with very stable jetting regimes over large ranges of jetting conditions. This geometry also enables the production of fibers with a diverse range of surface and morphology characteristics, while maintaining a small diameter, not easily achieved by previously described methods (149). Furthermore, nanocomposite fibers were also produced and shown to be easily accessible with this nozzle geometry, with the microfluidic design relieving problems such as clogging from the nanoparticle flow.

GDVN-based micro-/nanofiber spinning has the potential to simplify current production processes and minimize the required space and equipment for manufacture. Furthermore, due to the applied rapid prototyping approach inherent to UV- and soft-lithographic techniques, nozzles

with different characteristics can be easily designed and fabricated and even arrayed to meet fiber production demands (139). The highly uniform fibers produced in this work are very versatile for different applications such as air filtering units (268), protective clothing (269), biomedical engineering and many more (270-277).

5.5.1 A microfluidic GDVN for fiber spinning

A GDVN-based microfluidic spinning device was produced with a geometry based on the previously described soft-lithography GDVN designed by Trebbin *et al.* (7). The spinning procedure was easily carried out under non-hazardous conditions at room temperature and atmospheric pressure. A polymer solution in acetone is fed through a liquid inlet which is then accelerated by 3D flow-focusing with compressed air at the nozzle (Fig. 27). The gas envelops and pulls the emergent polymer jet from the nozzle, which rapidly dries to form a continuous fiber. The mechanics of the drying process are discussed in a later section. Such a gas-focusing approach also alleviates the *need* for *external* pulling forces, i.e. from rotational or counter-charged collectors, and therefore allows for the direct solution blow spinning of fibers or micro-/nanofiber deposition onto (non-charged) surfaces.

The original liquid jet-purposed GDVN design (7) was adapted and optimized to one for fiber spinning applications (Fig. 45, B and C). These include changes of the distance from main channel to the nozzle outlet (now 35 µm vs the previous 95 µm) as well as a wider nozzle orifice (55 µm vs 30 µm). The shorter distance between the liquid channel and the nozzle orifice decreases the gas flow-focusing volume and the chances of clogging as the emergent fiber can quickly exit the device. The geometry of the nozzle designed for this work also differs significantly in the gas flow-focusing region compared to that described by Hofmann *et al*. (139). While Hofmann *et al.* described a flow-focusing nozzle geometry in a perpendicular (90°) configuration (Fig. 45A), we chose an incident angle of the gas flow onto the liquid of only 15º (Fig. 45C).We believe that our shallower angle allows for a more forward-directed momentum transfer of the gas accelerating the liquid, resulting in increased flow alignment, smaller fibers and more stable flow focusing conditions (10, 11). This geometry allows us to produce thin endless fibers under a wide range of jetting conditions and without clogging. We were able to effectively and robustly spin THV polymer (a terpolymer of fluorinated tetrafluoroethylene,

hexafluoropropylene and vinylidene fluoride monomers) micro-/nanofibers with highly tunable morphologies which extend beyond the circular and beaded morphologies described by Hofmann *et al*.(139). The stable jetting also allowed for the fabrication of nanocomposite fibers impregnated with spindle-shaped hematite nanoparticles. Due to the flow-induced converging flow rapidly followed by fiber fixation, this anisotropic nanocomposite material was strongly aligned parallel to the fiber axis promising improved fiber mechanics (11), as later shown in Fig. 63.

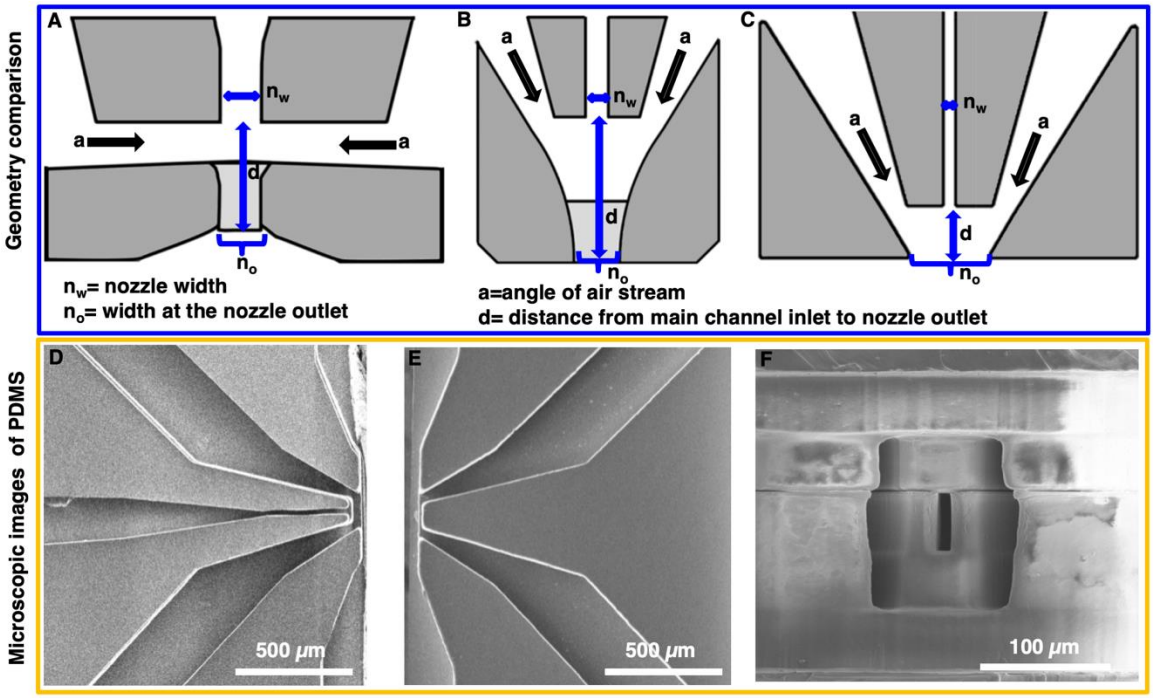

Fig. 45. (*Top*) Comparison of the geometries of previous microfluidic GDVN designs. (A) Microfiber spinning nozzle by Hofmann *et al*. (139); n_w = 30 µm, n_o= 30 µm, a= 90°, d= 80 µm, (B) GDVN for liquid jets by Trebbin *et al*.(35); n_w = 15 µm, n_o= 30 µm, a= 15°, d= 95 µm, (C) Nanofiber spinning nozzle developed for this work; n_w = 15 µm, n_o= 55 µm, a= 15°, d= 35 µm, (*Bottom*) SEM images show the (D) upper and (E) lower PDMS halves (F) SEM image of the asymmetric nozzle outlet.

5.5.2 Influence on fiber diameter

THV fibers of diameters ranging from ~250 nm to ~15 µm were produced. It is a commonly known fact that the fiber diameters can be influenced by the polymer content (final volume after solvent evaporation) as well as the drawing speeds and ratios in a jet-and-spool configuration (139). Since our GDVN did not employ a fiber spooling process, the speed of the emergent fiber is solely determined by the liquid flow rate and pressure-gradient acceleration at the gas flow-focusing region. A wide range of jetting conditions could be employed: 10-25 wt% THV solutions in acetone, 0.5-2 bar of pressurized air (see Fig. 46 for gas flow rates) and 100-3000 µL/h polymer flow rates. The thinner fibers fabricated were ~10x thinner than those previously reported (139). Only a few techniques, such as e.g. solution blow spinning or electrospinning, which however requiring more complex experimental set-ups, have been previously shown to yield such thin, continuous single fibers.

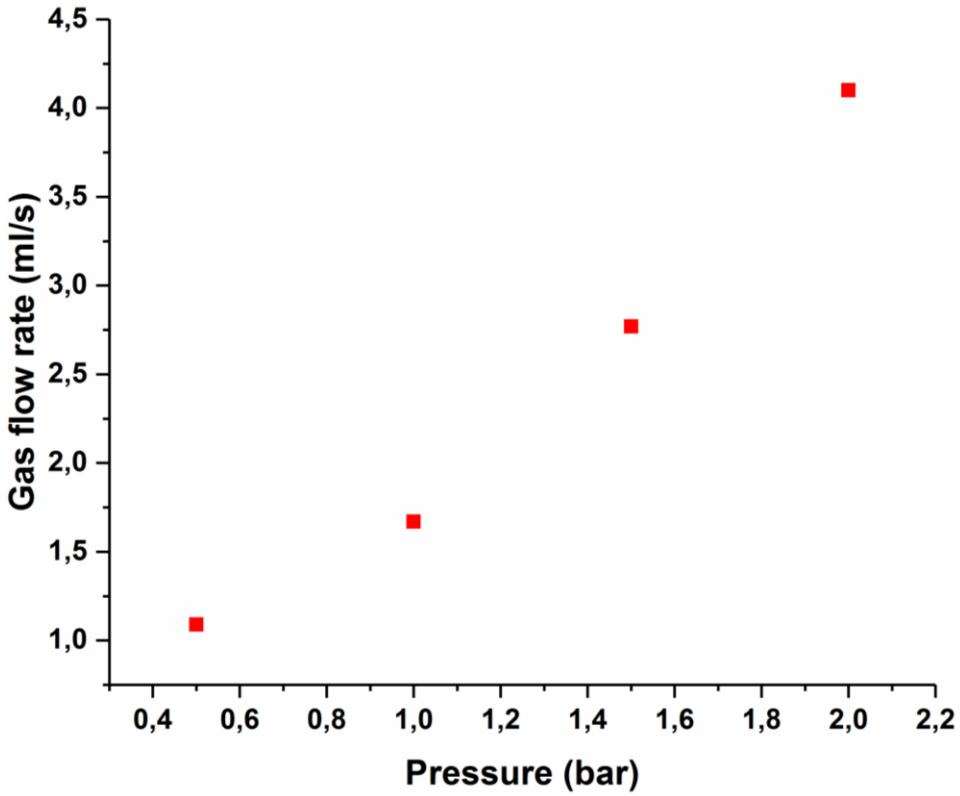

Fig. 46. Change of the gas flow rate as a function of the applied pressure.

A representative sample of different fibers obtained during this study is shown in Fig. 47. The upper and lower limits of the parameter ranges were determined to allow for continuous and smooth fiber fabrication and operation of the devices without clogging or instabilities. At very low polymer concentrations combined with low gas pressures, stable jetting could not be achieved and a dripping mode (followed by clogging from the drying polymer) was observed. For polymer concentrations of more than 25 wt%, the polymer solution was deemed too viscous, as it caused a pressure build-up inside the device which lead to rapid delamination of the nozzles.

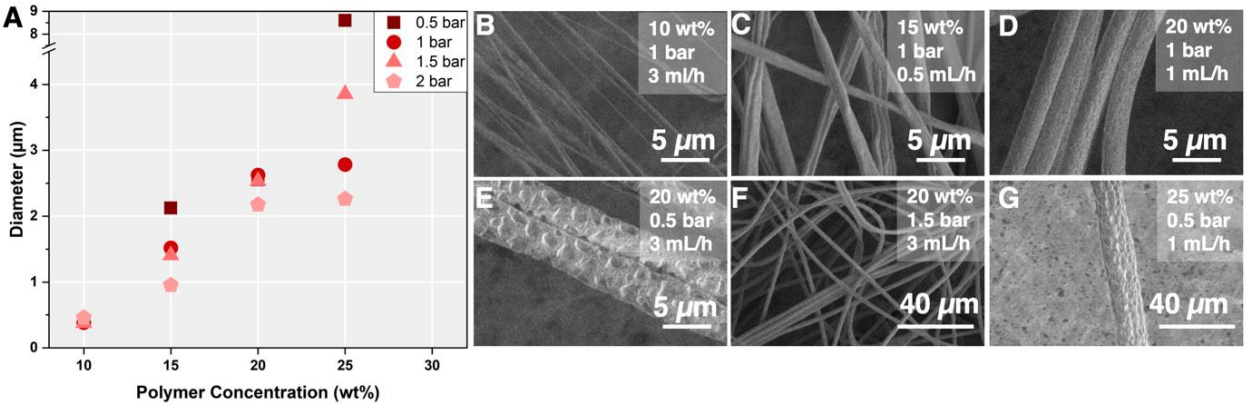

Fig. 47: A) The influences of pressure and polymer concentration are shown, for comparison, at a fixed flow rate of 1000 µL/h. A full data set is presented in Fig. 50 and Fig. 51. B-G) SEM images demonstrating the tunability and uniformity of fiber diameters. The fibers show different shapes and surface morphologies which can be tuned with the polymer concentration and the air pressure.

Furthermore, the handling of these solutions was difficult due to the fast transition from liquid to solid through slightest solvent evaporation (see Fig. 48). A detailed rheological analysis of the spinning solutions can be found in the supplemental information (Fig. 48, 49) (11). Very high air pressures (>2 bar), especially for low polymer concentrations lead to jet breakup and irregularities in the fiber diameter. The fibers did not show conglutination at a collecting distance of 7 cm, confirming that the drying process is extremely fast and the fiber is fully formed within this distance.

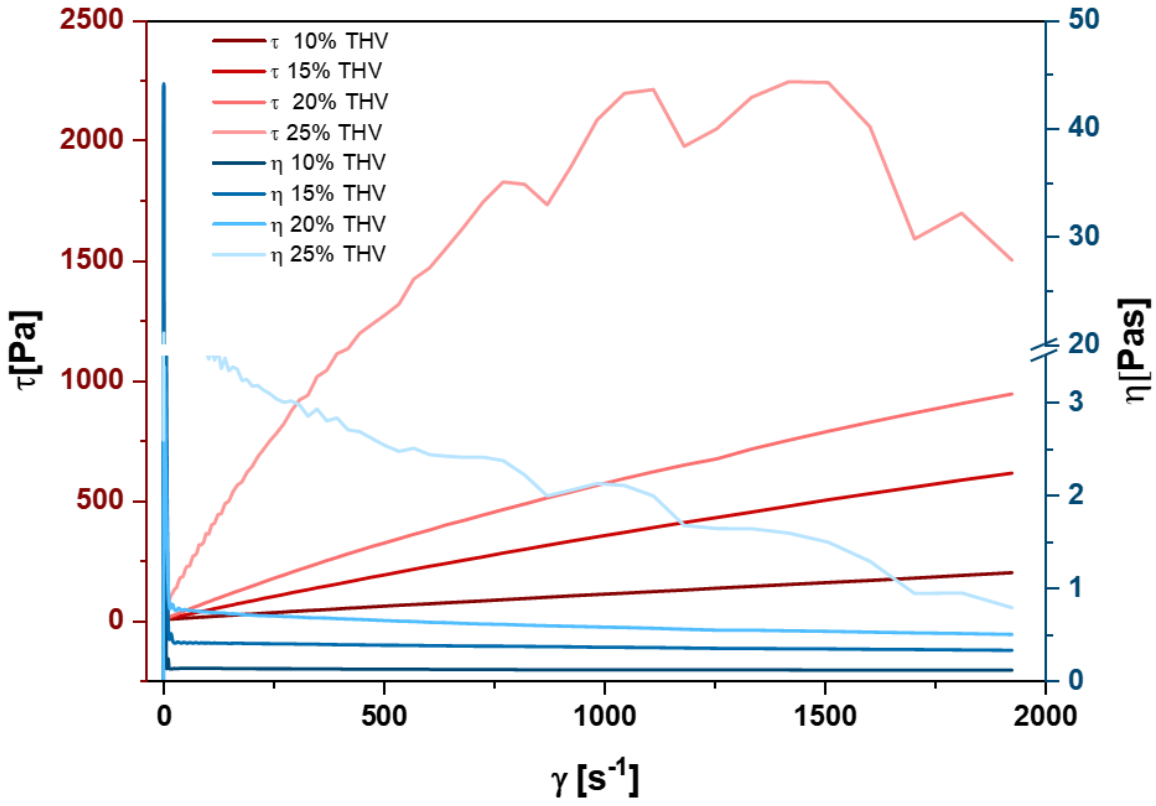

Fig. 48. Rheology data for THV 221 GZ polymer solutions in acetone from 10 wt% to 25 wt%. All concentrations of polymer solutions show a linear trend. The viscosity decreases slightly with an increasing shear rate (shear thinning), except for the highest polymer solution (25 wt%) where the graphs follow the same trend but not in a linear way which might be caused by fast solvent evaporation. Unfortunately, the molecular weight of this commercially-available polymer was not disclosed. Further information considering the material properties can be found with the link: https://multimedia.3m.com/mws/media/688833O/td-thv-221gz-eng.pdf (Accessed April 4th 2019).

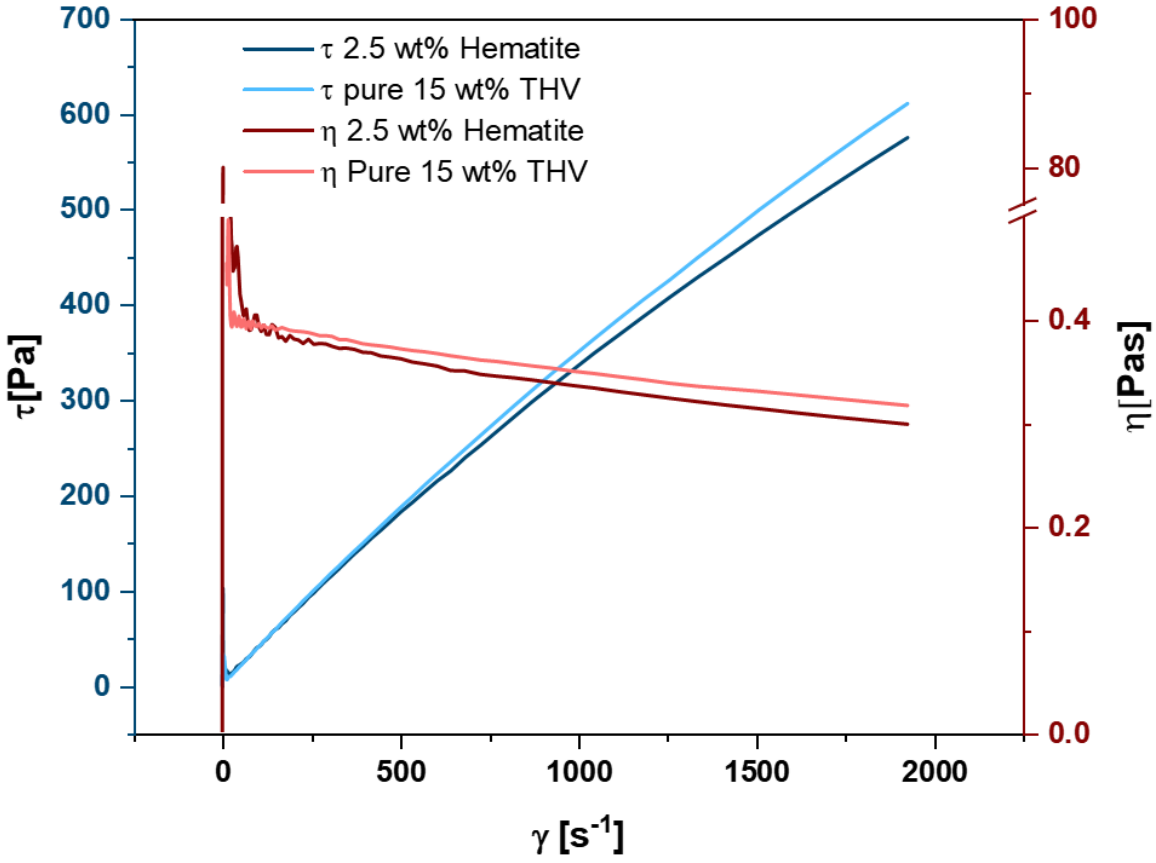

Fig. 49. Rheology data for 15 wt% THV 221 GZ polymer solutions in acetone with (dark colors) and without (bright colors) hematite nanoparticles. These anisotropic particles show only slight influence on the viscosity of the spinning solution. In fact, a small shear thinning effect could be observed - possibly due to the shear alignment in a converging flow. Due to the relatively high viscosity of the polymer solution, sedimentation could not be observed during weeks when the composite solution was stored in a shelf.

Due to the varying mass-flows, the diameters of fibers produced in our device were strongly influenced by the polymer concentration (Fig. 47(A) and Fig. 50). Low polymer concentrations (10 wt%) led to nm-diameter fibers (Fig. 47(B), 51(A)) and high polymer concentrations (25 wt%) to µm-diameter-fibers (Fig. 47(G)), Fig. 51(D), Fig. 50). Two additive effects contribute to this observation. Firstly, the lower initial polymer concentration will lead to a higher volume of acetone evaporation and, therefore, a thinner final fiber.

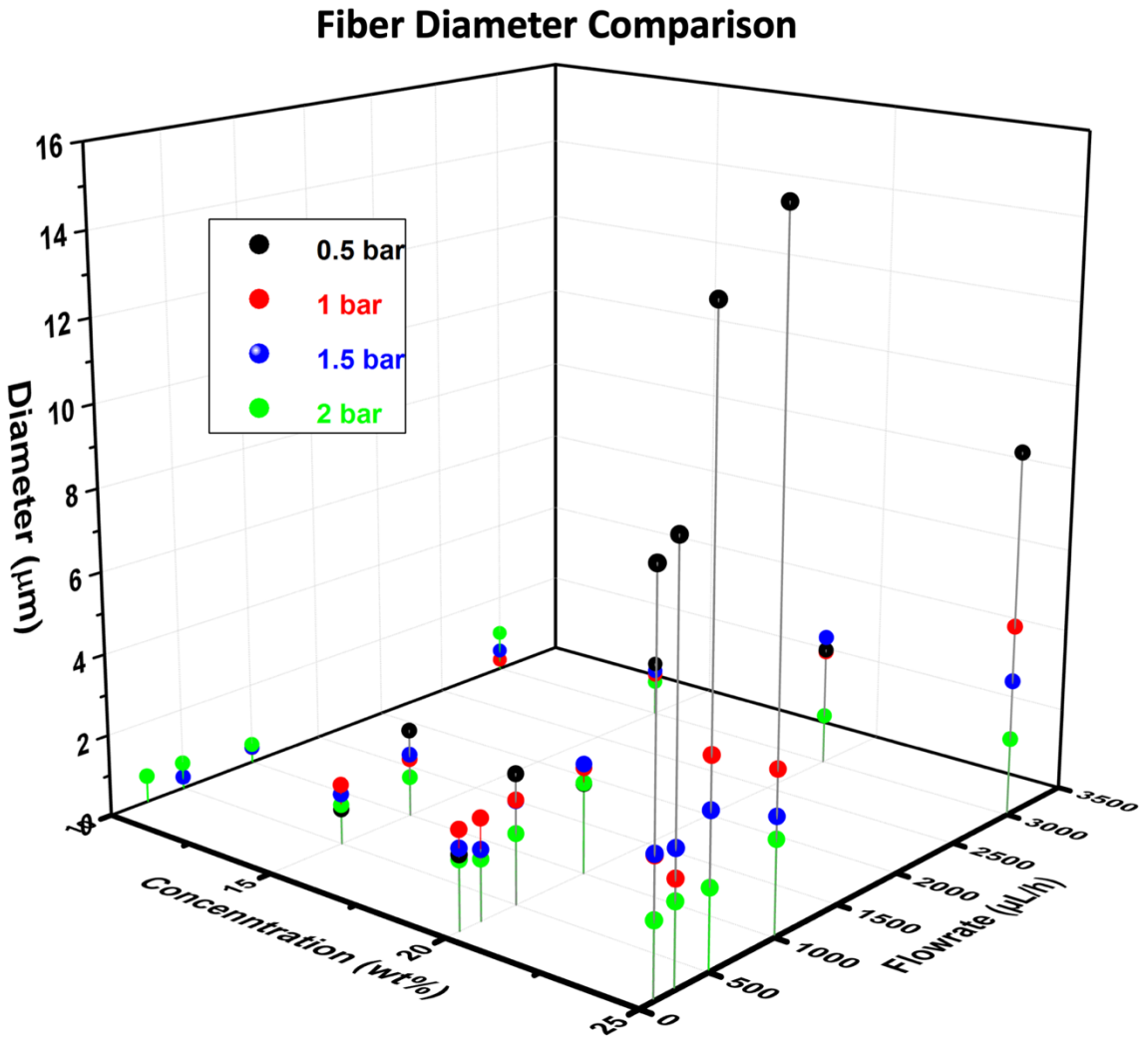

Fig. 50. Diameter measurements of all parameter combinations investigated. Several trends are caused by changes of flow rate, concentration and air pressure are demonstrated here. First, the diameter increases with an increasing polymer concentration (from left to right), especially between the transition from 20 wt% to 25 wt%. Second, with increasing air pressure the fiber diameters decrease (see color coding). Furthermore, the influence of air pressure was greater at higher polymer concentrations. Lastly, the flowrate has only little influence in comparison to polymer concentration and air pressure (from front to back) although it can affect the stability of the flow-focused jet.

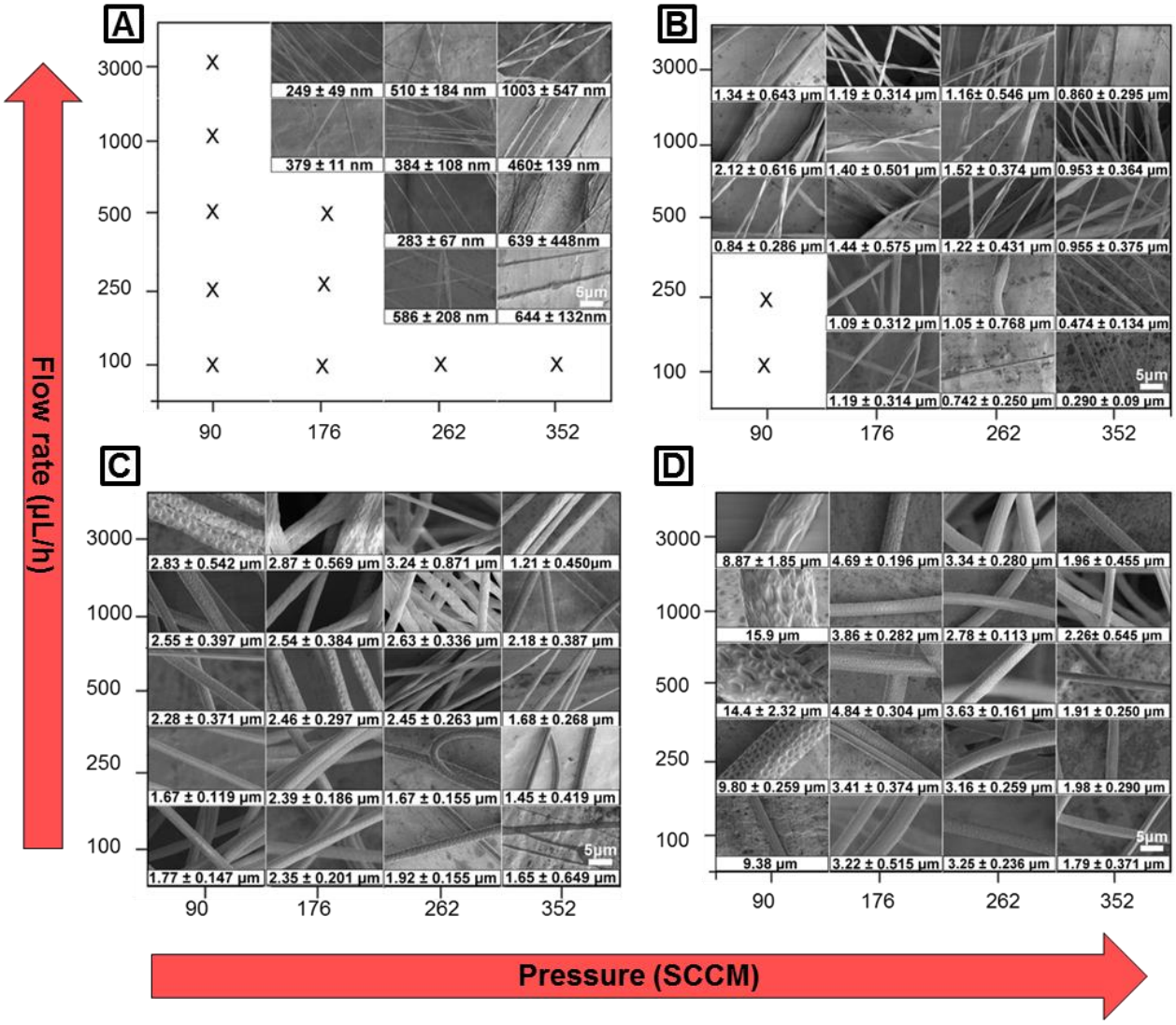

Fig. 51: SEM images of fibers w.r.t flowrate vs pressure at (A) 10% (B) 15% (C) 20% and (D) 25% polymer concentrations.

Secondly, the lower concentration polymer solution has a lower viscosity compared to the high concentration polymer solution and is therefore more easily deformed by the gas flow-focusing. In other words, the fiber diameter depends on the liquid's resistance to stretching (strain resistance) as well as its extensional viscosity and possibly also the elasticity which is present in many polymer solutions. The influence of the polymer concentration and shear on the fluid viscosity was confirmed by rheological data, which can be found in Fig. 48.

The applied air pressure also affects the final fiber diameters obtained. A comparison of fibers obtained from the same polymer solution concentration and liquid flow rate, but at different gas

pressures, shows that the diameters decrease with increasing gas pressure. Fig. 47(A) and Fig. 51(C) shows fibers obtained from 20 wt% THV solution at varying air pressure concentrations. At a constant liquid flow rate of 1 mL/h, the fiber size decreases from 2.55 µm to 2.18 µm (applied pressure 0.5 bar and 2 bar respectively) with the air pressure increase. This effect is even more dramatic at higher flow rates, with the size of the fibers varying between 2.83 µm and 1.21 µm. The smaller jet has less mass and can therefore be accelerated by the gas to faster velocities which results in a stronger extensional flow and thinner fibers emerging from the nozzle. This behavior has also been described for liquid jets generated in GDVNs (198) and is in line with the behavior described by Hofmann *et al.*(139).

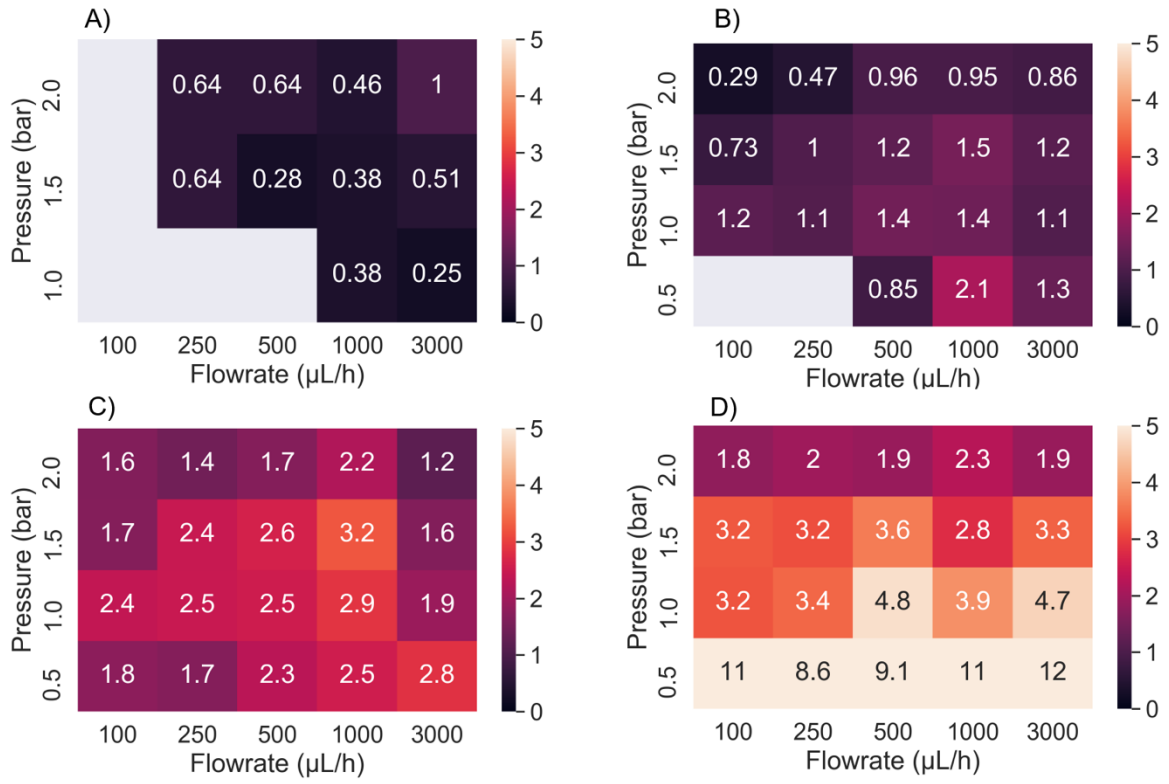

Fig. 52. Heatmap of the fiber diameters (values in µm) for 10 wt% - 25 wt% polymer solution A) - D). The map clearly shows that the diameter increases with increasing concentration and decreases with increasing pressure. The chosen colorscale robustly represents 90% of the data, with the exception of the largest fibers (25% polymer, 0.5 bar) which are outside of the scale.

In summary, fiber diameters increase with increasing polymer concentrations and with decreasing gas flow rates. An overview heat map highlighting of these trends can be found in Fig. 52.

Especially for the larger diameters (20-25% polymer solutions), the fiber diameters showed low relative standard deviations (Fig. 53, 54), showing that the controlled fabrication allows for high monodispersity of the sample. For lower polymer concentrations, these deviations were inflated, which is a repercussion of both the change in morphology (from round to flat fibers) as well as increased errors in the fiber diameter measurements arising from limitations in image resolution.

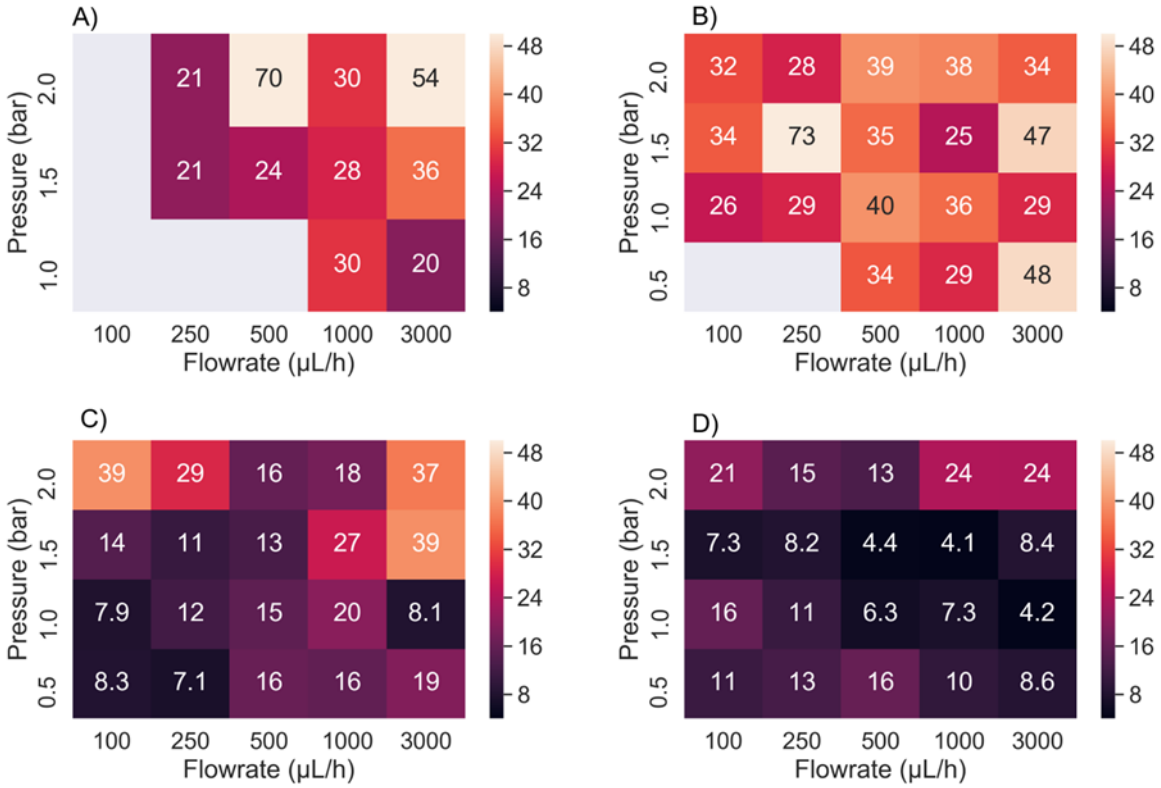

Fig. 53. Heatmap of the relative standard deviation of the fiber diameters (values in %) for concentrations of 10 wt%-25 wt% polymer solutions A) - D). The relative standard deviation is much bigger for flat fibers, which arises from their nonuniformity. The chosen color scale robustly represents 95% of the data, with the exception of the 3 largest values which are outside of the scale.

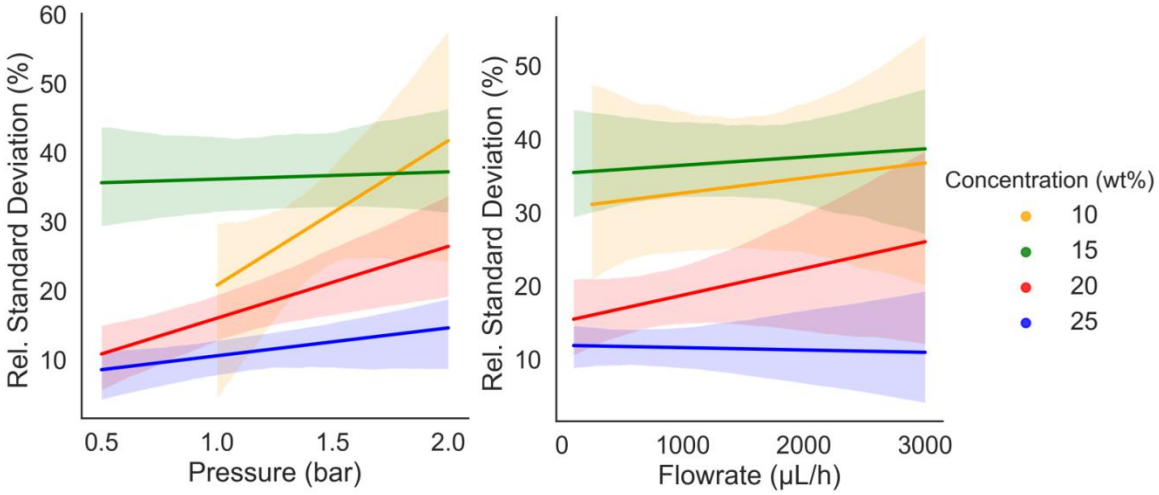

Fig. 54. Comparison of standard deviation for all measured fibers. First, the relative standard deviation (stdv%) drops with higher polymer concentrations, especially between 15 wt% and 20 wt%, where a large decrease can be found. This is probably due to the geometrical transition from flat to more uniform round fibers. Furthermore, by increasing the pressure, the stdv% is also increased, a trend that was can be also seen with respect to the flowrate, which was reportedly previously**.** Although, the variance increased at higher flowrates.

5.5.3 Fiber shape and characteristics

The polymer concentration and the air pressure do not only affect the diameter of the fibers but also the fibers' overall shape and surface features. The fabricated fibers could be divided into five distinct classes according to their shape and surface morphology as shown in Fig. 55: flat-rough (A), flat-smooth (B), round-rough (C), round-grooved (D) and round-smooth (E). Fig. 55 also shows how the classification is correlated with polymer concentration and gas focusing pressure used during fiber spinning. No beaded fibers, i.e. fibers with oscillating diameters along their length, were observed during our experiments, indicating a smooth and constant fiber formation process with rapid drying of the emergent fiber.

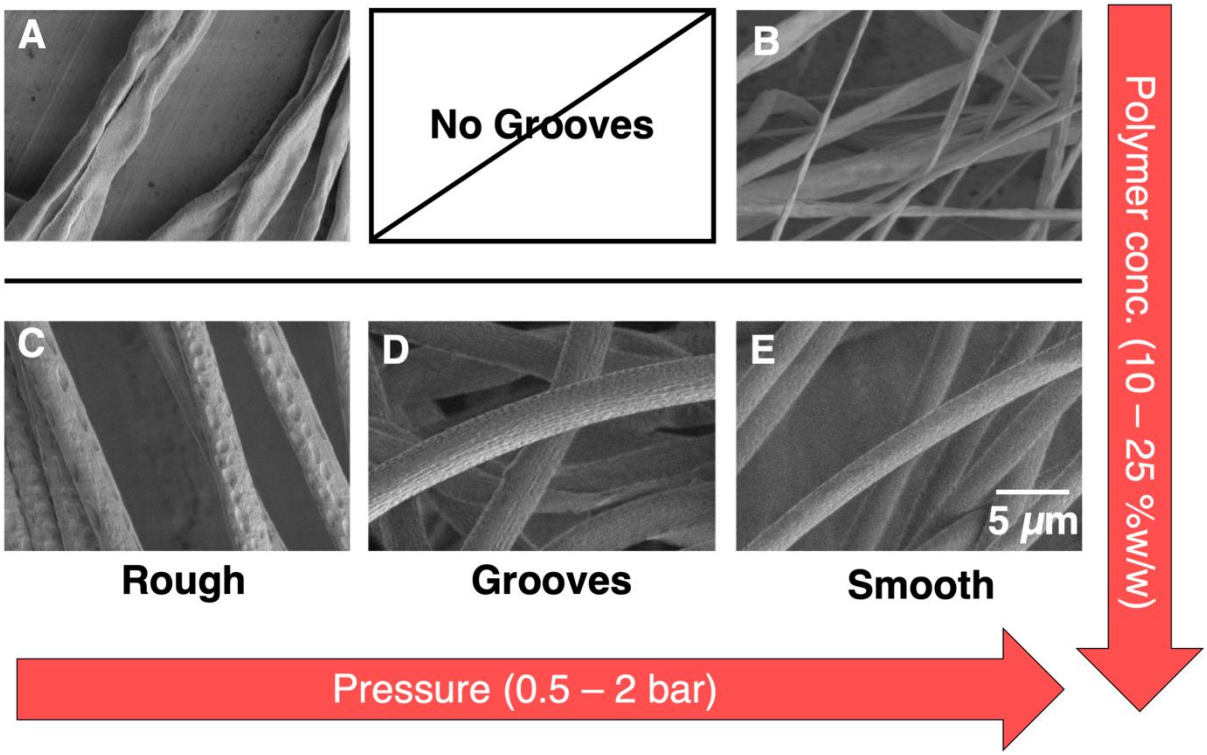

Fig. 55: Table of the different fiber classes with representative SEM images. The fibers were categorized into flat (A and B, 10 wt% - 15 wt%) or round (C-E, 20 wt% - 25 wt%). Flat fibers were either rough or smooth (A and B respectively). Round fibers were rough, grooved, or smooth (C, D and E respectively). The shape was influenced by the polymer concentration and the surface roughness was controlled by the air pressure.

The overall shape of the fiber could be flat or round and was controlled by the polymer concentration. Lower polymer concentrations of 10-15 wt% produced flat fibers (Fig. 55(A,B), Fig 51(A,B)), whereas round fibers were obtained from 20 wt% and 25 wt% polymer solutions (Fig. 55(C-D), Fig. 51(C,D)). Flattening of the fibers was caused by the device's rectangular geometry and the asymmetric pressure profile at the gas-focusing region. The liquid flow channel is rectangular (15 μm × 40 μm w×h) and so is the nozzle opening (55×120 μm w×h, Fig. 45(F)). The gas channel envelops the liquid in three-dimensions but due to the nozzle dimensions, the liquid will experience higher compression forces in the horizontal direction which, in the case of the low concentration/low viscosity polymer solution, will dictate the asymmetry of the final fiber. An increase of this aspect ratio would potentially allow for the fabrication of flat, ribbon-like fibers with a high surface-to-volume ratios. This anisotropy effect is much less pronounced at higher polymer concentrations due to the higher viscosity and surface energy of the liquid

resulting in circular fibers. Based on these observations we assume that a round (or square) nozzle geometry would be beneficial for the generation of round fibers.

The produced fibers can be further classified by their surface morphology, as shown in Fig. 55. The most pronounced surface characteristics (e.g. craters and grooves) were found at high polymer concentrations, especially with the 25 wt% polymer solution. Fig. 56 and Fig. 51 show the morphology obtained from the selected combinations of flow rate, focusing gas pressure and polymer solution concentration.

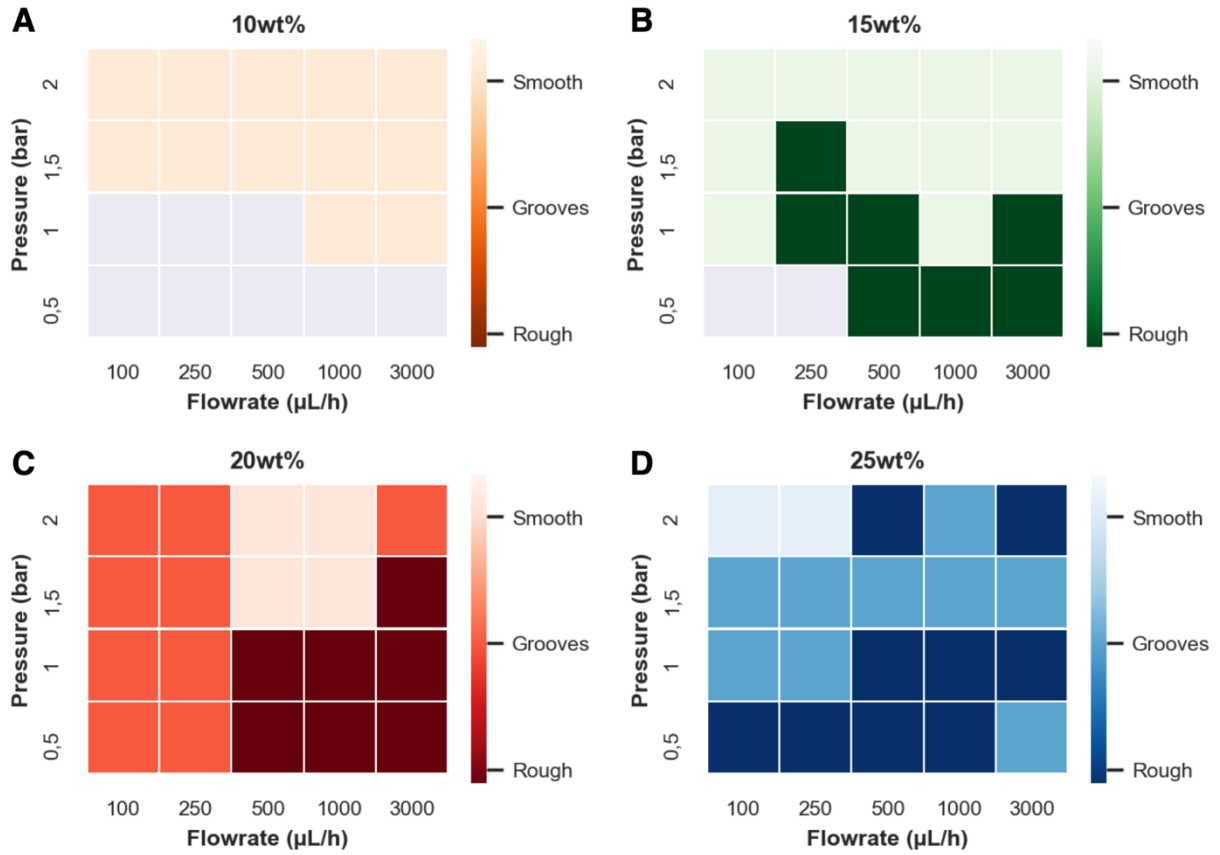

Fig. 56: Fiber surface characteristics are influenced by the polymer solution concentration, flow rate and focusing gas pressure. A) 10 wt% yields flat, smooth fibers. B) 15 wt% polymer solutions lead to smooth and rough flat fibers with decreasing pressure. C) 20 wt% and D) 25 wt% lead to smooth, grooved or rough fibers, with decreasing air pressure. The detailed surface characteristics - smooth, grooved, and rough - are shown by the different color brightnesses. The corresponding SEM images and diameters can be found in the supplemental information (Fig. 51A-D). Grey areas in A) and B display the “no jetting state“.

At the lowest concentration of 10 wt%, mainly smooth and flat fibers were observed (Fig. 56(A), Fig. 51(A)). By increasing the polymer concentration to 15 wt% the flat fibers could be distinguished into flat-rough and flat-smooth fibers (Fig. 56(B), Fig. 51(B)). The flat-rough fibers formed at low pressures (0.5-1 bar) and showed small craters in the nm-range. At higher pressures (1.5-2 bar), the fibers showed only smooth surfaces. At high polymer concentrations of 20 wt% and 25 wt% fibers were classified into round-rough, round-grooved, and round-smooth, representing different levels of surface craters. The data suggests that the appearance of the different surface morphologies depends on the interplay between the time scales of the solvent evaporation process at the surface and the velocity mismatch mechanism between the liquid jet and the air stream. The shear exerted on the surface of the liquid is coupled to the difference in speeds between the gas and the liquid surface. This shear is strongest in the converging flow-focusing region where the fast air flow accelerates the liquid. Our experiments show that round craters on the fibers' surface have a higher tendency to be observed at lower pressures (e.g. 0.5 bar) as shown in Fig. 55(C), Fig. 56(C,D), Fig. 51(C,D). The appearance of similar craters has also been previously observed in fibers fabricated by electrospinning (278). In electrospinning, surface porosity is achieved by a fast evaporating solvent in the absence of an air stream and inducing phase separation during solvent evaporation, which divides the matrix into polymer-rich and polymer-poor regions as discussed further below (279). At higher air pressures the fiber is stretched and grooves develop which are especially well expressed for the fibers spun with the 25 wt% polymer solution (Fig. 51 (D)). At the highest pressure, the surface patterns can fully vanish resulting in a smooth surface (Fig. 56). Therefore, we believe that surface the properties are mostly determined by the air pressure, or more precisely by the velocity of the air stream surpassing the liquid jet combined with a fast evaporating solvent. Interestingly, higher liquid flow rates led to an increase of surface roughness, but the mechanism for this is still unclear and needs further investigation.

The distinction between the different surface morphologies was done by evaluating SEM images of the fibers and is only a guide to the expected surface morphology vs. different experimental conditions. Of course, the change in morphology is continuous over the different experimental conditions and may vary especially in transition regions during the device operation. Further deviations from the expected morphology might be caused by changes in the environment (temperature or humidity).

5.5.4 Inner morphology and porosity of fiber

The production of porous or micro-/nanofibers is of high interest for reducing their weight and increasing their surface to volume ratio. For example, such porous or grooved fibers can be obtained by electrospinning and controlling the polymer/solvent/anti-solvent interaction (280, 281). The underlying mechanism of such processes relies on the formation of pores upon the evaporation from the polymer-poor phase and solidification of the polymer-rich phase, which is also reflected by the phase diagrams of such ternary phases (280, 281). To investigate the inner structure of the here-produced fibers, focused ion beam (FIB) (282) cuts were performed and revealed that the polymer concentration has indeed an impact on the fibers' internal porosity. Fibers manufactured from polymer concentrations of 10 to 25 wt% at the same flow rate and pressure (3 mL/h, 2 bar) were investigated as shown in Fig. 57.

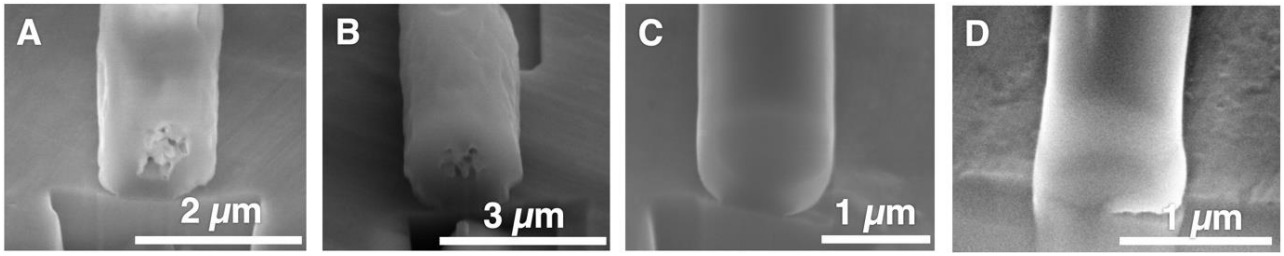

Fig. 57: SEM images of THV fibers dissected with FIB showing the cross section of fibers produced at 2 bar, 3000 µL/h. (A) 10 wt% THV, porous, 1.2 µm diameter, (B) 15 wt% THV, porous, 1.6 µm diameter, (C) 20 wt% THV, solid, 1.05 µm diameter, and (D) 25 wt% THV, solid, 0.9 µm diameter.

Fibers spun with 10 and 15 wt% polymer solution showed core porosity (Fig. 57(A,B)) while the fibers spun from the 20 and 25 wt% polymer solution were completely solid (Fig. 57(C,D)). This observation is in agreement with recent literature (280, 281). At polymer concentrations ≤ 15 wt%, a larger volume fraction of solvent has to evaporate first before the fiber can solidify which in turn increases the drying time. It can also be assumed that the outside layer at the air interface dries first, while this initial layer could even slow the solvent evaporation from the fiber core even further. This combination gives the material enough time and mobility to separate into polymer rich and polymer poor phases, which represents a thermodynamically favored state. Fibers with and without inner pores have different physical properties. Inner porosity is desirable for fibers manufactured for biomedical applications (cell-laden fibers) (283) or for fibers with

increase thermal insulation properties while solid fibers can serve as materials for non-woven tissues or high-performance clothing. The possibility of tuning these properties as easily as changing the polymer concentration by 5 wt% allows access to these different applications as well as the possibility of making layered materials.

5.5.5 Fiber spinning mechanics

Based on the experimental results obtained by SEM images and high speed video microscopy, a phenomenological hypothesis of the fiber spinning mechanics is suggested. This hypothesis divides the spinning process into three different regions as shown in Fig. 58: (1) the gas focusing region, (2) the jetting regime and (3) the thinning regime. The gas focusing region was located inside the microfluidic device where the main and side channels intersect. The expelled liquid is flow-focused by the bypassing air stream and a solution cone geometry can be observed (284). In this step, the jet diameter thins due to the hydrodynamic gas-focusing which is also the key step for the flow alignment of anisotropic particles. Subsequently, the liquid is ejected at the nozzle orifice as a straight jet entering the jetting regime, as seen from the very small oscillation of the emergent jet. This stable jetting behavior at 3 mL/h and 2 bar (20 wt% polymer solution) was roughly 1 cm. The length of this region depends on jet and air stream velocity as well as the viscosity of the solution. Within this region, the jet diameter is almost constant and only thinned by the loss of solvent due to evaporation. The end of the jetting regime is marked by the appearance of chaotic low-amplitude fluctuations which increase dramatically with the jetting distance and develop into a turbulent flow profile, causing the fiber to become thinner (thinning regime, 3). The turbulent behavior is characterized by the whipping of the fiber, as shown by the sudden increase of its oscillation amplitude. This behavior is caused by an increase of the Reynolds number (Re) and by Raleigh instabilities arising from the surface tension of the solvent. Even though the jet diameter is decreased within the hydrodynamic focusing region (1), the main fiber thinning process - especially for nanofibers at low polymer concentrations - seems to occur during the last stage due to the additional whipping or spiraling movement induced by the turbulent air flow. This behavior can stretch and thin the semi-solid fiber as it was observed by Benavides *et al.* where a comparable method was used (280).

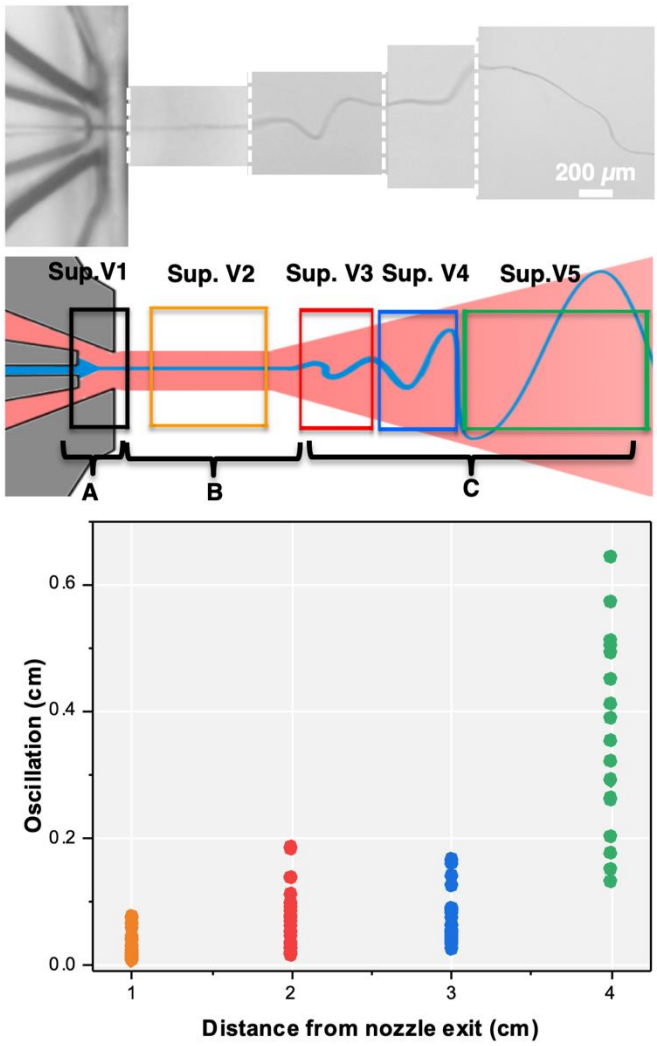

Fig. 58: Schematic view of fiber formation process using GDVN devices with (*top*) high speed video microscopy snapshots. The white dotted lines indicate different highspeed video recordings. (*middle*) An illustration of the hypothesis. The spinning process was separated into three sections, (A) gas focusing region, (B) jetting regime, and (C) thinning regime. (*bottom*) The plot shows the oscillation amplitude of the emerging fiber during jetting perpendicular to the jetting axis.

5.6 Nanocomposite fibers

3 mL of a 30 wt% polymer solution of THV 221 GZ in acetone was stirred overnight. Shortly before preparing the spinning solution, the Fe_2O_3 hematite nanoparticles (650×65 nm, L×D, Fig.59 (A)) (285) were dispersed in 1 mL of acetone in a tall and thin 2.5 mL vial. The dispersion was then homogenized with a sonotrode and mixed in a 1:1 v/v ratio with the 30 wt% THV 221 GZ polymer/acetone solution to obtain a final 15 wt% polymer solution with a 2.5 wt% concentration of nanoparticles. Due to the relatively high viscosity of the polymer solution, sedimentation could not be observed during weeks when the composite solution was stored in a shelf.

The used CNTs were produced via Chemical Vapor Deposition (CVD), a horizontal tube furnace HZS (Carbolite Gero) with three heating zones, Fig.53 (B)), as published (286) before with collaboration from Mr. Alexander Hass, Hamburg University of Technology-TUHH. The carbon nanotubes (CNTs, 20 µm x 75 nm, LxD) dispersion process is same as for hematite.

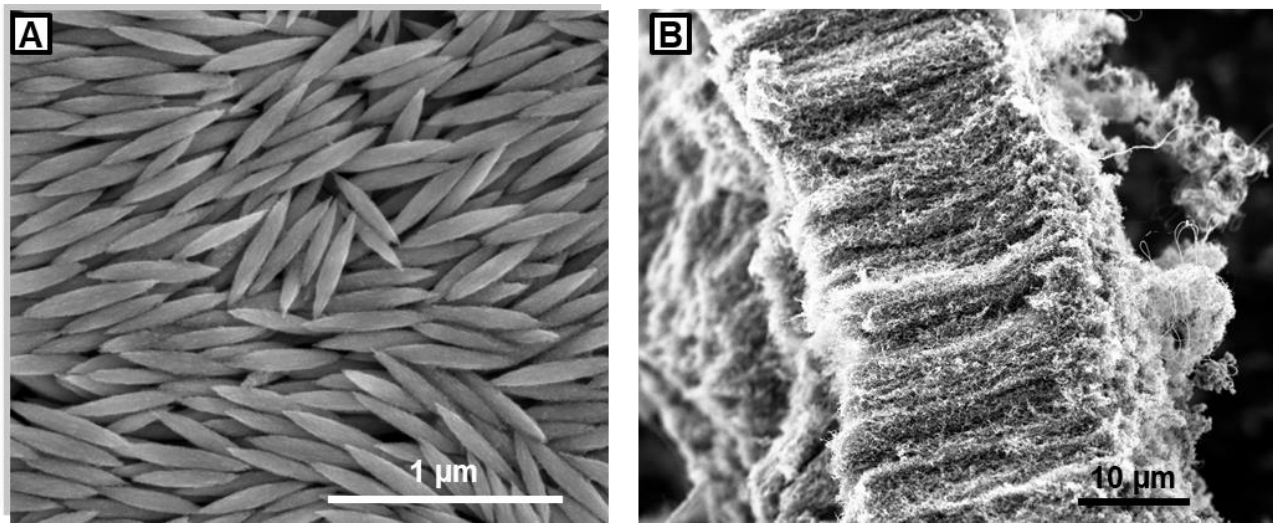

Fig. 59: SEM micrographs of (A) hematite spindle-shaped nanoparticles and (B) carbon nanotubes.

5.6.1 Hematite nanocomposite fibers

To demonstrate the versatility of this fiber manufacturing process, fibers impregnated with anisotropic hematite nanoparticles were also fabricated. 15% THV solutions with dispersed 650×65 (LxD) nm magnetic hematite nanoparticles (from 0.1 wt% to 10 wt%) could be easily jetted under similar conditions as described before (1 mL/h and 262 SCCM). SEM images of the hematite composite fibers are shown in Fig.60.

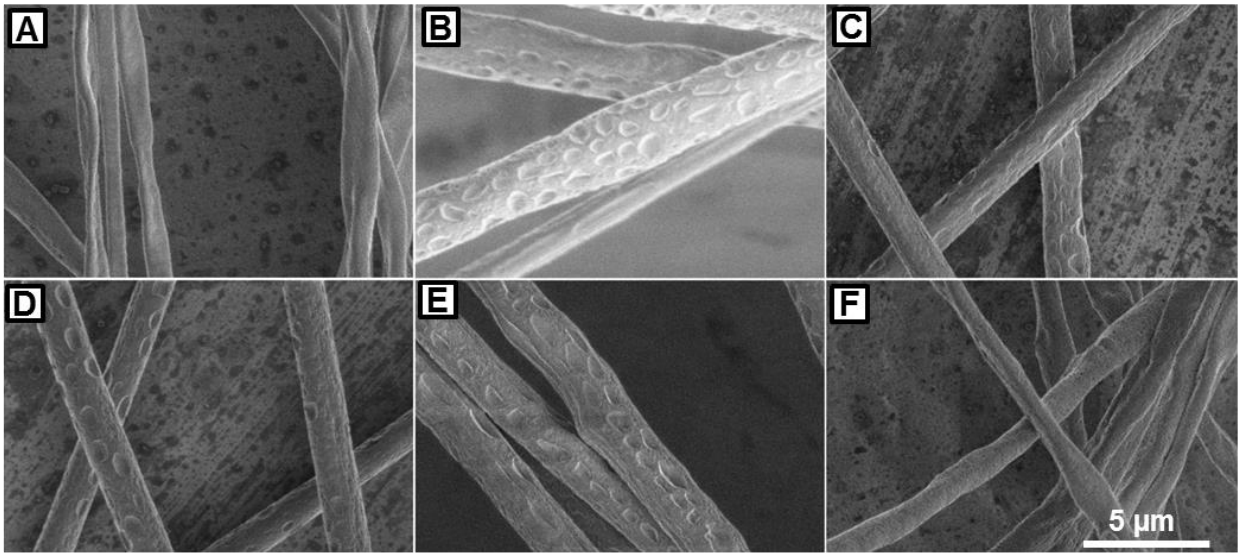

Fig. 60: SEM images of the hematite nanocomposite fibers. A) Pure THV, B) 0.1 wt% Hem, C) 1 wt% Hem, D) 2.5 wt% Hem, E) 5 wt% Hem, F) 10 wt% Hem.

The jetting behavior was smooth and continuous, suffering from no visible influences due to the presence of the nanoparticles. Contrary to the flat-smooth fiber expected under these conditions, the nanocomposite fibers were round and showing craters on the surface, indicating an influence on the surface morphology and overall fiber shape from the presence of the nanoparticles. Additionally, these fibers had a rough surface with slightly elongated craters on the surface in the sub-µm range.

Here, performed rheology experiments, to investigate the viscosity effects on surface roughness and diameter, the resulting data are shown in Fig.61. The graph shows that a small shear thinning effect, possibly due to the shear alignment in a converging flow (38). All concentrations showed

a sharp peak at the very beginning, which rises and falls quickly, which can be explained by the molecules and particles changing from a non-ordered state into an ordered one. Once this force is overcome, the curve shows behaviour that is proportional to viscosity. So friction is lowered due to aligned particles along the movement direction. All concentrations of polymer solutions show a linear trend. The viscosity decreases slightly with an increasing shear rate, except for the highest polymer solution (25 wt%), where the graphs follow the same trend but not in a linear way. This effect is called shear thinning and it is typical for polymer solutions and was described by Graessley (287).

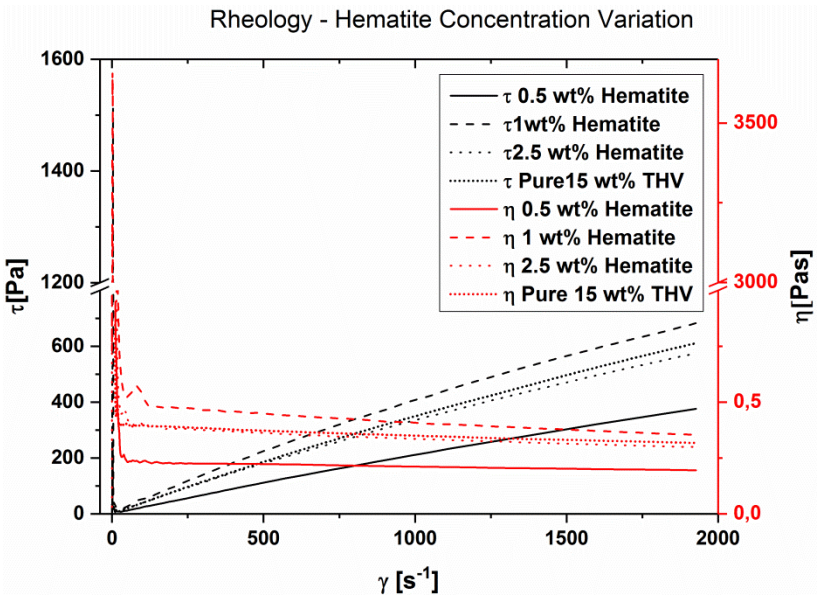

Fig. 61: Rheology data for the pure polymer and hematite ratios up to 2.5 wt%. The viscosity stagnates and does not change with higher amounts of nanoparticles, except at the very beginning, a tremendous rise and fall of the viscosity can be observed. With increasing shear rate, the solution shows a shear-thinning effect.

Polymer solutions or polymer melts with a molecular weight higher than the critical molecular weight can form entanglements. When no force is acting on the polymer solution, equilibrium settles of entanglements and disentanglements, which leads to a constant density of entanglements. By increasing the shear rate, the equilibrium is pushed to the side of disentanglements because the time to form new entanglements is too long (chain stretching and

relaxation time). Less entanglement leads to a decrease in friction consequently, resulting in shear-thinning.

Solutions containing up to 2.5 wt% hematite nanoparticles were analyzed, as shown in Fig.61. All graphs, including the reference sample with no hematite particles, showed a strong peak at the very beginning, which afterward decreased to a viscosity between 0.2 Pa.s and 0.5 Pa.s. From this point, the graph showed a linear behavior with a slightly decreasing viscosity at higher shear rates. The peak at the very beginning was more intense; the higher the amount of hematite particles inside the sample.

To verify the quality of the distribution of the hematite particles inside the fiber, a SEM analysis of the three types of wt% samples was carried out (Fig.62). The images show that high concentrations of particles agglomerate into large bundles. These bundles seem to float to the fiber surface, but individual hematite particles still seem to be distributed inside the fiber, where they show alignment along the fiber direction (Fig.62 (B). The images suggest that the agglomerates might migrate to the surface during the drying process due to phase separation. The data shows that a homogenous dispersion was not wholly achieved at high hematite volume fractions and that most of the particles agglomerated (Fig.62 (C). This observation results from unfavorable interactions between the hydrophobic, fluorinated fiber and the hydrophilic phosphate ions on the surface of the particles. The schematic representation of the experimental setup and corresponding SEM image of 2.5 wt% hematite-loaded microfiber is shown in Fig. 63.

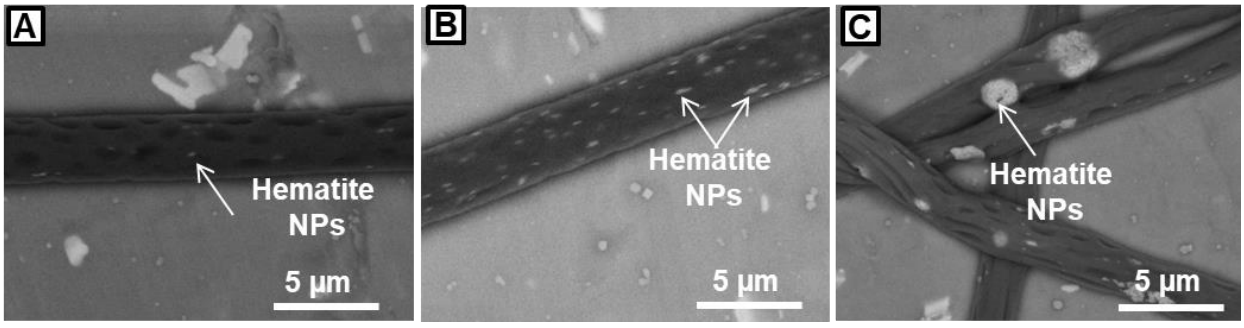

Fig. 62: SEM images of (A) 0.1 wt% Hem, (B) 2.5 wt% Hem, (C) 10 wt% hematite nanocomposite fibers.

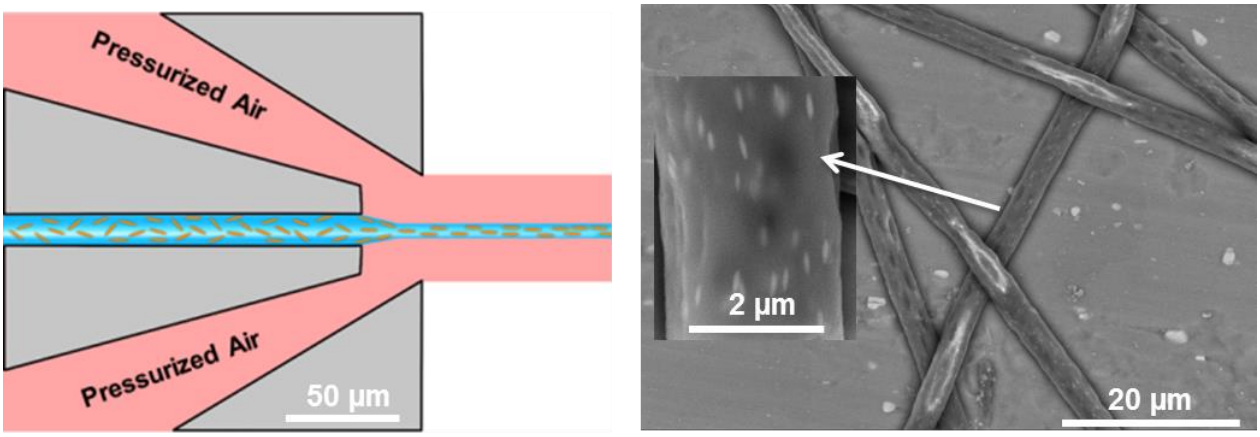

Fig. 63: (*Left*) Schematic view of the experimental microfluidic gas-dynamic fiber spinning setup where the extensional flow along the fiber axis fosters parallel particle alignment. (*Right*) The corresponding element-sensitive backscattered electron (BSE)-SEM image of 2.5 wt% hematite-loaded microfibers shows the parallel alignment of well-dispersed anisotropic nanoparticles along the fiber axis.

SEM images showed a uniform distribution of the particles inside the fiber (Fig. 63). Very interestingly, the particles were strongly aligned longitudinally along the jetting direction, as shown in previous aqueous circular jets (288). This strong alignment can be explained by the strong extensional flow field in the converging flow focusing region followed by a rapid solidification of the polymer. Due to this rapid fixation, any rotational diffusion of diverging flow is stopped which would otherwise influence the order parameter of these anisotropic particles (38,39).

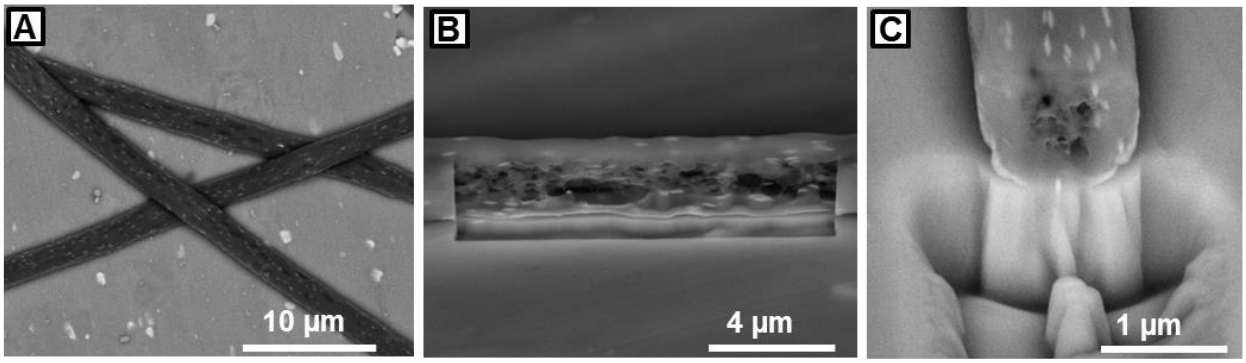

Fig. 64: FIB-SEM images of 2.5 wt% hematite-nanocomposite fibers showing particle alignment and porosity inside the fiber.

To investigate the inside of the nanocomposites, fibers containing 2.5 wt% hematite nanoparticles were analysed using FIB-SEM, as shown in Fig.64. Particles are aligned along the flow direction, as mentioned above, but there is porosity inside the fibre. This porosity could stem from (1) particle interaction with polymer solution due to interfacial effects leading to phase separation and/or (2) be a consequence of the large viscosity at the outer surface as it dries faster than the inner surface during fast solvent evaporation trapping aligned particles/and giving the polymers and solvent more time to microphase-separate.

Such nanocomposite fibers could find wide range of biomedical applications, for example in diagnostics (contrast agent), hyperthermia agent, drug delivery, or tissue engineering (10). Furthermore, applications as micro-/nanofibers from stimuli-responsive materials to magnetic fields are also possible.

5.6.2 CNT nanocomposite fibers

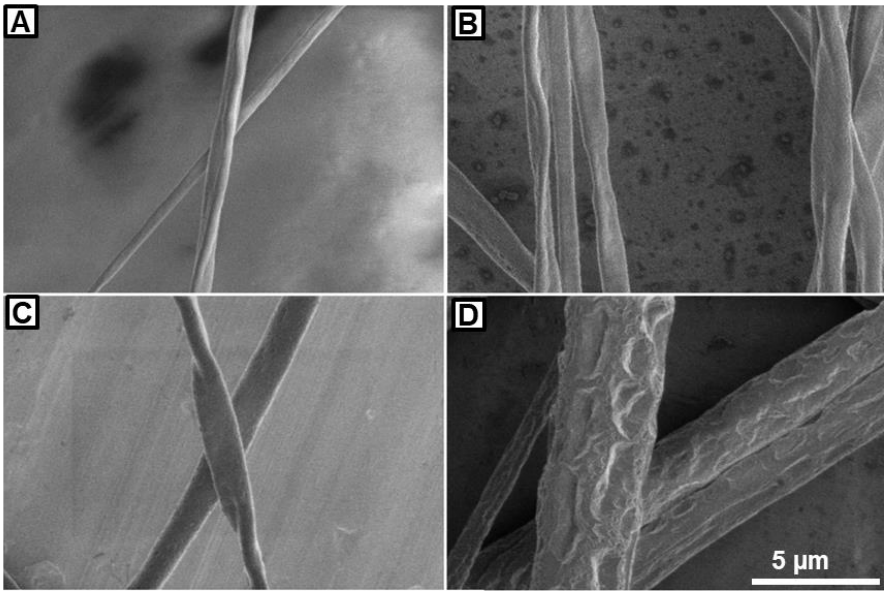

Fig. 65: SEM images of CNT nanocomposite fibers. The figure shows pure polymer fibers (THV 221 GZ) (A), with 0.1 wt% CNT fibers (B), with 0.5 wt% CNT fibers (C) and with 1 wt% CNT fibers (D). All fibers were flat except for 1 wt% CNT and the nanotube network is covered with polymer so it is difficult to image the CNTs, more details will see in below (FIB-SEM).

Three different ratios of CNT nanocomposite fibers were fabricated containing 0.1 wt% to 1 wt% CNT. The used CNTs can be seen in Fig.59. They had a mean length of 25.6 µm and a mean width of 75 nm (aspect ratio: 341). SEM images of the different ratios of CNT nanocomposite fibers are shown in Fig.65. Only 1 wt% CNT sample showed round fibers. Additionally, these fibers showed high surface roughness with elongated craters along the jetting direction that probably from the ligand- and gas-flow settings as discussed in chapter. For the 0.1 wt%, CNT and the 0.5 wt% CNT samples fibers with a flat shape were observed, same as for the pure THV 221 GZ sample. No surface roughness was observed. Previous research work on the influence of CNTs on the viscosity of fluids showed that the viscosity decreases for volume fractions below 0.4 %, due to the lubricative effect of nanoparticles [286, 289]. Considering this, at a critical threshold of CNTs between > 0.5 wt% and ≤ 1 wt% round fibers are the consequence. This could be induced by the CNTs, which could affect the jetting behavior at a certain critical CNT concentration and cause a more unstable jet or CNTs being longer than the channel width and therefore they can get stuck inside the channel and accumulate.

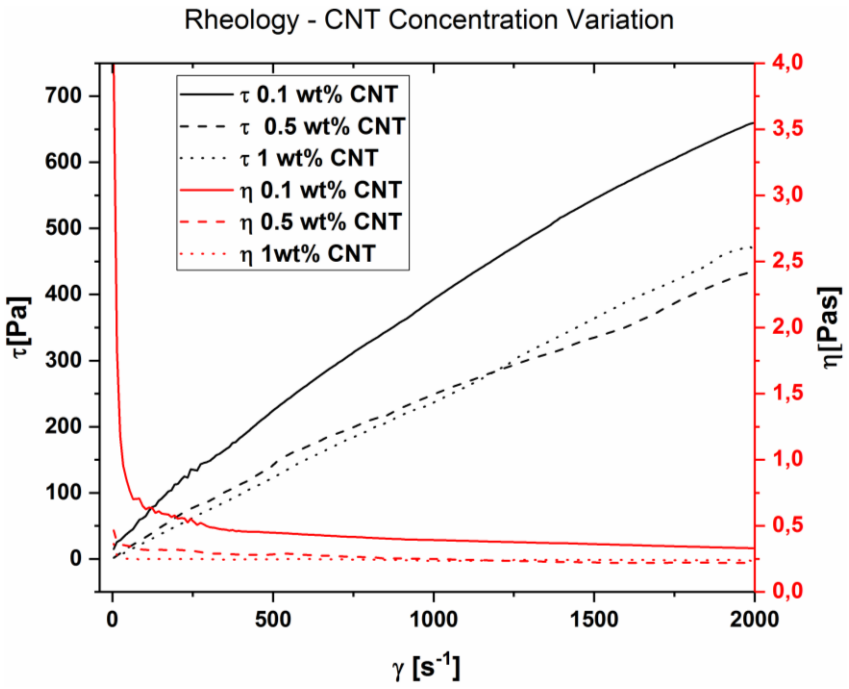

Fig. 66: Rheology graph of CNT nanocomposite.

To verify the influence of CNTs on the viscosity, rheological experiments were carried out, as shown in Fig.66. The results showed that the viscosity did not increase and the fluid showed shear thinning. The 0.1 wt% solution showed a strong peak at the very beginning, which could not be observed for the other samples. This effect could stem from an initial adhesion force between dried polymer on the edges and the plate. The non-Newtonian shear-thinning effect had been observed previously for MWCNTs in various nanofluids [290]. Nevertheless, rheological properties are highly dependent on the CNTs, fluid characteristics and the fabrication process. The 0.1 wt% solution shows a slightly higher viscosity than its higher homologues, due to the fast evaporation of acetone during the experiment. The processing of the solutions could explain these differences since they were used to spin nanocomposite fibers before they were used for the rheological experiments. During the handling of the solutions, the volatile acetone may have been evaporated and led to a more viscous solution.

To investigate the structure inside the fiber nanocomposites, fibers containing 1 wt% CNTs were analyzed, as shown in Fig.67. The FIB-SEM images show that excess concentration of CNTs leads to clusters/agglomerates. The increased viscosities of polymer solution further enhanced the problem of non-uniform dispersion of the CNTs.

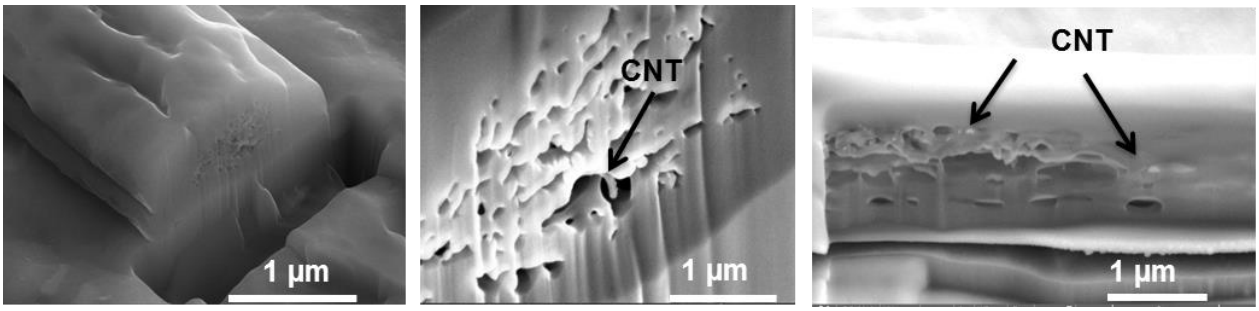

Fig. 67: FIB-SEM images of 1 wt% CNT nanocomposite fibers showing alignment and porosity inside the fiber.

6. Summary and outlook

In the first part of this thesis, a unique approach for producing 3D nozzles optimized for creating stable thin sheets, was established and tested. Nozzles high aspect ratio structures were produced by well-established soft-lithography techniques which allow for an exact control over the design and high-reproducibility of the nozzle geometry. Furthermore, optimized nozzle parameters are used to form different flow of liquid jets such as droplets, whipping droplets and fiber spinning for many applications such as single-particle imaging, nanorheology, X-ray spectroscopy [291-293]. The second part of the work benefits from advancements of microfocused scattering techniques, which leads to the development of shear and flow orientation dynamics of anisotropic nanoparticles in microfluidic sheet-like liquid jets and jets to investigate their dynamics. In the third section, these device technologies were used for spinning of functional micro/nanofibers.

Here, we reported the development, fabrication and testing of high aspect ratio microfluidic flat liquid jet devices. These devices are based on the GDVN principle, where the liquids are focused by a co-axially flowing gas. Commercially available capillary nozzles are typically made of glass, involving complicated fabrication steps and offering only weak geometry control. Hence, design evolution, reproducibility and mass production are limited. To overcome this limitation of glass capillaries, the fabrication of microfluidic liquid jet devices based on soft-lithography has been established in our group during the last years. The highly stable thin liquid sheets reported here enable the reduction of sample consumption up to tenfold compared to colliding liquid jets. This high fidelity and cost-effective sheet-GDVN technology can be implemented at ultrabright photon sources, which require the continuous sample replenishment, such as in the XFELs [294]. Moreover, this experimental methodology can also be utilized at synchrotrons and for laser spectroscopy setups to minimize the sample consumption during long experiments. Furthermore, this microfluidic device runs mostly clogging-free and highly reliable over long periods of time. These microfluidic devices further offer the benefit of a parallelized nozzle design which enables to create complex jet-in-jet-focusing geometries or complete arrays of multiple nozzles simultaneously in one fabrication sequence. Consequently, the device footprint is very small, which enables fast nozzle changes by simply switching to the adjacent nozzles.

Taking advantage of this design control, the relevant parameters, such as liquid flow rate and pressure difference, were varied to systematically study the liquid jet dynamics. These high aspect ratio devices reproducibly generate a series of alternating, orthogonal liquid sheets with thicknesses of approximately a few microns. Here, we found that the microfluidic flat liquid jet diameters can adjust with great control by varying the pressures and flow rates. The generation of stable liquid sheets shows a series of nodes, which are produced due to the interdependent inertial and surface tension forces. These liquid sheets are formed between big liquid rims, which initially move apart and then approach each other again to collide, in the form of a nodal point, consequently forming a new rimmed flat sheet perpendicular to the preceding one. This work enriches multiple arenas such as soft X-ray spectroscopy, which includes ultrafast molecular science, ultrafast chemical dynamics, X-ray beam diagnostics and nano-rheology as well as functional fiber spinning, thereby offering exciting well-grounded versatile opportunities.

The optimized microfluidic flat liquid jet system has been used to study complex fluids (dispersion of spindle-shaped nanoparticles) via wide-angle (WAXS) X-ray scattering at ESRF, Grenoble. The orientation of anisotropic particles has been investigated in sheet-like microjets. WAXS patterns show a pronounced alignment of dispersed single-crystalline hematite particles in the flow direction. Their orientation profile was analyzed from the center of the sheet and flipping zone. Furthermore, it was determined how the orientation influences the behavior of particles along the sheet. Due to the GDVN gas flow, the center of the sheet and the flipping zone is stretched out along the central flow axis, causing particle alignment in the direction of the central axis of the flow. The extended nodes within such a velocity profile will experience a torque which results in an alignment of the particles along the flow direction. This study gives a characterization of the spindle-shaped particles degree of alignment within a microfluidic flat liquid in a GDVN produced flow. The results of this work and the orientation effect, in general, are of great importance for applications that require orientation control, such as injection molding, fiber spinning, or processing of functional fibers.

Furthermore, we reported a new microfluidic GDVN nozzle, which allows continuous and reproducible fabrication of stable and uniform micro-/nanofibers with controlled surface morphologies and overall shapes. The influence of air pressure, polymer concentration and flow rate on the properties of the fiber were investigated and revealed that surface roughness was

controlled by a combination of air pressure and polymer concentration while the diameter and shape of the fibers were primarily influenced by the concentration of the polymer solution and marginally by the air pressure. A wide range of diameters ranging from a few hundred nanometers and up to ~15 µm were spun as continuous single fibers using the same microfluidic device, which indicates the highly tunable operational nature of this technique. To our knowledge, this microfluidic solution blow spinning concept is the most gentle and most uncomplicated setup described to date for the fabrication of (sub-)micrometer fibers. Our extensive study of fiber morphologies shows a high tunability of their properties. The formation of rough, smooth, or grooved surfaces was attributed to the interplay of the evaporation process and the velocity (mis)match between polymer solution jet and its surrounding air stream. FIB-cut fiber cross-sections also revealed that by simply changing the polymer concentration, fiber with different porosities could be obtained. These porous fibers have potential applications as scaffolds for tissue engineering, where cells could be loaded directly into fiber, which would not be possible with electrospinning.

Based on high-speed video imaging as well as SEM analysis of the fibers obtained, a model describing the fiber formation process was developed, which connects the fiber diameter with both the gas flow-focused jet diameter and a further thinning regime. The facile fabrication, as well as the operation of the devices, provides a new and robust preparation procedure of microfibers. The devices can be re-used or, if contaminated, discarded due to their low fabrication cost. The gas-focusing geometry allowed for stable fiber jetting, meaning that these nozzles could be used to also directly coat surfaces in fiber, without the need of an intermediate spooling step. The current types of fibers produced have applications in various areas such as air/water filtration units, drug delivery systems and cell growth studies. Further developments will enable the fabrication of more sophisticated devices which can provide jet-in-jet environments for the fabrication of more sophisticated fibers with core-shell, side by side, or Janus-like structures. The jet-in-jet approach will also allow for the incorporation of more clogging prone additives, such as CNTs or other large, high aspect ratio nanoparticles. With this technique, the fabrication of highly functional micro-/nanowires or complex nonwoven structures can be achieved and are currently under investigation.

Future work related to optimized microfluidic liquid jet technology may include many applications, as shown in Fig.68. New microfluidic channel geometries can be designed to create

more complex structures like core-shell fibers. With a jet-in-jet configuration, a core containing, e.g., CNTs, can be coated with a polymer. Due to the first hydrodynamic focusing region, the CNTs are concentrated into a small area. Moreover, this should lower the percolation threshold drastically for electrical conductivity and improve the alignment along the flow direction. Furthermore, it can overcome the issues with clogging, since the CNTs do not touch the channel walls anymore. With this technique, the fabrication of electrical micro/nanowires or complex nonwoven conductive structures can be achieved.

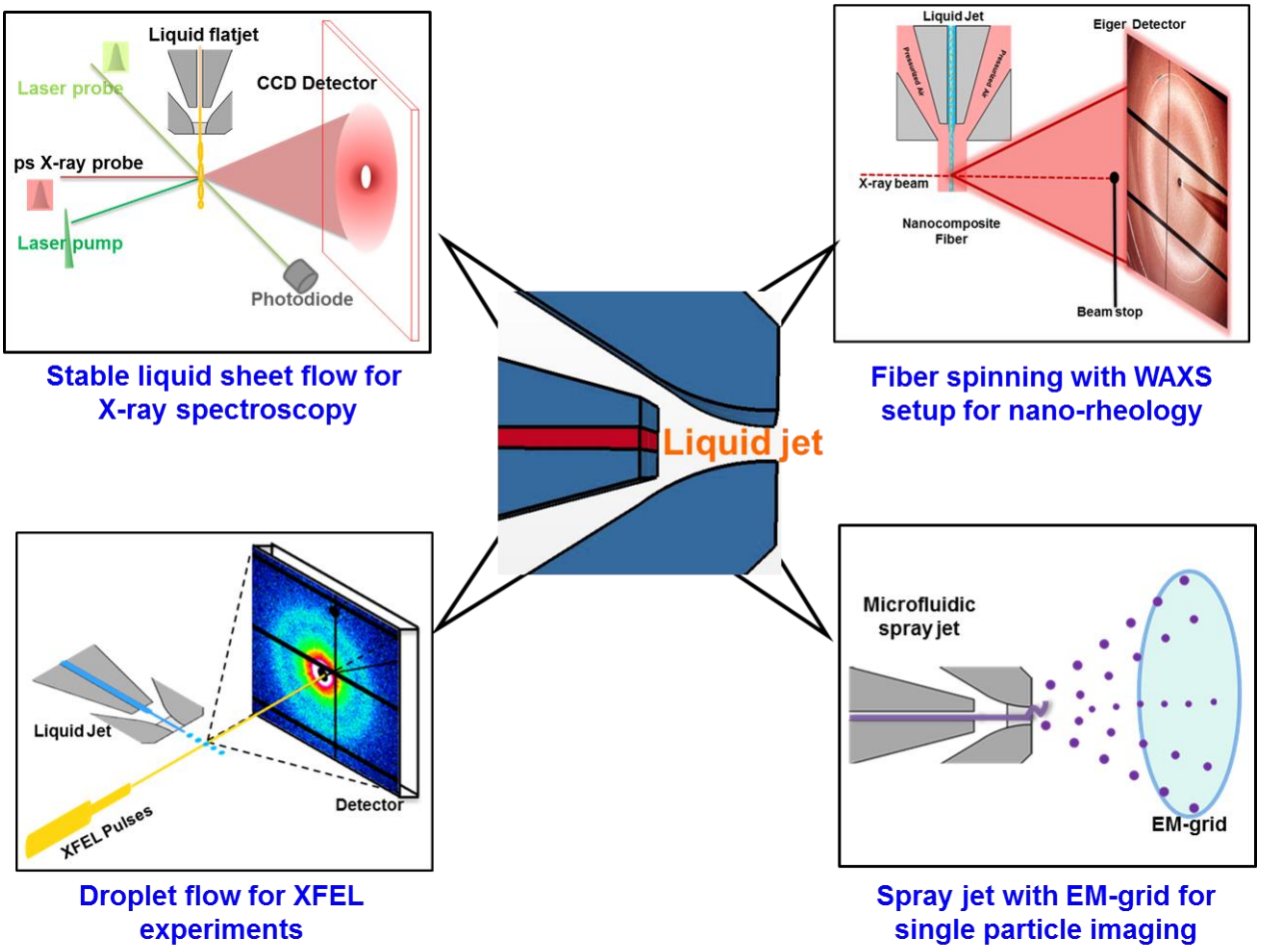

Fig. 68: Overview of future experiments can perform using optimized liquid jet technology.

These optimized microfluidic liquid jets are often used at XFEL sources where new types of experiments such as sheet-like flow for X-ray spectroscopy to study the molecular excitations and fast droplet flow for single-particle imaging [295, 296]. Therefore the flow alignment of such

bio-molecules may need to be considered and taken into account in future experiments. New developments related to other flows of liquid jets such a *in-situ* fiber spinning at synchrotron facilities will give a complete overview of particle orientation and structure-function relationship. Another outcome of this nozzle geometry can be used for fast and effective microfluidic spraying method for high-resolution single-particle Cryo-EM, as shown the setup in Fig.62 (297). Single-particle cryo-EM is a powerful technique in structural biology as it provides near-atomic-resolution structures for macromolecular assemblies [298, 299].

Bibliography

1. Fry, A.R., and Arrigoni, M., FEL Pulses and Ultrafast Lasers Team Up to Explore New Frontiers, *Photonics Spectra*, 46, 57-59 (2012).

2. Koopmann, R., et al., In vivo protein crystallization opens new routes in structural biology, *Nature methods*, 9(3), 259-262 (2012).

3. Boutet, S., et al., High-Resolution Protein Structure Determination by Serial Femtosecond Crystallography. *Science*, 337(6092), 362-364 (2012).

4. Taheri, S. M., et al., Lyotropic phase behavior of polymer-coated iron oxide nanoparticles. *Soft Matter*, 8(48), 12124 (2012).

5. Wiedorn M.O., et al., Megahertz serial crystallography, *Nature Communications*, 9, 4025 (2018).

6. Ekimova, M., Quevedo, W., Faubel, M., Wernet, P., and Nibbering, E. T. J., A liquid flat jet system for solution phase soft X-ray spectroscopy. *Structural Dynamics*, 2(5), 054301 (2015).

7. Trebbin, M., Kruger, K., DePonte, D., Roth, S.V., Chapman, H.N., and Forster, S., Microfluidic liquid jet system with compatibility for atmospheric and high-vacuum conditions, *LabChip*, 14, 1733-1745 (2014).

8. Vasireddi, R., Narayanasamy, S. R., Monteiro, D.C.F., Kopf, F., Huse, N., and Trebbin, M., Development of a stable microfluidic flat liquid jet system for versatile applications, *LabChip*, in preparation (2019).

9. Koralek, J.D., Kim, J.B., Bruza, P., Curry, C.B., Chen, Z., Bechtel, H.A., Cordones, A.A., Sperling, P., Toleikis, S., Kern, J.F., Moeller, S.P., Glenzer, S.H., and DePonte, D.P., Generation and characterization of ultrathin free-flowing liquid sheets, *Nature Communications* 9, 1353(2018).

10. Ganan-Calvo., A.M., Generation of Steady Liquid Microthreads and Micron-Sized Monodisperse Sprays in Gas Streams, *Physical review Letters* 80, 285-288 (1998).

11. Trebbin, M., et al. Anisotropic particles align perpendicular to the flow direction in narrow microchannels. *Proceedings of the National Academy of Sciences*, 110(17), 6706-6711 (2013).

12. Emma, P. et al. First lasing and operation of an angstrom-wavelength free-electron laser. *Nature Photonics*, 4(9), 641–647 (2010).

13. Buffet, A., et al., P03, the microfocus, and nanofocus X-ray scattering (MiNaXS) beamline of the PETRA III storage ring: the microfocus endstation. *Journal of Synchrotron Radiation,* 19(4), 647-653 (2012).

14. Stribeck, N., et al., Volume-Resolved Nanostructure Survey of a Polymer Part by Means of SAXS Microtomography. *Macromolecular Chemistry and Physics*, 207(13), 1139-1149 (2006).

15. Pollack, L., et al., Time Resolved Collapse of a Folding Protein Observed with Small Angle X-Ray Scattering. *Physical Review Letters,* 86(21), 4962-4965 (2001).

16. Ullrich, J., Rudenko, A., and Moshammer, R., Free-Electron Lasers: New Avenues in Molecular Physics and Photochemistry. *Annual Review of Physical Chemistry,* 63(1), 635-660 (2012).

17. Ganan-Calvo, A.M., The scaling of exploding liquid jets under intense X-ray pulses, *arXiv,* 1811.04402, (2018).

18. Wiedorn, M. O., Rapid sample delivery for megahertz serial crystallography at X-ray FELs, *IUCrJ,* 5, 574–584 (2018).

19. Röntgen, W. C., Über eine neue Art von Strahlen. Sitzungsberichte der Wuerzburger Physik.-medic. Gesellschaft, (1895).

20. Stribeck N., X-ray scattering of soft matter, Springer: Berlin, New York, (2007).

21. Riekel C, et al., Micro X-Ray Small-Angle Scattering with Synchrotron-Radiation, J. of Macromolecular Sc., Part B, B37, 587–599 (1998).

22. Timmann, A., et al., Small angle x-ray scattering with a beryllium compound refractive lens as focusing optic. *Review of Scientific Instruments,* 80(4), 046103 (2006).

23. Snigirev, A., Kohn, V., Snigireva, I., and Lengeler, B., A compound refractive lens for focusing high-energy X-rays. *Nature,* 384(6604), 49-51 (1996).

24. Martel, A., et al., A microfluidic cell for studying the formation of regenerated silk by synchrotron radiation small- and wide-angle X-ray scattering. *Biomicrofluidics,* 2(2), 024104 (2008).

25. Otten, A., et al., Microfluidics of soft matter investigated by small-angle X-ray scattering. *Journal of Synchrotron Radiation,* 12(6), 745–750 (2005).

26. Schroer, C. G., and Lengeler, B., Focusing Hard X Rays to Nanometer Dimensions by Adiabatically Focusing Lenses. *Physical Review Letters,* 94(5) (2005).

27. Riekel, C., Burghammer, M., and Davies, R., Progress in micro- and nano-diffraction at the ESRF ID13 beamline. *IOP Conference Series: Materials Science and Engineering*, 14, 012013 (2010).

28. Robinson, I., Gruebel, G., and Mochrie, S., Focus on X-ray beams with high coherence. *New Journal of Physics*, 12(3), 035002 (2010).

29. Treusch, R., and Feldhaus, J., FLASH: new opportunities for (time-resolved) coherent imaging of nanostructures. *New Journal of Physics*, 12(3), 035015 (2010).

30. Suckewer, S., and Jaeglé, P. X-Ray laser: past, present, and future. *Laser Physics Letters*, 6(6), 411-436 (2009).

31. Ackermann, W., et al., Operation of a free-electron laser from the extreme ultraviolet to the water window. *Nature Photonics*, 1(6), 336–342 (2007).

32. Yan, H., Conley, R., Bouet, N., and Chu, Y. S., Hard x-ray nanofocusing by multilayer Laue lenses. Journal of Physics D: *Applied Physics*, 47(26), 263001 (2014).

33. Stangl, J., Mocuta, C., Chamard, V., and Carbone, D., Nanobeam X-Ray Scattering: Probing Matter at the Nanoscale, Weinheim, Germany: *Wiley*, (2014).

34. Altarelli, M., the European X-ray Free-Electron Laser: toward an ultra-bright, high repetition-rate x-ray source, *High Power Laser Science and Engineering*, 3. (2015).

35. Bartzsch, S., and Oelfke, U., Line focus x-ray tubes-a new concept to produce high brilliance x-rays, *Physics in Medicine & Biology*, 62(22), 8600-8615 (2017).

36. Müller, M., Riekel, C., Vuong, R., and Chanzy, H., Skin/core micro-structure in viscose rayon fibres analysed by X-ray microbeam and electron diffraction mapping. Polymer, 41(7), 2627-2632 (2000).

37. Seidel, R., et al., Mapping fibre orientation in complex-shaped biological systems with micrometre resolution by scanning X-ray microdiffraction. *Micron*, 39(2), 198-205 (2008).

38. Riekel, C., et al., X-ray Microdiffraction Study of Chain Orientation in Poly (p-phenylene terephthalamide). *Macromolecules*, 32(23), 7859-7865 (1999).

39. Martel, A., et al., Silk Fiber Assembly Studied by Synchrotron Radiation SAXS/WAXS and Raman Spectroscopy. *Journal of the American Chemical Society*, 130(50), 17070-17074 (2008).

40. Riekel, C., et al., Influence of CO 2 on the micro-structural properties of spider dragline silk: X-ray microdiffraction results. *Naturwissenschaften*, 91(1), 30-33 (2004).

41. Kinahan, M. E., et al., Tunable Silk: Using Microfluidics to Fabricate Silk Fibers with Controllable Properties. *Biomacromolecules,* 12(5), 1504-1511 (2011).

42. Moulin, J.F., et al., Flow at interfaces: A new device for x-ray surface scattering investigations. *Review of Scientific Instruments,* 79(1), 015109 (2008).

43. Thiele, C., Monteiro, D.C.F., R, Vasireddi, Schroer, C., and Trebbin, M. Dynamic flow alignment of anisotropic particles in liquids studied by in situ SAXS tomography. *in preparation* (2019).

44. Neutze, R., Wouts, R., van der Spoel, D., Weckert, E., and Hajdu, J., Potential for biomolecular imaging with femtosecond X-ray pulses. *Nature,* 406(6797), 752–757 (2000).

45. Caleman, C., et al., On the Feasibility of Nanocrystal Imaging Using Intense and Ultrashort X-ray Pulses. *ACS Nano,* 5(1), 139-146 (2010).

46. Spence, J. C. H., Weierstall, U., and Chapman, H. N., X-ray lasers for structural and dynamic biology. *Reports on Progress in Physics,* 75(10), 102601 (2012).

47. Neutze, R., and Moffat, K. Time-resolved structural studies at synchrotrons and X-ray free electron lasers: opportunities and challenges. *Current Opinion in Structural Biology,* 22(5), 651-659 (2012).

48. Sun, Z., Fan, J., Li, H., and Jiang, H., Current Status of Single Particle Imaging with X-ray Lasers. *Applied Sciences,* 8(1), 132 (2018).

49. Russell, R., et al., Rapid compaction during RNA folding. *Proceedings of the National Academy of Sciences,* 99(7), 4266-4271 (2002).

50. Lomb, L., et al., Radiation damage in protein serial femtosecond crystallography using an x-ray free-electron laser. *Physical Review B,* 84(21) (2011).

51. Neutze, R., Brändén, G., and Schertler, G. F., Membrane protein structural biology using X-ray free electron lasers. *Current Opinion in Structural Biology,* 33, 115-125 (2015).

52. Johansson, L. C., Stauch, B., Ishchenko, A., and Cherezov, V., A Bright Future for Serial Femtosecond Crystallography with XFELs. *Trends in Biochemical Sciences*, 42(9), 749–762 (2017).

53. Spence, C., et al. "XFELs for structure and dynamics in biology", *IUCrJ* 4, 322 (2017).

54. Chergui, M., et al., Time-resolved X-ray spectroscopies of chemical systems: New perspectives. *Structural Dynamics,* 3(3), 031001. (2016).

55. Abela, R., et al., Perspective: Opportunities for ultrafast science at SwissFEL. *Structural Dynamics*, 4(6), 061602 (2017).

56. Kubin, M., et al., Soft x-rays absorption spectroscopy of metalloproteins and high-valent metal-complexes at room temperature using free-electron lasers. *Structural Dynamics*, 4(5), 054307 (2017).

57. Hong, K., et al., Element-Specific Characterization of Transient Electronic Structure of Solvated Fe(II) Complexes with Time-Resolved Soft X-ray Absorption Spectroscopy. *Accounts of Chemical Research*, 48(11), 2957–2966 (2015).

58. Ghazal, A., et al., Recent advances in X-ray compatible microfluidics for applications in soft materials and life sciences. *Lab on a Chip*, 16(22), 4263-4295 (2016).

59. Stone, H. A., Stroock, A. D., and Ajdari, A., Engineering Flows In Small Devices. Annual *Review of Fluid Mechanics*, 36(1), 381-411 (2004).

60. Groisman, A., Microfluidic Memory and Control Devices. *Science*, 300(5621), 955–958 (2003).

61. Abate, A. R., Agresti, J. J., and Weitz, D. A., Microfluidic sorting with high-speed single-layer membrane valves. *Applied Physics Letters*, 96(20), 203509 (2010).

62. Whitesides, G. M., The origins and the future of microfluidics. *Nature*, 442(7101), 368–373 (2006).

63. Abate, A. R., et al., High-throughput injection with microfluidics using picoinjectors. *Proceedings of the National Academy of Sciences*, 107(45), 19163–19166 (2010).

64. Pihl, J., Sinclair, J., Karlsson, M., and Orwar, O., Microfluidics for cell-based assays. *Materials Today*, 8(12), 46-51 (2005).

65. Pfohl, T., Mugele, F., Seemann, R., and Herminghaus, S., Trends in Microfluidics with Complex Fluids. *ChemPhysChem*, 4(12), 1291-1298 (2003).

66. Bhargava, K., Thompson, B., Tembhekar, A., and Malmstadt, N. Temperature Sensing in Modular Microfluidic Architectures. *Micromachines*, 7(1), 11 (2016).

67. Song, Y., Hormes, J., and Kumar, C. S. S. R., Microfluidic Synthesis of Nanomaterials. *Small*, 4(6), 698-711 (2008).

68. Ho, C.-M., and Tai, Y.-C., Micro-Electro-Mechanical-Systems (Mems) And Fluid Flows. *Annual Review of Fluid Mechanics*, 30(1), 579–612 (1998).

69. Li, R., Lv, X., Zhang, X., Saeed, O., and Deng, Y., Microfluidics for cell-cell interactions: A review. *Frontiers of Chemical Science and Engineering*, 10(1), 90–98 (2015).

70. Capretto, L., Carugo, D., Mazzitelli, S., Nastruzzi, C., and Zhang, X., Microfluidic and lab-on-a-chip preparation routes for organic nanoparticles and vesicular systems for nanomedicine applications. *Advanced Drug Delivery Reviews*, 65(11-12), 1496–1532 (2013).

71. Xia, Y., and Whitesides, G. M., Soft Lithography. *Annual Review of Materials Science*, 28(1), 153-184 (1998).

72. Manz, A., Graber, N., and Widmer, H. M., Miniaturized total chemical analysis systems: A novel concept for chemical sensing. *Sensors and Actuators B: Chemical*, 1(1-6), 244–248 (1990).

73. Thorsen, T., Microfluidic Large-Scale Integration. *Science*, 298(5593), 580-584 (2002).

74. Lee, C.C., Multistep Synthesis of a Radiolabeled Imaging Probe Using Integrated Microfluidics. *Science*, 310(5755), 1793-1796 (2005).

75. Kulasinghe, A., Wu, H., Punyadeera, C., and Warkiani, M. The Use of Microfluidic Technology for Cancer Applications and Liquid Biopsy. Micromachines, 9(8), 397 (2018).

76. Hany, C., Lebrun, H., Pradere, C., Toutain, J., and Batsale, J.C., Thermal analysis of chemical reaction with a continuous microfluidic calorimeter. *Chemical Engineering Journal*, 160(3), 814–822 (2010).

77. Cui, P., and Wang, S., Applications of microfluidic chip technology in pharmaceutical analysis: A review. *Journal of Pharmaceutical Analysis* (2018).

78. Wlodkowic, D., and Darzynkiewicz, Z. Rise of the Micromachines: Microfluidics and the Future of Cytometry. Recent Advances in Cytometry, Part A - Instrumentation, *Methods*, 105–125 (2011).

79. Rothbauer, M., Zirath, H., and Ertl, P. Recent advances in microfluidic technologies for cell-to-cell interaction studies. *Lab on a Chip*, 18(2), 249–270 (2018).

80. Seiffert, S., and Weitz, D. A. Microfluidic fabrication of smart microgels from macromolecular precursors. *Polymer*, 51(25), 5883–5889 (2010).

81. Priest, C., et al., Microfluidic polymer multilayer adsorption on liquid crystal droplets for microcapsule synthesis. *Lab on a Chip*, 8(12), 2182 (2008).

82. Ramsey, R. S., and Ramsey, J. M. Generating Electrospray from Microchip Devices Using Electroosmotic Pumping. *Analytical Chemistry*, 69(6), 1174–1178 (1997).

83. Li, W., Greener, J., Voicu, D., and Kumacheva, E., Multiple modular microfluidic (M3) reactors for the synthesis of polymer particles. *Lab on a Chip*, 9(18), 2715 (2009).

84. Hansen, C. L., Skordalakes, E., Berger, J. M., and Quake, S. R., A robust and scalable microfluidic metering method that allows protein crystal growth by free interface diffusion. *Proceedings of the National Academy of Sciences*, 99(26), 16531–16536 (2002).

85. Hansen, C., and Quake, S.R., Microfluidics in structural biology: smaller, faster em leader better, *Curr Opin Struct Biol*. 13(5):538-44 (2003).

86. Pushkarev, D., Neff, N. F., and Quake, S. R., Single-molecule sequencing of an individual human genome. *Nature Biotechnology*, 27(9), 847–850 (2009).

87. Tumarkin, E., and Kumacheva, E., Microfluidic generation of microgels from synthetic and natural polymers. *Chemical Society Reviews*, 38(8), 2161 (2009).

88. Song, Y., et al., Microfluidic Synthesis of Cobalt Nanoparticles. *Chemistry of Materials*, 18(12), 2817-2827 (2006).

89. Jahn, A., et al., Preparation of nanoparticles by continuous-flow microfluidics. *Journal of Nanoparticle Research*, 10(6), 925-934 (2008).

90. Mansur, E. A., YE, M., WANG, Y., and DAI, Y. A State-of-the-Art Review of Mixing in Microfluidic Mixers. *Chinese Journal of Chemical Engineering*, 16(4), 503–516 (2008).

91. Pollack, L., et al., Time Resolved Collapse of a Folding Protein Observed with Small Angle X-Ray Scattering. *Physical Review Letters*, 86(21), 4962–4965 (2001).

92. Johansson, L. C., Stauch, B., Ishchenko, A., and Cherezov, V., A Bright Future for Serial Femtosecond Crystallography with XFELs. *Trends in Biochemical Sciences*, 42(9), 749–762 (2017).

93. Knight, J. B., Vishwanath, A., Brody, J. P., and Austin, R. H. Hydrodynamic Focusing on a Silicon Chip: Mixing Nanoliters in Microseconds. *Physical Review Letters*, 80(17), 3863–3866 (1998).

94. Vasireddi et al., Development of a high fidelity stable microfluidic flat liquid jet system for versatile applications, *in preparation* (2019).

95. Priest, C., et al., Surface patterning of bonded microfluidic channels. *Biomicrofluidics*, 4(3), 032206 (2010).

96. Valerio, J., Structure of complex fluids under shear flows, Ph.D. thesis, University of Hamburg (2018).

97. Nette, J., 3D Design of Nozzles for microfluidic liquid flat jet devices, Master thesis, University of Hamburg (2018).

98. Vakili, M., Vasireddi, R., Trebbin, M., Fully Polyimide-based Liquid Jet Systems for

in-situ X-ray Studies, *in preparation* (2019).

99. Mair, D. A., et al., Injection molded microfluidic chips featuring integrated interconnects. *Lab Chip*, 6(10), 1346-1354 (2006).

100. Dhouib, K., et al., Microfluidic chips for the crystallization of biomacromolecules by counter-diffusion and on-chip crystal X-ray analysis. *Lab on a Chip*, 9(10), 1412 (2009).

101. Nelson, G., et al., Three-dimensional-printed gas dynamic virtual nozzles for x-ray laser sample delivery. *Optics Express*, 24(11), 11515 (2016).

102. Zhao, X.-M., Xia, Y., and Whitesides, G. M., Soft lithographic methods for nano-fabrication. *Journal of Materials Chemistry*, 7(7), 1069-1074 (1997).

103. Thiele, J., et al., Early development drug formulation on a chip: Fabrication of nanoparticles using a microfluidic spray dryer. *Lab on a Chip*, 11(14), 2362 (2011).

104. Heida, T., et al., Mechanically Defined Microgels by Droplet Microfluidics. *Macromolecular Chemistry and Physics*, 218(2), 1600418 (2016).

105. Tommoaso, B et al., Three-Dimensional Microfabrication Using Two-Photon Polymerization, Elsevier, (2020).

106. Meents, A., et al., Pink-beam serial crystallography, *Nature Communications* 8 (1), 1281, (2017).

107. Oberthuer, D., et al., Double-flow focused liquid injector for efficient serial femtosecond crystallography. *Scientific Reports*, 7(1) (2017).

108. Wiedorn, M. O., et al., Megahertz serial crystallography. *Nature Communications*, 9(1) (2018).

109. Ganan-Calvo., A.M., et al., Device and method for the production of aerodynamically stabilized, electrified microscopic jets for the transport of samples, *US Patent*, 15, 225 (2018).

110. Quake, S. R., From Micro- to Nanofabrication with Soft Materials. *Science*, 290(5496), 1536-1540 (2000).

111. Ren, K., Dai, W., Zhou, J., Su, J., and Wu, H., Whole-Teflon microfluidic chips. *Proceedings of the National Academy of Sciences*, 108(20), 8162-8166 (2011).

112. Montanero, J. M., and Ganan-Calvo, A. M. Stability of coflowing capillary jets under nonaxisymmetric perturbations. *Physical Review E*, 77(4) (2008).

113. Herrada, M. A., et al., Liquid flow focused by a gas: Jetting, dripping, and recirculation. *Physical Review E*, 78(3) (2008).

114. Luu, T.T., et al., Extreme – ultraviolet high – harmonic generation in liquids, *Nature Communications*, 9, 3723 (2018).

115. Kondoh, M., and Tsubouchi, M. Liquid-sheet jets for terahertz spectroscopy. *Optics Express*, 22(12), 14135 (2014).

116. Sanjay, V., and Das, A. K., Formation of liquid chain by collision of two laminar jets. *Physics of Fluids*, 29(11), 112101 (2017).

117. Chapman, H. N., et al., Femtosecond X-ray protein nanocrystallography. *Nature*, 470(7332), 73-77 (2011).

118. Oberthuer, D., et al., Double-flow focused liquid injector for efficient serial femtosecond crystallography. *Scientific Reports*, 7(1) (2017).

119. Galinis, G., et al., Micrometer-thickness liquid sheet jets flowing in vacuum. *Review of Scientific Instruments*, 88(8), 083117 (2017).

120. Fromme, P., XFELs open a new era in structural chemical biology. *Nature Chemical Biology*, 11(12), 895-899 (2015).

121. Näslund, L.Å., et al., X-ray Absorption Spectroscopy Measurements of Liquid Water. *The Journal of Physical Chemistry B*, 109(28), 13835-13839 (2005).

122. Vad, T., et al., "Orientation of Well-Dispersed Multiwalled Carbon Nanotubes in Melt-Spun Polymer Fibers and Its Impact on the Formation of the Semicrystalline Polymer Structure: A Combined Wide-Angle X-ray Scattering and Electron Tomography Study". *Macromolecules*, 46 (14) 5604-5613 (2013).

123. Håkansson, K. M. O., et al., Hydrodynamic alignment and assembly of nanofibrils resulting in strong cellulose filaments. *Nature Communications*, 5(1) (2014).

124. McWhirter, J. L., Noguchi, H., and Gompper, G., Flow-induced clustering, and alignment of vesicles and red blood cells in microcapillaries. *Proceedings of the National Academy of Sciences*, 106(15), 6039-6043 (2009).

125. Kamada, A., et al., Flow-assisted assembly of nanostructured protein microfibers. *Proceedings of the National Academy of Sciences*, 114(6), 1232-1237 (2017).

126. Gutt, C., et al., Single Shot Spatial and Temporal Coherence Properties of the SLAC Linac Coherent Light Source in the Hard X-Ray Regime. *Physical Review Letters*, 108(2) (2012).

127. Luu, T. T., et al., Extreme–ultraviolet high–harmonic generation in liquids. *Nature Communications*, 9(1) (2018).

128. Galinis, G., et al., Micrometer-thickness liquid sheet jets flowing in vacuum. *Review of Scientific Instruments*, 88(8), 083117 (2017).

129. Vasireddi, R., et al., Shear and Flow Orientation Dynamics of Anisotropic Nanoparticles in Microfluidic Sheet-like Microjets, *in preparation* (2109).

130. Mohtaschemi, M., et al., Rheology dynamics of aggregating colloidal suspensions. *Soft Matter,* 10(17), 2971 (2014).

131. Löwen, H., et al., Colloidal layers in magnetic fields and under shear flow. *Journal of Physics: Condensed Matter,* 17(45), S3379-S3386 (2005).

132. Xu, X., Rice, S. A., and Dinner, A. R., Relation between ordering and shear thinning in colloidal suspensions. *Proceedings of the National Academy of Sciences*, 110(10), 3771–3776 (2013).

133. Liu, F., et al., Fabrication of highly oriented nanoporous fibers via airflow bubble-spinning. *Appl Surf Sci* 421:61-67 (2017).

134. Yuan, X., et al., Characterization of poly(L-lactic acid) fibers produced by melt spinning. *J Appl Polym Sci* 81(1): 251-260 (2001).

135. Puppi, D., et al., Development of 3D wet-spun polymeric scaffolds loaded with antimicrobial agents for bone engineering. *J Bioact Compat Pol* 26 (5): 478-492 (2011).

136. Pham, U.H.T., A microfluidic device approach to generate hollow alginate microfibers with controlled wall thickness and inner diameter. *J Appl Phys* 117 (21): 214703 (2015).

137. Bhardwaj, N., and Kundu, S.C., Electrospinning. A fascinating fiber fabrication technique. *Biotechnol Adv* 28(3): 325-347 (2010).

138. Rajgarhia, S.S., and Jana, S.C., Comparison of Electrospinning and Gas Jet Fiber Processes for Fabrication of Bi-Component Polymer Nanofibers from Single Solutions. *Macromol Symp* 369(1): 8-13 (2016).

139. Hofmann, E., et al., Microfluidic nozzle device for ultrafine fiber solution blow spinning with precise diameter control. *Lab Chip* 18, 2225-2234 (2018).

140. Daniele, M.A., et al., Microfluidic strategies for design and assembly of microfibers and nanofibers with tissue engineering and regenerative medicine applications. *Adv Healthc Mater* 4 (1): 11-28 (2015).

141. Tuzlakoglu, K., et al., Production and characterization of chitosan fibers and 3-D fiber mesh scaffolds for tissue engineering applications. *Macromol Biosci* 4(8): 811-819 (2004).

142. Mortimer, C.J., and Wright, C.J., The fabrication of iron oxide nanoparticle nanofiber composites by electrospinning and their applications in tissue engineering. *Biotechnol J* 12(7) 1600693 (2017).

143. Thielke, M.W., et al., Thiol-ene modification of electrospun polybutadiene fibers crosslinked by UV irradiation. *Polymer* 55(22): 5596-5599 (2014).

144. Thielke, M.W., et al., Electrospinning of crystallizable polypeptoid fibers. *Macromol Rapid Commun* 37(1): 100-104 (2015).

145. Cheng, J., et al., Electrospinning versus microfluidic spinning of functional fibers for biomedical applications. *Biomaterials* 114:121-143 (2017).

146. Bhardwaj, N., et al., Electrospinning. A fascinating fiber fabrication technique. *Biotechnol Adv* 28(3):325-347 (2010).

147. Huang, Z.M., et al., review on polymer nanofibers by electrospinning and their applications in nanocomposites. *Compos Sci Technol* 63(15):2223-2253 (2003).

148. Sackmann, E.K., Fulton, A.L., and Beebe, D.J., The present and future role of microfluidics in biomedical research. *Nature* 507(7491):181-189 (2014).

149. Jun, Y., Kang, E., Chae, S., and Lee, S., Microfluidic spinning of micro- and nano-scale fibers for tissue engineering. *Lab Chip* 14(13): 2145-2160 (2014).

150. Zhao, J., Xiong, W., Yu, N., and Yang, X., Continuous Jetting of Alginate Microfiber in Atmosphere Based on a Microfluidic Chip. *Micromachines* 8 (1): 1-11 (2017).

151. Daristotle, J.L., et al., A review of the fundamental principles and applications of solution blow spinning. *ACS Appl Mater Interfaces* 8(51): 34951-34963 (2016).

152. Oliveira, J.E., et al. Nano and Submicrometric Fibers of Poly(D,L-Lactide) Obtained by Solution Blow Spinning: Process and Solution Variables. *J Appl Polym Sci* 122(5): 3396-3405 (2011).

153. Park. D., et al., Simultaneous microfluidic spinning of multiple strands of submicron fiber for the production of free-standing porous membranes for biological application. *Biofabrication* 9 (2):025026 (2017).

154. Ma, J., Wang, Y., and Liu, J., Biomaterials Meet Microfluidics: From Synthesis Technologies to Biological Applications. *Micromachines* 8 (8):255 (2017).

155. Guillot, P., Colin, A., Utada, A. S., and Ajdari, A., Stability of a jet in confined pressure-driven biphasic flows at low Reynolds numbers, *Phys. Rev. Lett*. **99**, 104502 (2007).

156. Biener, J., et al., Surface Chemistry in Nanoscale Materials. *Materials*, 2(4), 2404-2428 (2009).

157. DePonte, D. P., et al., Gas dynamic virtual nozzle for generation of microscopic droplet streams. Journal of Physics D: *Applied Physics*, 41(19), 195505 (2008).

158. Bogan, M. J., et al., Aerosol Imaging with a Soft X-Ray Free Electron Laser. *Aerosol Science and Technology*, 44(3), i–vi (2010).

159. Lehmkühler, F., Steinke, I., Schroer, M. A., Fischer, B., Sprung, M., and Grübel, G. Microsecond Structural Rheology. *The Journal of Physical Chemistry Letters*, 8(15), 3581–3585 (2017).

160. Weierstall, U., Liquid sample delivery techniques for serial femtosecond crystallography. *Philosophical Transactions of the Royal Society B: Biological Sciences*, 369(1647), 20130337–20130337 (2014).

161. Von Ardenne, B., Mechelke, M., and Grubmüller, H., Structure determination from single molecule X-ray scattering with three photons per image. *Nature Communications*, 9(1) (2018).

162. Ganan-Calvo, A. M., et al., The combination of electrospray and flow focusing. *Journal of Fluid Mechanics*, 566, 421 (2006).

163. Zeng, Q., et al., Jetting of viscous droplets from cavitation-induced Rayleigh–Taylor instability. *Journal of Fluid Mechanics*, 846, 916–943 (2018).

164. Ganan-Calvo, A. M., On the general scaling theory for electrospraying. *Journal of Fluid Mechanics*, 507, 203-212 (2004).

165. Cruz-Mazo, F., et al., Global stability of axisymmetric flow focusing. *Journal of Fluid Mechanics*, 832, 329–344 (2007).

166. Beyerlein, K. R., et al., Ultrafast nonthermal heating of water initiated by an X-ray Free-Electron Laser. *Proceedings of the National Academy of Sciences*, 115(22), 5652–5657 (2018).

167. Steinke, I., et al., A liquid jet setup for x-ray scattering experiments on complex liquids at free-electron laser sources. *Review of Scientific Instruments*, 87(6), 063905 (2006).

168. Rayleigh, L., On The Instability of Jets. *Proceedings of the London Mathematical Society*, s1-10(1), 4-13 (1878).

169. Eggers, J., and Villermaux, E., Physics of liquid jets. *Reports on Progress in Physics*, 71(3), 036601 (2008).

170. Hoeve, V., et al., Breakup of diminutive Rayleigh jets. *Physics of Fluids*, 22(12), 122003 (2010).

171. Hilbing, J. H., and Heister, S. D., Droplet size control in liquid jet breakup. *Physics of Fluids*, 8(6), 1574-1581 (1996).

172. Eggers, J., and Dupont, T. F., Drop formation in a one-dimensional approximation of the Navier–Stokes equation. *Journal of Fluid Mechanics*, 262(-1), 205 (1994).

173. Loscertales, I. G., Micro/Nano Encapsulation via Electrified Coaxial Liquid Jets. *Science*, 295(5560), 1695-1698 (2002).

174. Ganan-Calvo, A. M., Enhanced liquid atomization: From flow-focusing to flow-blurring. *Applied Physics Letters*, *86* 1-3 (2005).

175. Beyerlein, K. R., et al., Ceramic micro-injection molded nozzles for serial femtosecond crystallography sample delivery. *Review of Scientific Instruments*, 86(12), 125104 (2015).

176. Cruz-Mazo, F., Montanero, J. M. and Ganan-Calvo, A. M. Monosized dripping mode of axisymmetric flow focusing. *Physical Review E*, 94:053122 (2016).

177. Zahoor, R., Simulation of gas focused liquid jets, Ph.D. thesis, University of Nova Gorica, (2018).

178. Ganan-Calvo, A. M., Ferrera, C. and Montanero, J. M., Universal size and shape of viscous capillary jets: application to gas-focused microjets. *Journal of Fluid Mechanics*, *670*:427-438 (2011).

179. Cadarso, V. J., et al., Microdrop generation and deposition of ionic liquids. *Journal of Materials Research*, 29(17), 2100-2107 (2014).

180. Ganan-Calvo, A. M., et al., Liquid capillary micro/nanojets in free-jet expansion. *Small*, *6*:822-824 (2010).

181. DePonte, D. P., et al., SEM imaging of liquid jets. *Micron*, 40(4), 507–509 (2009).

182. Rayleigh, L., On The Instability Of Jets. *Proceedings of the London Mathematical Society*, s1-10(1), 4-13 (1878).

183. Ganan-Calvo, A. M., and Montanero, J. M., Revision of capillary cone-jet physics: Electrospray and flow focusing. *Physical Review E*, *79*:066305 (2009).

184. Acero, A. J., et al., A new flow focusing technique to produce very thin jets. *Journal of Micromechanics and Microengineering*, *23*:065009 (2013).

185. De Groot, J., Johansson, G. A., and Hertz, H. M., Capillary nozzles for liquid-jet laser-plasma x-ray sources. *Review of Scientific Instruments*, 74(8), 3881-3882 (2003).

186. Grünbein, M. L., Shoeman, R. L., and Doak, R. B., Velocimetry of fast microscopic liquid jets by nanosecond dual-pulse laser illumination for megahertz X-ray free-electron lasers. *Optics Express*, 26(6), 7190 (2018).

187. Priebe, M., et al., Orientation of biomolecular assemblies in a microfluidic jet. *New Journal of Physics*, 12(4), 043056 (2010).

188. Skou, M., et al., In situ microfluidic dialysis for biological small-angle X-ray scattering. *Journal of Applied Crystallography*, 47(4), 1355–1366 (2014).

189. Ganan-Calvo, A. M., Jetting–dripping transition of a liquid jet in a lower viscosity co-flowing immiscible liquid: the minimum flow rate in flow focusing. *Journal of Fluid Mechanics*, 553(-1), 75 (2006).

190. Panao, M.R.O., et al., Effect of pre-impingement length and misalignment in the hydrodynamics of multijet impingement atomization, *Physics of Fluids* 25, 012105 (2013).

191. Alessandra, P., et al. A closed-loop pump-driven wire-guided flow jet for ultrafast spectroscopy of liquid samples, *Review of Scientific Instruments* 86, 093105 (2015).

192. Akira, W., et al., a new nozzle producing ultrathin liquid sheets for femtosecond pulse dye lasers, *Optics Communications*, 7, 301-3014 (1989).

193. Naohiro, Y., et al., Impingement of liquid jets at atmospheric and elevated pressures: an observational study using paired water jets or water and methylcyclohexane jets, *Proc. R. Soc. A*, 466, 3501-3526 (2010).

194. Jens, E., et al., Physics of liquid jets, *Rep. Prog. Phys.*71, 036601 (2008).

195. Ganan-Calvo, A. M., Dávila, J., and Barrero, A., Current and droplet size in the electrospraying of liquids. Scaling laws. *Journal of Aerosol Science*, 28(2), 249-275 (1997).

196. Jake, D. K., et al., Generation and characterization of ultrathin free-flowing liquid sheets *Nature Communications* 9, 1353 (2018).

197. Baerns, M. et al. Technische Chemie. *Wiley-VCH Verlag, Weinheim*, (2006).

198. Zahoor, R., Bajt, S., and Šarler, B. Influence of Gas Dynamic Virtual Nozzle Geometry on Micro-Jet Characteristics. *International Journal of Multiphase Flow*, 104, 152-165 (2018).

199. Ferziger, J. H., and Peric, M., Computational methods for fluid dynamics, *Springer* (2002).

200. Versteeg, H., and Malalasekra, W., An Introduction to Computational Fluid Dynamics: The Finite Volume Method Approach, *Prentice Hall* (1996).

201. Quartapelle, L., Numerical Solution of the Incompressible Navier-Stokes Equations, *Birkhäuser Basel*, (1993).

202. Palma, E. D., and Matano, R. P., On the implementation of open boundary conditions for a general circulation model: The three-dimensional case. *Journal of Geophysical Research: Oceans*, 105(C4), 8605-8627 (2000).

203. Ruith, M., Development of boundary conditions for direct numerical simulations of three-dimensional vortex breakdown phenomena in semi-infinite domains. *Computers & Fluids*, 33(9), 1225–1250 (2004).

204. Terrapon, V. E., Dubief, Y., and Soria, J., On the role of pressure in elasto-inertial turbulence. *Journal of Turbulence*, 16(1), 26–43 (2014).

205. Edward, J., et al., Introduction to fluid mechanics, *Oxford University Press*, (2004).

206. Batchelor, G. K., An Introduction to Fluid Dynamics, *Cambridge University Press* (1967).

207. Beebe, D. J., Mensing, G. A., and Walker, G. M., Physics and Applications of Microfluidics in Biology. *Annual Review of Biomedical Engineering*, 4(1), 261-286 (2002).

208. Squires, T. M., and Quake, S. R. Microfluidics: Fluid physics at the nanoliter scale. *Reviews of Modern Physics*, 77(3), 977-1026 (2005).

209. Leib, S. J., and Goldstein, M. E., Convective and absolute instability of a viscous liquid jet. *Physics of Fluids*, 29(4), 952 (1986).

210. Lin., S. P., Breakup of liquid sheets and jets, *Cambridge University Press*, (2010).

211. Leib, S. J., and Goldstein, M. E., The generation of capillary instabilities on a liquid jet. *Journal of Fluid Mechanics*, 168(-1), 479 (1986).

212. Ganan-Calvo, A. M., Herrada, M. A., and Montanero, J. M. How does a shear boundary layer affect the stability of a capillary jet? *Physics of Fluids*, 26(6), 061701 (2014).

213. Sengupta, T., Poinsot, T., Instabilities of Flows: With and Without Heat Transfer and Chemical Reaction, *Springer*, (2010).

214. Lasheras, J. C., and Hopfinger, E. J., Liquid Jet Instability and Atomization in a Coaxial Gas Stream. *Annual Review of Fluid Mechanics*, 32(1), 275-308 (2000).

215. Tropea, C., Yarin, C., Foss, J. F., Handbook of Experiemntal Fluid Mechanics, *Spring*, 2007.

216. Guillot, P., Colin, A., Utada, A. S., and Ajdari, A., Stability of a jet in confined pressure-driven biphasic flows at low Reynolds numbers, *Phys. Rev. Lett*. 99, 104502 (2007).

217. Vega, E. J., et al., Global and local instability of flow focusing: The influence of the geometry. *Physics of Fluids*, 22(6), 064105 (2010).

218. Squires, T. M., and Quake, S. R., Microfluidics: Fluid physics at the nanoliter scale. *Reviews of Modern Physics*, 77(3), 977-1026 (2005).

219. Van Dommelen, R., Fanzio, P., and Sasso, L. Surface self-assembly of colloidal crystals for micro- and nano-patterning. *Advances in Colloid and Interface Science*, 251, 97-114 (2018).

220. Galindo-Rosales, F. J., Alves, M. A., and Oliveira, M. S. N., Microdevices for extensional rheometry of low viscosity elastic liquids: a review. *Microfluidics and Nanofluidics*, 14(1-2), 1–19 (2012).

221. Gupta, S., Wang, W. S., and Vanapalli, S. A. Microfluidic viscometers for shear rheology of complex fluids and biofluids. *Biomicrofluidics*, 10(4), 043402 (2016).

222. Haward, S. J., Microfluidic extensional rheometry using stagnation point flow. *Biomicrofluidics*, 10(4), 043401 (2016).

223. Di Carlo, D., Inertial microfluidics. *Lab on a Chip*, 9(21), 3038 (2009).

224. Girardo, S., Cingolani, R., and Pisignano, D. Microfluidic Rheology of Non-Newtonian Liquids. *Analytical Chemistry*, 79(15), 5856-5861 (2007).

225. Brenner, H., Rheology of a dilute suspension of axisymmetric Brownian particles. *International Journal of Multiphase Flow*, 1(2), 195–341 (1974).

226. Powell, R. L., Rheology of suspensions of rodlike particles. *Journal of Statistical Physics*, 62(5-6), 1073–1094 (1991).

227. Macosko, C.W., Rheology Principles, Measurements, and Applications. *Wiley-VCH*, (1994).

228. Wagner, N. J., and Brady, J. F. Shear thickening in colloidal dispersions. *Physics Today*, 62(10), 27-32 (2009).

229. Toschi, F., and Bodenschatz, E. Lagrangian Properties of Particles in Turbulence. *Annual Review of Fluid Mechanics*, 41(1), 375-404 (2009).

230. Lundell, F., Söderberg, L. D., and Alfredsson, P. H., Fluid Mechanics of Papermaking. *Annual Review of Fluid Mechanics*, 43(1), 195-217 (2011).

231. Gunes, D. Z., Scirocco, R., Mewis, J., and Vermant, J. Flow-induced orientation of non-spherical particles: Effect of aspect ratio and medium rheology. *Journal of Non-Newtonian Fluid Mechanics*, 155(1-2), 39-50 (2008).

232. Leahy, B. D., Koch, D. L., and Cohen, I. The effect of shear flow on the rotational diffusion of a single axisymmetric particle. *Journal of Fluid Mechanics*, 772, 42–79 (2015).

233. Rosén, T., et al., Three-Dimensional Orientation of Nanofibrils in Axially Symmetric Systems Using Small-Angle X-ray Scattering. *The Journal of Physical Chemistry C*, 122(12), 6889–6899 (2018).

234. Parsheh, M., Brown, M. L., and Aidun, C. K., On the orientation of stiff fibres suspended in turbulent flow in a planar contraction. *Journal of Fluid Mechanics*, 545(-1), 245 (2005).

235. Vasireddi, R., et al., Shear and Flow Orientation Dynamics of Anisotropic Nanoparticles in Microfluidic Sheet-like Microjets, *in preparation* (2109).

236. Spence, J. C. H., XFELs for structure and dynamics in biology. *IUCrJ*, 4(4), 322-339 (2017).

237. De Jeu, W. H., Basic X-ray Scattering for soft matter, *Oxford, University Press*, (2016).

238. Als-Nielsen, J., and McMorrow, D., Elements of modern X-ray Physics, *John Wiley and Sons*, 2011.

239. Feigin, L. A., and Svergun, G. I., Structure Analysis by Small-Angle X-ray and Neutron Scattering, *Plenum Press, New York*, (1987).

240. Guinier, A., and Fournet, G., Small-Angle Scattering of X-rays, *Wiley, Ney York*, (1955).

241. Shayeganfar, F., et al., Controlled nucleation and growth of CdS nanoparticles by turbulent dispersion. *Physical Review E*, 81(2) 2010).

242. Lindner, P., and Zemb, T. Neutrons, X-rays and Light. Scattering Methods applied to Soft Condensed Matter., *Elsevier*, (2002).

243. Schnablegger, H. and Singh, Y., The SAXS Guide. Getting acquainted with the principles. *Anton-Paar GmbH*, (2013).

244. Glatter, O., and Hainisch, B., Improvements in real-space deconvolution of small-angle scattering data. *Journal of Applied Crystallography*, 17(6), 435–441 (1984).

245. Glatter, O., Convolution square root of band-limited symmetrical functions and its application to small-angle scattering data. *Journal of Applied Crystallography*, 14(2), 101–108 (1981).

246. Glatter, O., The interpretation of real-space information from small-angle scattering experiments. *Journal of Applied Crystallography*, 12(2), 166–175 (1979).

247. Glatter, O., Evaluation of small-angle scattering data from lamellar and cylindrical particles by the indirect transformation method. *Journal of Applied Crystallography*, 13(6), 577–584 (1980).

248. Trebbin, M., Microfluidics at high-intensity X-ray sources: from microflow chips to microfluidic liquid jet systems, *University of Bayreuth*, (2013).

249. Oliveira, C. L. P., et al., Gaussian deconvolution: a useful method for a form-free modeling of scattering data from mono- and multilayered planar systems. *Journal of Applied Crystallography*, 45(6), 1278–1286 (2012).

250. Svergun, D. I., Mathematical methods in small-angle scattering data analysis. *Journal of Applied Crystallography*, 24(5), 485-492 (1991).

251. Förster, S., et al., Calculation of scattering-patterns of ordered nano- and mesoscale materials. *Advances in Colloid and Interface Science*, 163(1), 53–83 (2011).

252. Pedersen, J. S., Small-angle scattering from precipitates: Analysis by use of a polydisperse hard-sphere model. *Physical Review B*, 47(2), 657–665 (1993).

253. Pedersen, J. S., Analysis of small-angle scattering data from colloids and polymer solutions: modeling and least-squares fitting. *Advances in Colloid and Interface Science*, 70, 171–210 (1997).

254. Allec, N., et al., Small-angle X-ray scattering method to characterize molecular interactions: Proof of concept. *Scientific Reports*, 5(1) (2015).

255. Brunner-Popela, J., and Glatter, O., Small-Angle Scattering of Interacting Particles. I. Basic Principles of a Global Evaluation Technique. *Journal of Applied Crystallography*, 30(4), 431-442v (1997).

256. Cullity, B. D., and Stock, S.R., Elements of X-ray Diffraction, *Pearson Education Limited* (1959).

257. Märkert, C., Fischer, B., and Wagner, J., Small-angle scattering from spindle-shaped colloidal hematite particles in external magnetic fields. *Journal of Applied Crystallography*, 44(3), 441-447 (2011).

258. Eddings, M. A., Johnson, M. A., and Gale, B. K., Determining the optimal PDMS–PDMS bonding technique for microfluidic devices. *Journal of Micromechanics and Microengineering*, 18(6), 067001 (2008).

259. Kruse, J., Spinning of functional polymer microfibers using GDVN based microfluidic devices, master thesis, *University of Hamburg,* (2018).

260. Patra, A. K., Kundu, S. K., Bhaumik, A., and Kim, D. Morphology evolution of single-crystalline hematite nanocrystals: magnetically recoverable nanocatalysts for enhanced facet-driven photoredox activity. *Nanoscale*, 8(1), 365–377 (2016).

261. Märkert, C., Fischer, B., and Wagner, J. Small-angle scattering from spindle-shaped colloidal hematite particles in external magnetic fields. *Journal of Applied Crystallography*, 44(3), 441-447 (2011).

262. Ganan-Calvo, A. M. On the theory of electrohydrodynamically driven capillary jets. *Journal of Fluid Mechanics*, 335, 165-188 (1997).

263. Mata, A., Fleischman, A. J., and Roy, S. Fabrication of multi-layer SU-8 microstructures. *Journal of Micromechanics and Microengineering*, 16(2), 276–284 (2006).

264. Lorenz, H., et al., High-aspect-ratio, ultrathick, negative-tone near-UV photoresist and its applications for MEMS. *Sensors and Actuators A: Physical*, 64(1), 33-39 (1998).

265. Hee, L., et al., A new fabrication process for uniform SU-8 thick photoresist structures by simultaneously removing edge bead and air bubbles, Journal of Micromechanics and Microengineering 21(12):125006 (2011).

266. Chandrasekhar, S., Hydrodynamic and hydromagnetic stability, *Dover Publications* (1981).

267. Ozaki, M., Kratohvil, S., and Matijević, E., Formation of monodispersed spindle-type hematite particles. *Journal of Colloid and Interface Science*, 102(1), 146–151 (1984).

268. Huang, Z.M., et al., A review on polymer nanofibers by electrospinning and their applications in nanocomposites. *Compos Sci Technol* 63(15):2223-2253 (2003).

269. Pham, Q.P., Sharma, U., and Mikos, A.G., Electrospun Poly(ε-caprolactone) Microfiber and Multilayer Nanofiber/Microfiber Scaffolds: Characterization of Scaffolds and Measurement of Cellular Infiltration. *Biomacromolecules* 7 (10): 2796-2805 (2006).

270. Chae, S.K., et al., Micro/Nanometer-scale fiber with highly ordered structures by mimicking the spinning process of silkworm. *Adv mater* 25(22): 3071-3078 (2013).

271. Lepore, E., et al., Spider silk reinforced by graphene or carbon nanotubes. *2D Materials* 4(3): 031013 (2017).

272. Pacheco, M., et al., INTECH Open Access Publisher: Synthesis of Carbon Nanofibers by a Glow-Arc Discharge, *Nanofibers*, 253-268 (2010).

273. Zhang, Y., et al., Microfluidic-Spinning-Directed Microreactors Toward Generation of Multiple Nanocrystals Loaded Anisotropic Fluorescent Microfibers. *Adv Funct Mater* 25(47): 7253-7262 (2015).

274. Daniele, M.A., et al., Microfluidic strategies for design and assembly of microfibers and nanofibers with tissue engineering and regenerative medicine applications. *Adv Healthc Mater* 4(1): 11-28 (2015).

275. Rujitanaroj, P.O., Pimpha, N., and Supaphol, P., Wound-dressing materials with antibacterial activity from electrospun gelatin fiber mats containing silver nanoparticles. *Polymer* 49(21): 4723-4732 (2008).

276. Chen, J.P., Chang, G.Y., and Chen, J.K, Electrospun collagen/chitosan nanofibrous membrane as wound dressing. *Colloids Surf A Physicochem Eng Asp* 313-314:183-188 (2008).

277. Podgórski, A., Bałazy, A., and Gradoń, L., Application of nanofibers to improve the filtration efficiency of the most penetrating aerosol particles in fibrous filters. Chem Eng Sci 61(20): 6804-6815 (2006).

278. Bognitzki, M., et al. Preparation of fibers with nanoscaled morphologies. Electrospinning of polymer blends. *Polym Eng Sci* 41(6): 982-989 (2001).

279. Ok, S., Furquan, S.A., Khan, Z., and Dogan, A.U, Near superhydrophobic-fluorinated THV fiber-like structures and fibers prepared by electrospinning. *High Performance Polym* 28(2): 206-214 (2016).

280. Abolhasani, M.M., Naebe, M., Shirvanimoghaddam, K., Fashandi, H., Khayyam, H., Joordens, M., Pipertzis, A., Anwar, S., Berger, R., Floudas, G., Michels, J., and Asadi, K. Thermodynamic approach to tailor porosity in piezoelectric polymer fibers for application in nanogenerators. *Nano Energy* 62, 594-600 (2019).

281. Chen, X., Xu, Y., Zhang, W., Xu, K., Ke, O., Jinab, X., and Huang, C. Online fabrication of ultralight, three-dimensional, and structurally stable ultrafine fibre assemblies with a double-porous feature. *Nanoscale* 11, 8185-8195 (2019).

282. Stierle, A., Keller, T.F., Noei, H., Vonk, V., and Roehlsberger, R. DESY NanoLab. *J.* Large-Scale Res. Facil. JLSRF 2 A76**,** 1-9 (2016).

283. Onoe, H., Okitsu, T., Itou, A., Kato-Negishi, M., Gojo, R., Kiriya, D., Sato, K., Miura, S., Iwanaga, S., Kuribayashi-Shigetomi, K., Matsunaga, Y.T., Shimoyama, Y., and Takeuchi, S. Metre-long cell-laden microfibres exhibit tissue morphologies and functions. *Nat. Mater.* 12(6), 584-590 (2013).

284. Medeiros, E.S., Glenn, G. M., Klamczynski, A.P., Orts, W.S., and Mattoso, L. H. C., Solution blow spinning: A new method to produce micro- and nanofibers from polymer solutions. *Journal of Applied Polymer Science*,113, 2322-2330 (2009).

285. Benavides, R.E., Jana, S.C., and Reneker, D.H, Nanofibers from Scalable Gas Jet Process. *ACS Macro Lett* 1(8): 1032-1036 (2012).

286. Ponmozhi, J., et al., Thermodynamic and Transport Properties of CNT-Water Based Nanofluids. *JNanoR* 11, 101–106 (2010).

287. Colby, R. H., et al., Shear thinning of unentangled flexible polymer liquids, Rheologica Acta 46(5):569-575 (2007).

288. Schlenk, M., et al. Parallel and Perpendicular Alignment of Anisotropic Particles in Free Liquid Microjets and Emerging Microdroplets. *Langmuir* 34(16): 4843-4851 (2018).

289. Ahir, S.V., Huang, Y.Y., and Terentjev, E.M., Polymers with aligned carbon nanotubes. Active composite materials. *Polymer* 49, 3841–3854 (2008).

290. Sadri, R. et al., An experimental study on thermal conductivity and viscosity of nanofluids containing carbon nanotubes. *Nanoscale research letters* 9, 151 (2014).

291. Feng, X., et al., A Fast and Effective Microfluidic Spraying-Plunging Method for High-Resolution Single-Particle Cryo-EM. *Structure,* 25(4), 663–670.e3 (2017).

292. Hu, X., et al., The Use of Microfluidics in Rheology. *Macromolecular Materials and Engineering*, 296(3-4), 308–320 (2011).

293. Trincao, J., et al., Dynamic structural science: recent developments in time-resolved spectroscopy and X-ray crystallography: Figure 1. *Biochemical Society Transactions*, 41(5), 1260–1264 (2013).

294. Wang, D., et al., Double-focusing mixing jet for XFEL study of chemical kinetics. *Journal of Synchrotron Radiation,* 21(6), 1364–1366 (2014).

295. Levantino, M., et al., Using synchrotrons and XFELs for time-resolved X-ray crystallography and solution scattering experiments on biomolecules, *Curr. Opin. Struct. Biol.* 35, 41–48 (2015).

296. Spence, J. C. H., XFELs for structure and dynamics in biology. *IUCrJ*, 4(4), 322–339 (2017).

297. Dimitrios, K., et al., A cryo-EM grid preparation device for time-resolved structural studies, 6, 1024-1031, (2019).

298. Bartesaghi, A., et al., 2.2 A resolution cryo-EM structure of -galactosidase in complex with a cell-permeant inhibitor. *Science,* 348(6239), 1147–1151 (2015).

299. Marsh, J.A., Protein Complex Assembly, *Springer New York, Humana Press*, (2018).

List of publications

Published:

1. Deepak Kumar Khajuria, **Ramakrishna Vasireddi**, Martin Trebbin, David Karasik and Rema Razdan; Novel therapeutic intervention for osteoporosis prepared with strontium hydroxyapatite and zoledronic acid: in vitro and pharmacodynamic evaluation; **Materials Science & Engineering C 71, 698-708 (2017).**

2. **Ramakrishna Vasireddi,** Joscha Kruse, Mohammad Vakili, Satishkumar Kulkarni, Thomas F Keller, Diana C.F. Monteiro, Martin Trebbin; Solution blow spinning of polymer/nanocomposite micro-/nanofibers with tunable diameters and morphologies using a gas dynamic virtual nozzle; **Scientific Reports, 9, 1-10 (2019).**

3. Mohammad Vakili, Stefan Merkens, Yunyun Gao, Paul Gwozdz, **Ramakrishna Vasireddi**, Lewis Sharpnack, Andreas Meyer, Robert Blick, Martin Trebbin; 3D-Micromachined Polyimide Mixing Devices for in Situ X-ray Imaging of Solution-Based Block Copolymer Phase Transitions; **Langmuir, 35, 10435-10445 (2019).**

Manuscripts ready for submission:

4. **Ramakrishna Vasireddi,** Sankar Raju Narayanasamy, Diana C.F. Monteiro, Nils Huse, Martin Trebbin; Development of a high fidelity stable microfluidic flat liquid jet system for versatile applications; **Lab on a chip (Finalizing manuscript for submission (2020).**

5. Mohammad Vakili, **Ramakrishna Vasireddi,** Diana C.F. Monteiro, Martin Trebbin**;** Fully Polyimide-based Liquid Jet Systems for In situ X-ray Studies; **Lab on a chip (Finalizing manuscript for submission (2020).**

In preparation:

6. **Ramakrishna Vasireddi,** Sankar Raju Narayanasamy, Diana C.F. Monteiro, Mohammad Vakili, Joana Valerio, Nils Huse, Gerhard Grübel, Martin Trebbin, Shear and Flow Orientation Dynamics of Anisotropic Nanoparticles in Microfluidic Sheet-like Microjets; **(in preparation).**

7. **Ramakrishna Vasireddi,** Joscha Kruse, Mohammad Vakili, Diana C.F. Monteiro, Thomas F Keller, Martin Trebbin; Effect of flow-induced anisotropic nanoparticle orientation in polymer fiber with microfluidic spinning; **(in preparation).**

8. **Ramakrishna Vasireddi,** Sankar Raju Narayanasamy, Martin Trebbin; Whipping Instability of Anisotropic Microfluidic Liquid Jet Devices; **(In preparation).**

9. Mohammad Vakili, Tomke Glier, Tobias Gerling, **Ramakrishna Vasireddi,** Yunyun Gao, Florian Kopf, Matthew Derry, Andreas Mayer, Stephan V. Roth, Martin Trebbin; Microfluidic Synthesis of PDMAm-PMEA diblock copolymer nano-objects: An In Situ SAXS Study; **(In preparation).**

10. Thiele, C., Monteiro, D.C.F., **R, Vasireddi,** Schroer, C., Trebbin, M. Dynamic flow alignment of anisotropic particles in liquids studied by in situ SAXS tomography. **(In preparation).**

Conference presentations

1. **R. Vasireddi**; Microfluidic Devices for Ultrafast Structural Dynamics and Biological Applications; **CUI winter school 2016**, The Hamburg Centre for Ultrafast Imaging, Feb 15-19 (2016).

2. S. Bommel, M. Vakili, D. Monteiro, **R. Vasireddi**, S. Hinrichs, F. Lauterbach, P. Gwozdz, G. Yang, M. Heymann, H. N. Chapman and M. Trebbin; Microfluidics and X-ray Scattering for In Situ Time-Resolved Studies; **DESY Research Course 2016**-Soft Matter in the Light of Modern X-ray Sources, Mar 2-4 (2016).

3. M. Vakili, D. Monteiro, **R. Vasireddi,** T. Glier, T. Gerling, P. Gwozdz, R. Blick, H. N. Chapman, and M. Trebbin; Microfluidics and X-ray scattering for In Situ Time-resolved Studies; **CUI Annual Meeting**, Oct 5-7 (2016).

4. **R. Vasireddi,** D. Monteiro, M. Vakili, A. Naidu, V. Quint, O. Aust, C. Thiele, H. N. Chapman, M. Rübhausen, N. Huse and M. Trebbin; Fluid Dynamics of Flat Liquid Jets; **CUI Annual Meeting**, Oct 5-7 (2016).

5. Diana C.F. Monteiro, Sebastian Bommel, **Ramakrishna Vasireddi,** Mohammad vakili, Martin Trebbin; Microfluidic devices for fast time-resolved studies; **Acta Cryst A, A72, s182 (2016).**

6. **Ramakrishna Vasireddi,** Mohammad Vakili, Diana Monteiro and Martin Trebbin; Size Controlled Synthesis of γ-Fe_2O_3 Nanoparticles by Simple Chemical method and Study of Optical Properties; **International Journal of Science, Engineering and Management, 1,10-14 (2016).**

7. M. Vakili, T. Glier, T. Gerling, **R. Vasireddi,** D. Monteiro, M. Trebbin, Microfluidics, and X-ray Scattering for In Situ Time-Resolved studies of Macromolecules, **7th International Colloids Conference**, Sitges, Barcelona, Spain, June 18-21 (2017).

8. **R. Vasireddi**; Fluid Dynamics in Anisotropic Microfluidic Liquid Jet Devices; **CUI winter school 2017**, The Hamburg Centre for Ultrafast Imaging, Feb 20-24 (2017).

9. **R. Vasireddi,** J. Kruse, J. Nette, A. Naidu, O.Aust, M. Vakili, F. Kopf, D. Monteiro, H. N. Chapman, M. Rübhausen, N. Huse and M. Trebbin; Fluid Dynamics of Flat Liquid Jet Devices; **CUI Annual Meeting**, Oct 11-13 (2017).

10. **R. Vasireddi**; Stable flat liquid jet microfluidic system for solution phase X-ray experiments; **CUI winter school 2018**, The Hamburg Centre for Ultrafast Imaging, Feb 26 (2018).

11. M. Vakili, T. Glier, S. Merkens**, R. Vasireddi,** D. Monteiro, F. Kopf, Y. Rao, P. Gwozdz, R. Blick, T. Narayanan, S.V. Roth, and M. Trebbin; In Situ SAXS for Time-resolved Soft Matter Studies; **PIER graduate week (2018) (Best poster award).**

12. **R. Vasireddi,** J. Kruse, M. Vakili, D. Monteiro, F. Kopf, H. N. Chapman, T. F. Keller, N. Huse, and M. Trebbin; GDVN based microfluidic liquid jet technology for various applications; **PIER graduate week (2018) (Best poster award).**

13. **R. Vasireddi,** J. Kruse, M. Vakili, F. Kopf, D. Monteiro, H. N. Chapman, T. F. Keller, N. Huse, and M. Trebbin; GDVN microfluidic nozzle for the spinning of polymer nanofibers, fibres with tunable surface morphologies and nanocomposite fibers; **MSME 2018**, Nov 08-10 (2018).

14. **R. Vasireddi,** J. Kruse, M. Vakili, F. Kopf, D. Monteiro, H. N. Chapman, T. F. Keller, N. Huse and M. Trebbin; Microfluidic liquid jet; **CUI Annual Meeting**, Nov 14-16 (2018).

15. **R. Vasireddi,** J. Kruse, M. Vakili, F. Kopf, D. Monteiro, H. N. Chapman, T. F. Keller, N. Huse, and M. Trebbin; Microfluidic liquid jet systems for Synchrotrons and XFELs; **XFEL users meeting**, Jan 23-25 (2019).

16. N. Sankar, **R. Vasireddi,** D. Monteiro, F. Kopf, N. Huse, S. Glenzer and M. Trebbin; Computational fluid dynamic characterization of liquid sheets suitable for XFEL and Synchrotron experiments; **BioXFEL 6th international conference**, Feb 12-14 (2019).

Acknowledgments

First and foremost, I would like to express my sincere gratitude to my advisor Prof. Dr. Martin Trebbin, for allowing me to work on both exciting and challenging research topics and leaving me the freedom needed for the experiments. His continuous support at all times and stimulating - ideas during the process of device development and X-ray data analysis has taken my entire doctoral research to be of more considerable significance in the X-ray community. Mostly, he gave me the freedom and trust to unfold my potential to work and grow as a research scientist. Also, I would like to thank him for the opportunity that he had given me to supervise bachelor and master students for various exiting experiments and allowing me for my colleague's beamtime experiments as well as performing my research at the highest level.

I am deeply thankful to my co-supervisor, Prof. Dr. Nils Huse, for his continuous guidance and follow-ups on the progress of my work. I also would like to thank him for his financial support for my extension in the last stage of my Ph.D. I have benefitted a lot from his motivations, expertise and fruitful discussions right from the day one of my work.

I am also very grateful to Prof. Dr. Grubel Gerhard for his sample support and fruitful discussions during beamtime, Prof. Dr. Henry Chapman, for cleanroom support, Dr. Thomas Keller, for allowing me to use SEM/FIB Nanolab and indeed for further research discussions.

In particular, I am thankful to my colleague's Mr. Mohammad Vakili for the stimulating discussions and ideas as well as immediate help in various situations and all stimulated discussions we had for combined projects, Dr. Diana Monteiro for her supports on nozzle optimization steps for further improvements and always suggests ideas on the projects and gave me valuable support whenever needed, Dr. Florian Kopf for his help to improve theses and valuable discussions during peer review thesis, Dr. Sebastian Bommel for introducing cleanroom experiments.

I am also thankful to people at ID13 and P03 beamlines at ESRF and DESY, who have always willing to help during the experiments. I am especially thankful to Dr. Pallavi Pandit and Dr.

Tilman Grunewald for their support before and after experiments. I am also thankful to Dr. Andre Rothkirch for data analysis, fruitful suggestions.

I want to thank Joana Valerio and Irina Lokteva for their sample preparation and characterization support for beamtime experiments and their stimulating discussions. I also thanks to Satish Kumar for his SEM/FIB characterization and enjoyable coffee after experiments.

I must thank my bachelor and master students Oliver Aust, Akhil Naidu, Julia Nette, Joscha Kruse and Sankar Raju Narayanasamy for sharing the lab with exciting experiments and generating new results. I also want to thank them for all the stimulating discussions for manuscript writing and the fun we had in the past three years.

Furthermore, I would also like to thank all my friends who have supported me before and during my Ph.D. I have always enjoyed with them after the working hours. Thank you all for understanding my situation and helps me a lot to solve problems. I especially thank my family friends Brahmanandam, Srinu, Kasi Naidu, Nagaraja, Rakesh and Venkanna for their family support and useful discussions keeping me always in good standing.

On the personal side, I much express my very profound gratitude to my parents Chinnammi and Satyam Naidu. I am very much grateful to them for their loving affection, prayers and endless support at all time. I cannot express how much I appreciate what you have done for me. I would also like to thank my brother and sister-in-law Maheshwar Rao and Veeramani for their encouragement and concern for me. I also thank my brother-in-law and sisters Satyanarayana, Laxmi, Ramu, Devi and Mani for their support and love for me.

Finally, I owe my deepest gratitude towards my wife, Revathi, for her continued support and understanding of my goals and aspirations. She has been incredibly supportive during the long months of writing and has made countless sacrifices to help me get to this point.

Eidesstattliche Versicherung/ Declaration on oath

Hiermit versichere ich an Eides statt, die vorliegende Dissertationsschrift selbst verfasst und keine anderen als die angegebenen Hilfsmittel und Quellen benutzt zu haben.

Die eingereichte schriftliche Fassung entspricht der auf dem elektronischen Speichermedium.

Die Dissertation wurde in der vorgelegten oder einer ähnlichen Form nicht schon einmal in einem früheren Promotionsverfahren angenommen oder als ungenügend beurteilt.

V. Rama Krishna

Hamburg, den 15.02.2019

_____

Unterschrift der Doktorandin / des Doktoranden